Mechanical properties characterization of two-dimensional materials via nano-indentation experiments

Guoxin Cao, Huajian Gao

PII: S0079-6425(19)30025-8
DOI: https://doi.org/10.1016/j.pmatsci.2019.03.002
Reference: JPMS 557

To appear in: *Progress in Materials Science*

Received Date: 16 June 2018
Revised Date: 25 February 2019
Accepted Date: 4 March 2019

Please cite this article as: Cao, G., Gao, H., Mechanical properties characterization of two-dimensional materials via nanoindentation experiments, *Progress in Materials Science* (2019), doi: https://doi.org/10.1016/j.pmatsci.2019.03.002

Mechanical properties characterization of two-dimensional materials via nanoindentation experiments

Guoxin Cao[a] and Huajian Gao[b]

[a] *School of Aerospace Engineering and Applied Mechanics, Tongji University, Shanghai 200092, China, Corresponding address: Guoxin Cao: caogx@pku.edu.cn*

[b] *School of Engineering, Brown University, Providence, RI 02912, USA, Corresponding address: Huajian Gao: huajian_gao@brown.edu*

Abstract:

Nanoindentation has been widely adopted for mechanical properties characterization of two-dimensional (2D) materials, where one typically starts with measuring the indentation load-displacement relationship of a selected 2D material, either free-standing or on a substrate, and then fits the result to an analytical model to extract the elastic modulus and strength of the material. However, the existing indentation models were not originally intended to be used for atomically thin materials, which has led to some controversies and confusion in the field. There is now an urgent need to develop new analytical models capable of describing the indentation response of 2D materials for accurate characterization of their mechanical properties. Here, we review recent progress in this field to identify existing issues and opportunities for future studies.

Keywords: 2D materials; mechanical properties; nanoindentation testing.

Outline

Abbreviations list:

2D: two-dimensional
ac: armchair
AFM: atomic force microscopy
BP: black phosphorous
CVD: chemical vapor deposition
DFT: density functional theory
FEM: finite element method
FS: free-standing
FSI: free-standing indentation
GO: graphene oxide
MD: molecular dynamics
PDMS: polydimethylsiloxane
PET: polyethylene terephthalate
QM: quantum mechanics
SEM: Scanning electron microscopy
vdW: van der Waals
zz: zigzag

1. Introduction

Two-dimensional (2D) materials, including graphene [1], layered transition metal dichalcogenides (e.g., MoS_2 and WS_2 [2-4]) and layered black phosphorous (BP) [5, 6] have attracted worldwide research interest due to their unique electrical, thermal and mechanical properties. Many potential applications of 2D materials (e.g., 2D nanodevices) are related to their mechanical properties [7-12], such as elastic modulus E, Poisson ratio ν and intrinsic strength σ_{int}. Due to the nanoscale thickness of 2D materials, measuring their mechanical properties via conventional tensile and bending testing approaches is challenging [13-15]. Numerical studies to investigate the intrinsic mechanical properties of 2D materials have been primarily based on atomic simulations, including classic molecular dynamics (MD) with empirical interatomic potentials [16-20] and quantum mechanics (QM)-based techniques [21-26].

The mechanical behavior of 2D materials depends on the range of applied loads. Based on the first principle calculations [21-24], graphene exhibits an anisotropic nonlinear behavior under sufficiently large deformation (e.g., $\varepsilon > 5\%$), whereas it follows an isotropic linear behavior under very small deformation. Similar statements can be made for other 2D materials except for BP, which behaves highly anisotropic [18, 26, 27]. Therefore, other than BP, most 2D materials undergoing small deformations can be regarded as isotropic and linear elastic with Young's modulus E and Poisson ratio ν. Under moderate to large deformations, 2D materials are often modeled as a continuum thin shell with the following constitutive relationship [17, 21, 24, 25, 28-30]:

$$\sigma = E\varepsilon + D\varepsilon^2 \tag{1}$$

where the coefficient D of the second-order term is typically taken to be negative ($D < 0$), leading to a reduced stiffness with increasing tensile strain. The maximum value of σ, at which $\partial\sigma / \partial\varepsilon = 0$, defines the so-called intrinsic strength and strain to failure as follows:

$$\sigma_{\text{int}} = -E^2/4D \quad \text{at the strain} \quad \varepsilon_{\text{int}} = -E/2D. \tag{2}$$

Note that there are also more sophisticated nonlinear and anisotropic constitutive models [22, 24, 31, 32], which have more model parameters and can more accurately describe nonlinear

and anisotropic behaviors of a 2D material under large deformation. However, determining all the parameters associated with these models via experiments is challenging.

Indentation testing is by far the most frequently adopted method for characterizing the mechanical properties of 2D materials. This method can be divided into two categories: (1) indentation of free-standing (FS) 2D materials via AFM, referred to as free-standing indentation (FSI) testing [27, 33-53], and (2) instrumented nanoindentation of 2D materials on a substrate [54-57]. In such tests, the indentation load-displacement relationship of a 2D material, either FS or on a substrate, is measured, and the material's mechanical properties are then extracted by fitting the measured load-displacement curve to an analytical model. 2D materials subject to indentation are typically regarded as linear and isotropic, and all existing indentation models are derived based on the assumption of an isotropic linear elastic solid.

In measuring the elastic modulus of a 2D material via indentation, the indenter displacement is typically quite small, which causes a small in-plane tensile strain in the 2D material except in the vicinity of the indenter tip [33, 55, 56, 58, 59]. In such cases, the elastic modulus determined from a nonlinear elastic model of the 2D material is similar to that obtained from the linear elastic model. Measuring the strength of a 2D material often leads to large indenter displacement and large in-plane tensile strain in the 2D material, such that a nonlinear elastic model should be used otherwise the strength of the 2D material will be overestimated [33]. However, there is no analytical solution for the relationship between indenter load and the maximum in-plane stress for nonlinear membranes (modeled via Eq.(1)), such that numerical simulations (e.g., FEM [33, 40, 55, 60, 61]) are often employed, in which the nonlinear elastic behavior (e.g., represented by D in Eq.(1)) can be effectively obtained. For anisotropic materials (e.g., single-layer BP) [27], an average of the Young's moduli along different orientations is obtained along with the minimum value of strengths along different orientations.

One problem with this approach is that the existing indentation models were not originally intended for atomically thin 2D materials, which has led to some controversies and confusion in the field. Here, we review selected theoretical and experimental studies related to

mechanical properties characterization of 2D materials via indentation testing. The aims of this review are (1) to emphasize some of the key issues associated with the indentation testing of 2D materials which might affect their mechanical properties characterization and (2) to highlight some opportunities for future studies in this field.

This paper is organized as follows: Section 2 provides the theoretical studies of FSI response of continuous structures (including basic equations associated with FSI). The FSI testing of 2D materials is discussed in Section 3, which starts from the theoretical model (equations and methods), followed by analysis of different issues associated with the FSI testing of 2D materials, including the effects of the sample geometry, boundary conditions, pre-stress, material nonlinearity (in-plane nonlinear stress-strain relationship of 2D materials), defects (e.g., grain boundaries), and van der Waals (vdW) interactions with an AFM tip and with a substrate near the boundary of the FS region. Section 4 describes the indentation testing of 2D materials mounted on a substrate, where the issues of interest include the influence of the elastic modulus ratio of the 2D material to its substrate and the effects of material nonlinearity and interfacial properties. The final section provides a summary of some of the existing issues in the indentation characterization of 2D materials and selected topics of interest for future studies.

2. Theoretical studies of FSI response of continuous structures

Classical models of beam bending and membrane stretching have been used to predict the indentation response of 2D materials [35, 62-70]. When the ratio of sample size to indenter tip radius, a/R, is large (e.g., $a/R > 30$), the indenter load-displacement relationship is not sensitive to the tip radius (R) so that the indenter can be regarded as a point load [62]. In this way, the elastic modulus of a sample measured via FSI is commonly based on the point load assumption, e.g., for a clamped circular thin plate [62]. However, when the ratio of sample size to tip radius is not large enough (e.g., $a/R < 30$), the indenter load-displacement relationship can be significantly influenced by the indenter tip radius R, and thus, a finite size tip should be considered [65]. A finite radius should always be used for determining the intrinsic strength.

2.1 Clamped beam

The relationship between the indentation load (P) and displacement (δ_t) of a doubly clamped beam subject to a point force at the center of the beam [35, 71] is as follows:

$$P = \left(\frac{\pi^4 EW}{6} \left(\frac{t}{L} \right)^3 + \frac{\pi^2 T}{2L} \right) \delta_t + \frac{\pi^4 EWt}{8} \left(\frac{\delta_t}{L} \right)^3, \tag{3}$$

where T denotes a pre-tension in the beam, W is the beam width, L is the beam length, and t is the beam thickness. The three terms on the right-hand side of Eq. (3) are associated with bending, pre-tension and stretching. Note that Eq. (3) is an approximate solution, with a typical error of a few percent relative to the exact beam solution [72].

For a small indentation displacement relative to the sample thickness, i.e., $\delta_t < t$, a sample subjected to FSI primarily undergoes bending, and the stretching term in Eq. (3) can be neglected. In this case, the P-δ_t relationship is approximately linear with the following slope:

$$k = \frac{P}{\delta_t} = \frac{\pi^4 EW}{6} \left(\frac{t}{L} \right)^3 + \frac{\pi^2 T}{2L} \quad . \tag{4}$$

The contribution from stretching, represented by the third term in Eq. (3), increases rapidly with increasing indentation displacement and becomes dominant when $\delta_t >> t$. In that case, the first term in Eq. (3) becomes negligible, and the P-δ_t relationship can be expressed as follows:

$$P = \frac{\pi^2 Wt\sigma_0}{2} \left(\frac{\delta_t}{L} \right) + \frac{\pi^4 EWt}{8} \left(\frac{\delta_t}{L} \right)^3 \tag{5}$$

where $\sigma_0 = T/(Wt)$.

2.2 Clamped circular thin plate

The relationship between the indentation load and displacement of a clamped circular thin plate subject to a point force at the center of the plate is as follows [62, 64, 65]:

$$P = \left[\frac{4\pi Et^3}{3(1-\nu^2)a} + T \right] \frac{\delta_t}{a} + E(\xi^3 ta) \left(\frac{\delta_t}{a} \right)^3 \tag{6}$$

where a is the sample radius and $\xi = 1/(1.049 - 0.15\nu - 0.16\nu^2)$ is a function of Poisson ratio ν.

Similar to Eq. (3), the three terms on the right-hand side of Eq. (6) correspond to bending, pre-tension, and stretching.

When the indentation displacement is smaller than the sample thickness, stretching is considered small; consequently, the third term in Eq. (6) can be neglected. In this case, the indentation stiffness arises primarily from bending and pre-tension, and the P-δ_t relationship is approximately linear with the slope:

$$k = \frac{P}{\delta_t} = \frac{4\pi a E}{3\left(1-\nu^2\right)}\left(\frac{t}{a}\right)^3 + \frac{T}{a} \tag{7}$$

For $\delta_t >> t$, the first term in Eq. (6) becomes negligible, and the P-δ_t relationship becomes:

$$P = \sigma_0\left(\pi t a\right)\frac{\delta_t}{a} + E\left(\xi^3 t a\right)\left(\frac{\delta_t}{a}\right)^3 \tag{8}$$

where $\sigma_0 = T/(\pi a t)$.

2.3 Fracture strength

For a clamped, linear elastic, circular membrane subject to indentation, if the ratios of R/a and σ_0/E are small (R denotes the indenter tip radius), an analytical relationship between the indentation load and the maximum membrane stress (σ_m) in the contact region directly underneath the indenter can be approximately obtained [70]. The restriction condition for this approximate solution is given via a dimensionless factor [70]:

$$\zeta = 2^{\frac{2}{3}}\left(\frac{\sigma_0}{E}\right)^{\frac{1}{3}}\left(\frac{R}{a}\right)^{\frac{2}{3}} \tag{9}$$

If $\zeta << 1$, the P-σ_m relationship can be estimated as $P = 4\pi R t \sigma_m^2 / E$; the value of σ_m corresponding to the maximum indentation load (P_f) is typically considered as the fracture strength of membrane, expressed as follows [70]:

$$\sigma_f = \left(\frac{P_f E}{4\pi R t}\right)^{\frac{1}{2}} \tag{10}$$

3. FSI testing of 2D materials

FSI testing performed via atomic force microscopy (AFM) is widely used to measure the mechanical properties of 2D materials [27, 33-51]. In such tests, typically, a clamped

beam/drum-like sample of a 2D material of interest is fabricated in one of the following ways: (I) mechanical exfoliation of bulk layered materials onto a substrate with patterned cylindrical holes (or trenches) [33, 34, 50, 51, 73, 74]; (II) removing the substrate underneath the 2D material through etching [38]; and (III) transferring the 2D material onto a substrate with patterned cylindrical holes or trenches [11, 40, 41, 44, 52, 61, 75]. In all cases, the 2D material sample binds tightly with the substrate outside the patterned holes (or trenches) via vdW interactions [76]. The FS part of the 2D material over a cylindrical hole (or trench) is indented via an AFM tip, and the relationship between the indentation load (P) and displacement (δ_t) is recorded. The mechanical properties of the 2D material are then extracted by fitting the measured P-δ_t relationship with an analytical model. In such tests, the 2D material is deformed in two different modes (bending and stretching) based on the ratio of the indentation displacement to its thickness (δ_t/t).

Fig. 1 shows images of selected 2D materials measured with FSI [27, 33, 34, 43, 45, 46]; the properties obtained from such tests are listed in Table 1, and the associated geometrical parameters and loading conditions are listed in Table 2.

3.1 Existing analytical models for FSI

The FS portion of the 2D material over a trench or circular-hole in the substrate is treated as a doubly clamped beam (Fig. 2) or a circumferentially clamped drum (see Fig. 4); consequently, the analytical solutions about the beam bending and membrane stretching can be used to predict the indentation response of 2D materials [35, 62-70]. In the existing models for FSI, the selected 2D material is typically assumed to be clamped, the AFM tip idealized as a point force, and the sample deflection (δ) assumed to be equal to the AFM tip displacement (δ_t).

Note that the existing indentation analyses are not intended for atomically thin 2D materials; rather, they were originally developed for clamped continuum beams, plates and membranes. This discrepancy has led to some controversies in modeling the indentation response for mechanical properties characterization of 2D materials via FSI testing, as discussed below.

3.1.1 Doubly clamped beam model

In this model, the relationship between the indentation load and displacement of a 2D material over a trench in the substrate is modeled by Eq. (3) [27, 34-39, 53, 71]. For a small indentation displacement relative to the sample thickness, i.e., $\delta_i < t$, a 2D material subjected to FSI primarily undergoes bending. In this case, the P-δ_i relationship is approximately linear (see Fig. 3(a) [34]) with a slope estimated by Eq. (4). For pre-stretched 2D materials, the elastic modulus E cannot be directly obtained from Eq. (4) due to the substantial presence of the second term in Eq. (4), but E can still be extracted from the measured results by varying the geometric parameters (length L or thickness t). For example, E can be obtained from the fitted relationship between k and t/L, as shown in Fig. 3(b) [34, 36, 38]. In such cases, it is typically assumed that the 2D material is subjected to a constant pre-tension (T) that is insensitive to the thickness t but related to the vdW adhesion strength from the substrate sidewall (more details are given in section 3.4.2). A larger value t results in a smaller contribution of T to the FSI response and a more accurate estimate of E using Eq. (4) without the second term in the right-hand side. For example, the elastic modulus of a multilayered BP was extracted by fitting its measured P-δ_i curve with a linear relationship [27], resulting in E_{zig} = 58.6±11.7 GPa along the zigzag direction and E_{arm} = 27.2±4.1 GPa along the armchair direction.

The contribution from stretching, represented by the third term in Eq. (3), increases rapidly with increasing indentation displacement and becomes dominant when $\delta_i >> t$. In that case, the first term in Eq. (3) becomes negligible, and the P-δ_i relationship can be expressed as (5) [39]. Using Eq. (5), Li et al. [39] determined the elastic modulus of graphene to be E = 0.8 TPa.

3.1.2 Clamped drum model

In this model, the P-δ_i relationship is commonly modeled by Eq. (6) [33, 40-50]. When the indentation displacement is smaller than the sample thickness, the indentation stiffness arises primarily from bending and pre-tension, and the P-δ_i relationship is approximately linear with a slope as Eq. (7) [42, 48, 49] (see Fig. 4(b)). With the pre-tension T considered

insensitive to t [34, 42], E can be extracted from the relationship between k and t^3/a^2, as shown in Fig. 4(c). Using Eq. (7), Castellanos-Gomez et al. determined the elastic moduli of multilayer MoS_2 and mica to be 330 ± 70 GPa (with the number of layers n = 5-25) [42] and 202 ± 22 GPa (n = 2-14) [49], respectively; they also found that the elastic moduli of these 2D materials are not sensitive to their thickness t.

For $\delta_t >> t$, the first term in Eq. (6) becomes negligible, and the P-δ_t relationship is expressed as Eq. (8) [33, 41, 43-45, 62, 77-80] (see Fig. 5(a)). Fitting the measured P-δ_t relationship with Eq. (8), Lee et al. [33] reported E = 1.0 ± 0.1 TPa for monolayer graphene; for mono- and bi-layer MoS_2, Bertolazzi et al. [41] reported E = 270±100 GPa (n = 1) and 200±60 GPa (n = 2), and Liu et al. [43] reported E = 264±18 GPa (n = 1) and 231±10 GPa (n = 2) [43], respectively.

3.1.3 Fracture strength

In the FSI testing of a clamped 2D material, the intrinsic strength of a 2D material can be typically estimated using Eq. (10) [33, 41, 46, 49] (as shown in Fig. 5(b)). For example, Wang et al. [46] estimated the intrinsic strength of a multilayered BP as 25 GPa, and Bertolazzi et al. [41] reported the fracture strength of mono- and bi-layer MoS_2 as 22 GPa and 21 GPa, respectively.

Note that the existing indentation models are not intended for atomically thin 2D materials; rather, they were originally developed for clamped continuum beams, plates and membranes. This discrepancy has led to some controversy in modeling the indentation response for the mechanical property characterization of 2D materials via FSI testing, as discussed below.

3.2 Geometrical issues with FSI models

3.2.1 Clamped beam model

In continuum mechanics, a beam typically refers to as a slender structure with a large length-to-width ratio (L/W). In applying the clamped beam model to a 2D material under FSI, the plane strain modulus ($E^* = E/(1-\nu^2)$), instead of the elastic modulus E, is obtained using Eqs. (4) and (5) when $W > 5t$ [81]. However, the width of such clamped 2D materials

fabricated using a transfer technique is typically larger than their length [34, 39], sometimes several times larger [37, 53], as shown in Fig. 6(a). This geometric issue can induce substantial error in estimating the elastic modulus using Eqs. (4) and (5), which can be corrected using a doubly clamped plate model instead of the beam model mentioned previously. Consequently, the first term in Eq. (4) is rewritten as follows [37, 64]:

$$k = \frac{P}{\delta_t} = \frac{L}{12\alpha}\frac{E}{\left(1-\nu^2\right)}\left(\frac{t}{L}\right)^3 \tag{11}$$

where the geometrical parameter α depends on the ratio of L/W and the boundary condition (e.g., for $L/W = 1$, $\alpha = 0.0116$ for a simply supported plate, whereas $\alpha = 0.00724$ for a doubly clamped plate). Kunz et al. [37] determined the elastic modulus of clay tactoids (with $t < 25$ nm) as $E = 21\pm9$ GPa by fitting their measured P-δ_t relationship with Eq. (11) (see Fig. 6 (b)).

For a plate with a pre-stress or large indentation depth, the beam model (Eqs. (4) and (5)) may induce a large error in estimating elastic modulus; a more accurate solution can be determined using finite element method (FEM) simulations since more accurate analytical solutions are not available. For example, following the functional form of Eq. (6), the P-δ_t relationship of a pre-stretched plate can be expressed as follows:

$$P = \left[A\frac{Et^3}{L^2} + B\sigma_0 t\right]\delta_t + C\frac{Et}{L^2}\delta_t^3 \tag{12}$$

where the fitting parameters A, B and C can be determined from FEM simulations.

3.2.2 Clamped drum model

In the existing FSI models (e.g., (6)-(8)), the 2D materials are assumed to be subjected to a central point load, and the size effect of the indenter tip is neglected [62, 77-79]. However, the ratio of the sample size to tip radius, a/R, is finite in actual indentation tests. Begley et al. reported that the central point load assumption is effective only when $a/R > 30$ [65]. A comparison of the stretching term calculated using Eqs. (6)-(8) with FEM simulations shows an error of ~2% for $a/R = 50$, but this error increases to 16% with $a/R = 9$, indicating that the stretching term shown in the above equations is accurate only for very large a/R.

For relatively small a/R, it is suggested that the cubic term in Eqs. (6)-(8) should be

corrected by a factor of $(a/R)^4$ [65, 69]. Using MD simulations, Tan et al. [82] found that the elastic modulus of graphene is still overestimated for the case of $a/R = 6$ after introducing this correction factor. Due to the associated high computational cost, the tip radius R selected in MD simulations of spherical indentations should be as low as possible while having a similar ratio of a/R as experiments (e.g., a/R = 20-50 [33]); however, a very small R may cause an unrealistically high stress concentration; thus, $R \geq 2$ nm is typically selected in MD simulations. Even with R = 2 nm, a must be 100 nm to reach a/R = 50, which is still too expensive to obtain the effective mechanical properties of 2D materials from the MD results alone. To address this issue, Zhou et al. [16, 83-86] selected a cylindrical tip in MD simulations (instead of a spherical tip), in which the cylindrical surface is used to indent a rectangular 2D material sample. Both the sample and the cylindrical tip are subject to periodic boundary conditions along the axial direction of the tip, which not only eliminates the boundary effect along the lateral direction but also significantly reduces the computational cost. With this configuration, it was also found that the elastic modulus of graphene tends to be overestimated with a relatively small ratio of a/R [84, 85].

Komaragiri et al. [62] showed that the P-δ_t relationship of a pre-stretched, circular membrane is actually related to a/R and that when the pre-stress σ_0 is much larger than the membrane stress induced by P, the P-δ_t relationship can be expressed as follows [63, 87]:

$$P = \frac{2\pi\sigma_0 ta}{\ln(a/R)}\left(\frac{\delta_t}{a}\right) \tag{13}$$

Consequently, the FSI response of a pre-stretched 2D material (e.g., Eq. (8)) can be rewritten as follows [52]:

$$P = \frac{2\pi\sigma_0 ta}{\ln(a/R)}\left(\frac{\delta_t}{a}\right) + Et\xi^3 a\left(\frac{\delta_t}{a}\right)^3 \tag{14}$$

Since typically $a/R > 8$ in FSI testing (e.g., a/R = 9-50 [33, 44], see Table II), the pre-tension σ_0 in Eq. (14) is higher than that from Eq. (8), and this discrepancy increases with increasing a/R (e.g., σ_0 is doubled when a/R = 45 [33]).

The thickness of a 2D material has been widely discussed [17, 18, 88-95], and is often

treated as that of a thin plate (t_s) to be obtained from equation $t_s = \left(12D\left(1-\nu^2\right)/E^{2D}\right)^{\frac{1}{2}}$ in the continuum plate theory, where D is the bending stiffness and $E^{2D} = Et_s$ the tensile stiffness. The 2D elastic modulus Et and 2D intrinsic strength ($\sigma_{int}t$) of the material are associated with membrane stretching and Et^3 is associated with bending.

In summary, there can be a substantial size effect associated with the indenter tip in the FSI response of 2D materials, and the combined influence of this size effect and pre-tension should be further investigated.

3.3 Effect of boundary conditions in FSI models

3.3.1 Experimental investigations

Careful examination of typical FSI tests has revealed that 2D materials do not lie perfectly flat over a cylindrical hole/trench in a substrate and that a small portion of the 2D material close to the edge of the FS region is actually attached to the sidewall of the hole/trench (or it can be said that the FS portion is actually larger in size than the substrate hole/trench) [33, 41, 43-45, 74-76, 96, 97]. This sidewall adhesion is typically attributed to the vdW interaction between the FS 2D material and the substrate sidewall. Due to the nanoscale thickness of the 2D material, the strength of adhesion to the substrate is assumed to be sufficiently strong that the FS 2D material can be considered clamped at the boundary, as shown in Fig. 7 [74]. However, some recent experimental examinations have indicated that the portion of the 2D material adhered to the substrate sidewall can be delaminated by a small indentation load [44, 97]; thus, the conventional assumption of a clamped boundary in the existing FSI models might be inappropriate, as discussed below.

The Raman G-band frequency (ω_g) of graphene typically decreases with increasing in-plane tensile strain, but a contradictory result was reported by Kitt et al. [97]. They measured the variation of ω_g of an FS graphene membrane with an applied pressure difference (Δp) across it and found that there is an initial small increase in ω_g, which contradicts the expected increase in membrane stretching with Δp, as shown in Fig. 8. Kitt et al. hypothesized that this apparent paradox might be caused by the delamination of graphene from the substrate sidewall. They also found that the ω_g of the portion of graphene outside the hole decreases

with increasing Δp (see Fig. 9 [97]), suggesting that this outside portion is also stretched; therefore, the FS portion of the graphene was not well clamped.

Lin et al. [44] also found that the adhered portion of graphene could be delaminated from the substrate sidewall under a small indentation load (~100 nN) by monitoring the geometry of the FS region before and after loading (see Fig. 10). The initial topology of the FS of graphene is shown in Fig. 10(a), with a small portion of graphene (~6 nm) adhered onto the sidewall of the substrate; Fig. 10(b) shows the topology of the FS of graphene under a small indentation load, which clearly shows that the initially adhered portion has been delaminated. In addition, a much lower elastic modulus of graphene than its theoretical value (~1 TPa) was reported in their work, and the initial stage of the measured P-δ curve shows a much lower nonlinear behavior than that predicted by the existing indentation model (Eq. (8)) [44]. Therefore, the separation of the adhesive boundary of 2D materials in FSI tests seems possible, and the clamped boundary condition used in the existing models might be inappropriate.

3.3.2 Numerical investigations

Zhou et al. [83] investigated the FSI response of a graphene membrane with an adhesive boundary condition using an MD simulation in which the graphene membrane consisted of two portions: a vertical portion adhered to the substrate sidewall and a horizontally suspended portion, as shown in Fig. 11. The simulation results showed that a small indentation load can indeed delaminate the vertically adhered portion from the substrate sidewall and that the horizontal portion is stretched only after the adhered portion is fully delaminated. Using MD simulations, the vdW adhesion strength between the graphene and the substrate sidewall (SiO_2) was calculated as $\Delta\gamma$ = 0.1-0.2 J/m^2; it was also found that the carbon atoms in the adhered portion are delaminated layer by layer with no substantial sliding [83].

The FSI response of 2D materials with the adhesive boundary condition has also been investigated via FEM in our recent work [98]. As observed in the experiments, the FEM model of the sample consists of a large horizontal FS region and a small vertical portion that is adhered to the sidewall of the substrate-hole, as shown in Fig. 12(a). The vdW interaction

between the substrate sidewall and the adhered 2D material was simulated using a cohesive zone model, as shown in Fig. 12(b), with model parameters fitted from the MD simulation results. The vdW adhesion from the substrate sidewall induces a pre-tension in the FS portion represented by the FEM ($\varepsilon_0 = \Delta\gamma/Et$). The calculated P-δ_t curves of the 2D materials consist of two stages based on the evolution of their boundary condition (see Fig. 13) [98]. In stage I, the adhesive curve behaves less nonlinearly than the corresponding clamped curve, which indicates that the adhesive boundary condition reduces nonlinearity in the indentation response; in stage II, the adhesive curve is parallel with the clamped curve, suggesting that the sidewall-adhered portion has been fully delaminated. Clearly, the P-δ_t relationship at the sidewall delamination stage is not related to the elastic modulus of the 2D materials since the FS portion is not stretched; thus, their elastic moduli can be effectively determined only after the adhered portion is fully delaminated from the substrate sidewall.

3.4 Effect of prestress in FSI models

3.4.1 Experimental investigations

Tensile prestress (σ_0), which is commonly reported in the FSI testing of 2D materials, can be caused by the vdW interaction between the FS 2D material and the sidewall of the substrate. The prestress is typically determined from fitting the measured P-δ_t relationship with the existing indentation models (e.g., Eq. (8)), e.g., σ_0 = 0.07-1 Nm^{-1} for graphene [33, 34, 44, 50], σ_0 = 0.04-0.07 Nm^{-1} for graphene oxide (GO) [75], σ_0 = 0.02-0.2 Nm^{-1} for MoS_2 [41-43] and σ_0 = 0.06-0.2 Nm^{-1} for mica [49]. However, a contradictory finding is that σ_0 is also identified for an FS monolayer graphene grown by chemical vapor deposition (CVD) with many wrinkles or ripples [44]. Since the bending stiffness of graphene is negligible, a tensile prestress should be easily released by flattening out the wrinkles. Li et al. [39] proposed that there is no pre-tension in the FS graphene with wrinkles (observed from AFM images), and consequently, they neglected the first term in Eq. (8) when they measured the elastic modulus of CVD-grown graphene.

The reported tensile prestress σ_0 in FSI testing is not consistent with the observed tensile pre-strain ε_0, which is estimated from the length of the adhesive portion onto the substrate

sidewall. For example, Lee et al. [33] observed an adhesive length of approximately 2-10 nm in their FSI tests on graphene. The pre-strain was then estimated as ε_0 = 0.2-1% with a = 0.5 nm, corresponding to a tensile prestress of σ_0 = 0.7-3.4 Nm^{-1}, which is much larger than its counterpart obtained from Eq. (8). Lee et al. [33] attributed this difference to an existing pre-compression in FS graphene membranes, which might be caused by the lattice mismatch between graphene and the selected substrate (e.g., SiO_2). In the FS region of graphene, the pre-compression is released, and the resulting increase in the FS area is then adhered onto the substrate sidewall by vdW adhesion, which also induces a pre-tension in the FS portion.

Considering the effect of the adhesive boundary in the FSI testing of 2D materials, the pre-tension in an FS 2D material can be released by delaminating the adhered portion from the substrate sidewall [98]. In this case, this pre-tension may not substantially contribute to the indentation stiffness of a 2D material and cannot be effectively determined from the P-δ_t relationship. In addition, the FS portion of a 2D material should be larger than the substrate hole due to the delamination of the adhered portion. Therefore, a FS 2D material is more often subjected to a "pre-wrinkling strain" instead of a pre-tension.

3.4.2 Theoretical investigations

The vdW adhesion from the substrate sidewall causes a small adhered length (s_1) of the 2D material onto the substrate sidewall and simultaneously creates a pre-tension in the FS 2D material. For a cylindrical substrate hole, the biaxial pretension $\varepsilon_{rr} = \varepsilon_{\theta\theta} = \varepsilon_0 = s_1/a$ in the suspended 2D material ($r \le a$) and $\varepsilon_{rr} = \varepsilon_0 = s_1/a$ and $\varepsilon_{\theta\theta} = 0$ in the adhered portion ($a < r < a + s_1$), where ε_{rr} and $\varepsilon_{\theta\theta}$ are strains along the radial and circumferential directions, respectively. Schematic illustrations on the adhesive boundary condition and the associated pre-tension of a 2D material in FSI have been included on Fig. 14.

The value of s_1 related to the pre-tension can be determined through minimization of the system potential energy $dU_{tot}/ds_1 = 0$ [98]:

$$
\begin{aligned}
&U_{tot} = U_s + U_{adh} \\
&U_{adh} = -2\pi a s_1 \Delta\gamma \\
&U_s = U_{pre} = \pi a^2 t \frac{E}{1-\nu}\varepsilon_0^2 + \frac{1}{2}E\varepsilon_0 t\left((a+s)^2 - a^2\right)t \approx \pi \frac{Et}{1-\nu}s \\
&\frac{dU_{tot}}{ds_1} = -2\pi a\Delta\gamma + 2\pi\frac{Et}{1-\nu}s_1 = 0 \rightarrow s_1 = \frac{\Delta\gamma(1-\nu)}{Et}a
\end{aligned}
\tag{15}
$$

where U_s is the strain energy and U_{adh} the vdW adhesion energy from the portion of the 2D material adhered to the sidewall (s_1) of a cylindrical hole in the substrate. Initially, the strain energy U_s is mainly from the pretension energy U_{pre}, where the two terms on the right-hand of the third expression in Eq. (15) are associated with biaxial pretension in the suspended portion and pretension in the adhered portion, respectively. Due to the small value of s_1, the strain energy of the adhered portion is much lower than that of the suspended portion.

With the expression of s_1 (the last expression in Eq. (15)), the magnitude of pre-tension in an FS 2D material can be estimated from its vdW adhesion strength $\Delta\gamma$ with the substrate-sidewall as follows:

$$
\varepsilon_0 = \frac{s_1}{a} = \frac{\Delta\gamma(1-\nu)}{Et} \quad \text{and} \quad \frac{T}{\pi a} = \sigma_0 t = \frac{Et}{1-\nu}\varepsilon_0 = \Delta\gamma \tag{16}
$$

Thus, the pre-tension T is not sensitive to the thickness t of the 2D material but can be estimated from $\Delta\gamma$ using Eq. (16). Using MD simulations, $\Delta\gamma$ is estimated as 0.2 Jm^{-2} for graphene/SiO_2 [83], 0.26 Jm^{-2} for MoS_2/SiO_2 and 0.4 Jm^{-2} for graphene/graphene interfaces [99]. However, the pre-tension $\sigma_0 t$ in 2D materials determined from FSI tests typically deviates from the theoretical value predicted by Eq. (16), suggesting that it is not created by the vdW adhesion near the boundary of FS 2D materials. For example, the $\sigma_0 t$ of FS graphene from the experiments ($\sigma_0 t \leq 1$ N/m [33, 34, 44, 50]) is significantly higher than its theoretical value predicted by Eq. (16) ($\sigma_0 t \leq 0.2$ Nm^{-1}); although the $\sigma_0 t$ of FS MoS_2 is slightly higher than that of FS graphene from Eq. (16), the experimental value of $\sigma_0 t$ for FS graphene is significantly higher [41-43]; GO has a similar $\sigma_0 t$ as graphene (as determined from Eq. (16)), but the experimental value of $\sigma_0 t$ in FS GO ($\sigma_0 t \leq 0.07$ N/m [75]) is approximately one order of magnitude lower than that of FS graphene.

MD simulations are widely used to investigate the FSI response of 2D materials [16,

82-86, 100-104]. Neek-Amal et al. [101] and Tan et al. [82] calculated the FSI response of a clamped circular graphene membrane and found that the simulated P-δ_t relationship followed Eq. (8) closely. Although no pre-tension was assigned in the simulation, a linear term of δ_t was still obtained from fitting the simulated P-δ_t relationship with Eq. (8) [82, 83, 101], i.e., a pre-tension was determined from a graphene membrane with no pre-stretching using the existing indentation model. Their results indicate that the linear term of δ_t obtained from numerical fitting is not necessarily related to the prestress of the 2D material.

Using MD simulations, Lu et al. [99] and Zhou et al. [83] found that pre-tension in the FS of graphene with an adhesive boundary is quite small, e.g., $\varepsilon_0 \approx 3.0 \times 10^{-4}$ and 8.3×10^{-4} for SiO_2 and carbon-type sidewalls, respectively, which follows Eq. (16) closely. The corresponding prestress is roughly one order of magnitude smaller than its experimental value identified using the existing indentation model. In addition, the value of ε_0 is not sensitive to the length of the adhered or suspended portion; rather, it is related only to the adhesive strength $\Delta\gamma$ for a given material, suggesting that the pre-tension can be effectively predicted using Eq. (16) [83].

Similar to the FEM results shown in the preceding section, the MD simulation results also showed separation of the adhesive boundary under a small indentation load. Both the FEM and MD simulation results indicated that the pre-tension in the FS graphene can be rapidly released with boundary separation and do not affect the calculated P-δ_t relationship [83]. With the delamination of the adhesive portion, the FS portion is larger than the substrate hole, corresponding to a pre-compression in the 2D material. However, the adhesive P-δ_t relationship calculated using the FEM also follows the existing indentation model (as described by Eq. (8)), including both linear and cubic terms of δ_t, in agreement with the experimental results [98].

Therefore, separation of an adhesive boundary can also create a linear term of δ_t in the fitted P-δ_t relationship, indicating that the linear term of δ_t obtained from the measured P-δ_t relationship might not be related only to a tensile prestress in the 2D material.

3.5 Analytical model with adhesive boundary conditions

If an FS 2D material is larger than the substrate hole, it will adhere to the substrate sidewall, as observed in both experiments and the simulations. In FSI testing, the applied load results in either an increase in the strain energy (U_s) of the FS 2D material or a decrease in the adhesive energy (i.e., delamination of the adhered portion), both of which tend to increase the system energy. The pre-strain in the FS graphene varies with a delamination length x as follows:

$$\varepsilon_0 = \frac{s_1 - x}{a} \begin{cases} x \le s_1, \ \delta_t \le \delta_I \\ s_1 < x \le s, \ \delta_I < \delta_t < \delta_{II} \\ x = s, \ \delta_{II} \le \delta_t \end{cases} \tag{17}$$

where s is the total adhesive length and δ_I and δ_{II} are the indentation displacements corresponding to the delamination lengths of s_1 and s, respectively. Therefore, both the strain energy caused by the pre-tension and the adhesive energy vary with x as follows:

$$U_{pre} = \begin{cases} \frac{Et}{1-\nu}\left(\frac{s_1 - x}{a}\right)^2 & x < s_1 \\ 0 & x > s_1 \end{cases}, \ U_{adh} = \begin{cases} 2\pi a(x - s)\Delta\gamma & x < s \\ 0 & x > s \end{cases} \tag{18}$$

Pre-tension exists in the FS 2D material only when $\delta_t < \delta_I$; when $\delta_t > \delta_I$, the delaminated portion enlarges the radius of the suspended portion ($a + x$), i.e., $\varepsilon_0 < 0$.

With an adhesive boundary condition, the strain energy induced by the indentation load is similar to that of an FS film with continuously varying ε_0 under the clamped boundary condition, as follows:

$$U_{ind} = \int_0^{\delta_t} P_c d\delta_t, \ P_c = \alpha Et\varepsilon_0\left(\delta_t + x\right) + Et\xi^3 a^{-2}\left(\delta_t + x\right)^3 \ \ (P_c > 0) \tag{19}$$

where α is a geometrical parameter and the subscript c represents the clamped boundary condition. From the minimization of the total potential energy ($U_{tot} = U_{pre} + U_{ind} + U_{adh}$, $dU_{tot}/dx = 0$), the delaminated length x can be approximately expressed as a function of δ_t as follows [98]:

$$\frac{x}{a} \approx \begin{cases} \frac{\alpha}{4\pi}\left(\frac{\delta_t}{a}\right)^2 & (x \le s_1 \text{ and } x << \delta_t) \\ \frac{\alpha}{4\left(\alpha - \xi^3\right)}\left(\frac{\delta_t}{a}\right)^2 - \frac{\pi\Delta\gamma}{\left(\alpha - \xi^3\right)Et} & (s_1 \le x \le s \text{ and } x << \delta_t) \end{cases} \tag{20}$$

The work done by the indentation load is $W = U_{ind} + \Delta U_{pre} + \Delta U_{adh}$, where $\Delta U_{pre} = \pi Et\left(2s_1 x - x^2\right)/\left(1-\nu\right)$ and $\Delta U_{adh} = 2\pi a x \Delta\gamma$. The P-δ_t relationship can be estimated from the derivative of W with respect to δ_t as follows [98]:

$$P = \frac{dW}{d\delta_t} \approx A\delta_t + B\delta_t^3 \begin{cases} A = \alpha\Delta\gamma,\ B = \left(\xi^3 - \dfrac{\alpha^2}{4\pi\left(1-\nu\right)}\right)Eta^{-2},\ \delta_t \le \delta_I \\ A = \dfrac{2\pi\alpha\Delta\gamma}{\alpha - \xi^3},\ B = \left(\xi^3 - \dfrac{\alpha^2}{4\left(\alpha-\xi^3\right)}\right)Eta^{-2},\ \delta_I < \delta_t \le \delta_{II} \\ A = \alpha Et\left(s_1 - s\right)/a,\ B = Et\xi^3 a^{-2},\ \delta_{II} \le \delta_t \end{cases} \quad (21)$$

The value of the parameter α is further determined using the FEM based on the selected ratio of R/a. As described by Eq. (21), the P-δ_t relationship of an FS 2D material with the adhesive boundary includes three stages: the first two involve the delamination of the adhered portion from the substrate sidewall, in which the indentation load is related to the adhesive interaction (including the adhesive strength and adhesive length); in the third stage, the FS membrane is stretched and becomes larger than the substrate hole. Therefore, the elastic modulus of an FS 2D material can only be effectively determined from the third stage of the indentation P-δ_t curve.

3.6 Effect of tip-sample vdW interactions

3.6.1 Experimental investigation

In the conventional indentation tests performed via AFM, a negative indentation force ($P < 0$) occurs first as the AFM tip is attracted downward to contact the sample; after the indentation displacement is continuously increased, the indentation load smoothly changes to positive, and the initial contact point ($\delta_t = 0$) should be set as the beginning of a segment of positive P [105]. In the FSI test of a 2D material, the vdW interaction between the AFM-tip and the 2D material bends the 2D material upward towards the AFM tip [106, 107]. When δ_t is small, the vdW adhesion energy is negative and has a larger magnitude than the deformation energy of the 2D material; consequently, the beginning of a positive indentation load may not correspond to the true initial contact point ($\delta = 0$). Therefore, due to this vdW

effect, it is challenging to accurately determine the initial contact point of a 2D material in FSI tests, as shown in previous experiments [33, 44].

Lee et al. [33] and Lin et al. [44] found that there is an initial linear stage of the P-δ_i curve measured in the FSI test of graphene (different from the behavior predicted by Eq. (8)), which is hypothesized to be caused by the vdW interaction between the AFM tip and the graphene. Lee et al. [33] arbitrarily selected the midpoint of this linear stage as the initial contact point (i.e., P = 0, δ_i = 0). Lin et al. [44] conducted a more comprehensive investigation to determine the initial contact point of the 2D materials in FSI tests. They found that the elastic modulus E of graphene is highly sensitive to the initial contact point based on the existing indentation model and that a perturbation of 1 nm causes a change of ~10 GPa in E, which linearly increases with the right-shifting of the initial contact point (see Fig. 15). Using the beginning, midpoint and endpoint of the linear stage as the initial contact points, the elastic modulus of graphene is determined as $E \approx$ 417, 700, 935 GPa, respectively [44]. Due to the highly scattered experimental results, it is challenging to accurately determine the beginning, midpoint or endpoint of the initial linear stage, i.e., the initial contact point cannot be accurately identified. An incorrect assessment of initial contact can cause significant errors in the estimated elastic modulus of graphene.

To reduce the effect of the arbitrarily selected initial contact point on the elastic modulus, Lin et al. [44] proposed a new analytical indentation model (see the inset figure of Fig. 15 (b)) based on a selected reference point (P_0, δ_0) as follows:

$$P - P_0 = \sigma_0 t \pi \left(\delta - \delta_0\right) + \frac{Et\xi^3}{a^2}\left(\delta - \delta_0\right)^3 \tag{22}$$

They found that E is no longer sensitive to the selected initial contact point from Eq. (22) (~540 GPa, as shown in Fig. 15(b)), whereas it is significantly lower than the E reported by Lee et al. [33]. Relative to Eq. (8), Eq. (22) has two additional fitting parameters.

3.6.2 Numerical investigation

Although the AFM tip is typically assumed to be spherical and idealized as a point load in the existing FSI models [33], a spherical tip in MD simulations (see Fig. 16 (a)) can induce

a very high stress concentration [19, 108] and can even induce wrinkles [109] in the FS 2D material since the idealized tip radius is approximately one order of magnitude lower than its actual value. Due to the above issues, it can be highly challenging to determine the influence of tip-sample adhesion on the indentation response.

A cylindrical tip can apply a uniformly distributed load along the mid-line of the sample, as shown in Fig. 16 (b), which can eliminate the stress concentration or wrinkles induced by a spherical tip [16, 83-86, 110]. If the out-of-plane deformation of the portion in contact with the cylindrical tip is neglected, the FS graphene actually undergoes uniaxial tensile-strain deformation. Consequently, with a small indentation displacement, the strain energy of the membrane U_g in FSI is similar to its uniaxial tensile-strain energy (under the linear elastic assumption) [84, 85]:

$$\frac{U_g}{2WL}=\frac{1}{2}\frac{Et}{(1-\nu^2)}\varepsilon^2 \tag{23}$$

The in-plane stain ε can be easily estimated from the membrane deflection δ based on a geometrical relationship (assuming $\delta = \delta_t$):

$$\varepsilon=\sqrt{(\delta/L)^2+1}-1=k_0(\delta/L)^2\approx k_0(\delta_t/L)^2 \tag{24}$$

where $k_0 \approx 0.5$ is a fitting parameter. After substituting Eq. (24) into Eq. (23), the P-δ_t relationship of an FS membrane under a cylindrical tip is derived as follows:

$$P=dU_g/d\delta \text{ and } \frac{P}{W}=4k_0^2\frac{Et}{1-\nu^2}\left(\frac{\delta}{L}\right)^3\approx 4k_0^2\frac{Et}{1-\nu^2}\left(\frac{\delta_t}{L}\right)^3 \tag{25}$$

If a pre-strain ε_0 exists in the membrane, the δ-ε relationship can be rewritten as follows:

$$\varepsilon=\varepsilon_0+k_0(\delta/L)^2\approx\varepsilon_0+k_0(\delta_t/L)^2, \tag{26}$$

and the P-δ_t relationship becomes the following:

$$\frac{P}{W}=4k_0^2\frac{Et}{1-\nu^2}\left(\frac{\delta}{L}\right)^3+4k_0\frac{Et\varepsilon_0}{1-\nu^2}\left(\frac{\delta}{L}\right)\approx 4k_0^2\frac{Et}{1-\nu^2}\left(\frac{\delta_t}{L}\right)^3+4k_0\frac{Et\varepsilon_0}{1-\nu^2}\left(\frac{\delta_t}{L}\right). \tag{27}$$

Relative to the existing spherical indentation model, Eq. (27) has a similar functional form as Eq. (8) (including a linear term plus a cubic term). The clamped circular membrane under a central point load is exposed mainly to uniaxial tensile stress along the radial

direction, whereas the clamped rectangular membrane under a line load is exposed mainly to uniaxial tensile strain (perpendicular to the cylindrical axis). After we replace $Et/(1-\nu^2)$ by Et and select $W = L = R$, the cubic term in Eq. (27) is roughly equal to that in Eq. (8), but the coefficient of the linear term in Eq. (27) (e.g., $4k_0 \approx 2$) is lower than that in Eq. (8) (e.g., π).

The tip-graphene vdW interaction has a detectable effect on the graphene morphology at the initial contact point [83, 84], as shown in Fig. 17. The FS graphene remains flat without the vdW interaction, whereas the membrane is bent upward in the presence of vdW attraction (i.e., $\varepsilon > 0$ at $\delta_t = 0$) (see Figs. 17(a) and 17(b)). The vdW effect on the FS graphene is related to the pre-strain of the membrane: the vdW effect increases with increasing ε_0 when $\varepsilon_0 < 0$ (representing a larger size of the FS portion than the substrate hole) (see Fig. 17(c)), and the vdW effect decreases with increasing ε_0 when $\varepsilon_0 > 0$ (see Fig. 17(d)).

The vdW effect can be clarified via an energy analysis [83]. For a 2D material measured through FSI, the vdW interaction energy between the 2D material and indenter tip U_{vdw} is at the same level as the strain energy U_g when δ_t is small, and the expected system potential energy is $U_{tot} = U_g + U_{vdw}$. Fig. 18 shows the MD simulation results of U_{tot}, U_g and U_{vdW} varying with the in-plane strain ε normalized by the membrane area [84]. It is found that $U_g > 0$, $U_{vdW} < 0$ and $U_{tot} < 0$ at the initial contact point; consequently, the commonly used criterion for determining the initial contact point (in which $\delta_t = 0$ is set at $P \geq 0$) is not valid for 2D materials. Theoretically, the indentation depth at the minimum of U_{tot} should be set as the initial contact point, from which P monotonically increases with increasing δ_t ($dU_{tot}/d\delta_t = 0$ at $\delta_t = 0$), but this position is challenging to determine in experiments.

Due to the effect of the vdW interaction (see Fig. 18), the U_{tot}-δ_t relationship does not follow Eq. (23) closely, which indicates that the elastic modulus cannot be correctly determined from Eq. (23). The strain energy of graphene follows $U_g \propto \varepsilon^2$ quite well, and the elastic modulus determined from Eq. (23) is close to that obtained from uniaxial tension. With increasing in-plane strain ε, U_g rapidly increases, whereas U_{vdW} remains roughly constant. The vdW effect (represented by the ratio of U_{vdW}/U_g) rapidly decreases with increasing ε; consequently, the elastic modulus can be more accurately determined from a large indentation

load [84].

The accuracy in estimating the in-plane strain ε is also affected by the tip-sample vdW interaction, as shown in Fig. 19(a) [85]. From the MD simulations, Eq. (24) can describe the δ-ε relationship closely, but this equation is not consistent with the δ_t-ε relationship, which indicates that the tip-graphene vdW interaction produces a detectable deviation from δ_t to δ. Although this deviation decreases slightly with increasing L/R, the vdW effect mentioned above is not negligible in experiments (see Fig. 19(b) [85]). Consequently, Eq. (25) very accurately describes the P-δ relationship but not the P-δ_t relationship, resulting in an overestimation of the elastic modulus.

The P-δ_t relationship of non-prestretched graphene calculated from MD simulations follows Eq. (8) closely, leading to a fictitious pre-tension [82, 83, 101]. Zhou et al. [83] noted that the deviation of δ_t from δ might be the main cause for this fictitious pre-stress. Due to the tip-graphene vdW interaction, δ is larger than δ_t. Combining Eq. (25) with Eq. (27), a fictitious pre-tension is analytically derived as follows:

$$\varepsilon_0 = k\left(\frac{\delta^2}{L^2}\frac{\delta}{\delta_t} - \frac{\delta_t^2}{L^2}\right) \tag{28}$$

Therefore, the assumption of $\delta_t = \delta$ in the existing indentation model is, strictly speaking, inappropriate for 2D materials.

The pre-tension reduces the contact area A between the membrane and the tip, but the pre-compression (corresponding to a larger size of the FS membrane than the substrate hole) increases A. The vdW interaction scales with A. Consequently, the deviation of δ_t from δ also depends on the membrane prestress, decreasing with pre-tension ($\varepsilon_0 > 0$) but increasing with pre-compression ($\varepsilon_0 < 0$) [83]. Therefore, it could be beneficial to introduce a pre-tension in the measured 2D materials, which would reduce the tip-sample vdW effect and yield more accurate values of E and ε_0, as shown in Fig. 20.

3.7 Effect of material nonlinearity in FSI

Numerical simulations show that 2D materials behave highly nonlinearly (see Eq.) when the in-plane stress reaches their intrinsic strength [18, 21, 24-26, 30]. Using the FEM,

Lee et al. [33] studied the FSI responses of graphene with both linear and nonlinear models (see Fig. 21(a) and 21(b)). Although the FSI response of 2D materials is not sensitive to material nonlinearity with a small indentation displacement, the fracture strength is substantially overestimated using the linear elastic assumption (e.g., overestimated by ~30% [33]). In addition, the FEM results based on the linear elastic model of graphene match closely with the predictions of Eq. (10), which is consistent with the fact that Eq. (10) is derived with the linear elastic assumption leading to the overestimation of the fracture strength. Currently, there is no analytical solution for the relationship between the indentation load and the indentation stress that accounts for material nonlinearity.

Using a nonlinear elastic model of 2D materials, Lee et al. [33] and Wei et al. [60] estimated the fracture strength of graphene via an inverse analysis in conjunction with the FEM. The solution procedure is summarized as follows [33]: (I) The failure indentation load and displacement (P_f and δ_f) are measured from FSI tests via AFM; (II) The 2D material is modeled using a two-parameter nonlinear elastic model described by Eq. (1), where the nonlinear elastic coefficient D is obtained using the inverse analysis and the geometrical parameters and loading conditions are selected to be the same as those used in experiments. With a known E value and a series of assumed values of D, the corresponding indentation P-δ_f relationships are then calculated using the FEM; if the calculated values of P_f and δ_f are consistent with the experimental measurements, the input value of D is considered to be its true value; (III) The fracture strength is estimated from Eq. (2) after the value of D is determined.

According to the above procedure, Lee et al. [33] estimated the nonlinear elastic coefficient of graphene as D = -690 N/m, and its fracture strength and the corresponding fracture strain were then determined as σ_f = 130 GPa and ε_f = 0.25, respectively. This measured fracture strength is ~40% higher than the corresponding value calculated via DFT (90-98 GPa) [21, 22, 24]; however, the elastic modulus calculated from DFT is close to its experimental value reported by Lee et al. [33]. Based on numerical simulations, Zhou et al. [24] attributed the deviation of the measured σ_f from its DFT counterpart to the simplification

of the stress-strain (σ-ε) relationship of graphene with Eq. (1). In reality, the σ-ε relationship of graphene can be more accurately expressed as follows [24]:

$$\sigma = E\varepsilon + D'\varepsilon^2 + \lambda\varepsilon^3 \tag{29}$$

where D' and λ are higher-order parameters ($D' < 0$, and $\lambda > 0$). In other words, the nonlinear elastic coefficient D in Eq. is not a constant; rather, it decreases in magnitude with increasing in-plane strain ($D = D' + \lambda\varepsilon$). Consequently, the values of σ_f and ε_f of graphene increase with increasing ε from Eq. (2), as shown in Fig. 22, when normalized by their DFT counterparts (σ^* and ε^*). From Eq. (2), the value of σ_f can be changed by 100% in the present fitting range and matches its DFT value only when $\varepsilon \le 0.15$ (i.e., $\sigma_f/\sigma^* = 1$). For the loading range in the experiments, $\varepsilon \le 0.25$, and $\sigma_f/\sigma^* = 1.35$-1.4, as reported in the FSI tests [33]. Therefore, the value of σ_f is overestimated by the approach developed by Lee et al. [33]

Based on the σ-ε relationship modeled by the fifth-order anisotropic strain energy expression obtained from DFT calculations [22], Rassol et al. [61] calculated the relationship between the indentation stress and indentation load of graphene using the FEM; from the measured fracture indentation load, they estimated the fracture stress of graphene as σ_f = 90-94 GPa, in agreement with the intrinsic strength calculated from DFT [61]. Their results indicate that the measured fracture strength of graphene is close to its DFT value if the σ-ε relationship of graphene is accurately described with the FEM; on the other hand, the strength is overestimated if the two-parameter nonlinear model shown in Eq. (1) is used.

The Poisson ratio ν of 2D materials cannot be measured from FSI tests or other experimental approaches. The theoretical value of ν obtained from first-principle calculations is typically used, e.g., ν = 0.186 for monolayer graphene [33]. However, it is found that ν for graphene is not actually a constant; rather, it decreases with increasing tensile strain in the DFT calculations [21, 24], e.g., $\nu_{ac} = \nu_{zz} = 0.186$ with $\varepsilon = 0.01$, whereas $\nu_{ac} = 0.1$ and $\nu_{zz} = 0.05$ with $\varepsilon = 0.25$ (with subscripts *ac* and *zz* representing the armchair and zigzag directions, respectively). Currently, the possible effect of a varying ν on the indentation response has not been investigated.

3.8 Effect of material defects in FSI

CVD has been widely used to fabricate polycrystalline 2D materials that contain numerous lattice defects [20, 40, 61, 111-114], including grain boundaries that typically consist of 7-5 defects [61, 115-117].

3.8.1 Experimental investigations

Ruiz-Vargas et al. [52] measured the fracture load (P_f) of polycrystalline graphene and then estimated its fracture strength (σ_f) based on Eq. (10) (i.e., using the linear elastic assumption). By varying the distance between the indenting point and a grain boundary, they found that the fracture strength near the grain boundary is much lower (~35 GPa) than that in the grain interior (~84 GPa) and the theoretical lower limit of grain boundary strength (50-100 GPa) reported by Grantab et al. [118]. Recently, an even smaller theoretical lower limit of 38-100 GPa was reported on the basis of MD simulations of graphene bi-crystals under uniaxial tension [20]. Ruiz-Vargas et al. [52] speculated that there might be other defects (e.g., voids) in addition to grain boundaries to account for the discrepancy between the theoretical and experimental results, a conclusion that was supported by MD simulations of a bi-crystalline graphene including voids [52].

Rassol et al. [61] found that the relationship between fracture strength of a grain boundary (σ_f) and its tilt angle (θ) obtained from FSI tests is consistent with the corresponding theoretical result [20], e.g., σ_f increases with increasing θ (σ_f = 80-83 GPa for a high-angle grain boundary, whereas σ_f = 53-77 GPa for a low-angle grain boundary [61]). However, Lee et al. [40] reached a different conclusion by directly indenting a grain boundary via AFM, with the results showing that the σ_f of polycrystalline graphene is relatively insensitive to θ and is only approximately 20-40% lower than that of single-crystalline graphene [40]. In addition, the authors found that σ_f for polycrystalline graphene is also relatively insensitive to grain size, with σ_f = 98.5 GPa for some selected small grains and σ_f = 103 GPa for large grains (the difference is less than 5%) [40].

Lee et al. [40] speculated that a real grain boundary in polycrystalline graphene might be more complex than its theoretical model used in numerical simulations and consequently that the pre-stress created by a grain boundary could be released through its complex structure

(e.g., the out-of-plane deformation associated with a grain boundary can release some of the pre-stress created by 7-5 rings [119]). Thus, a grain boundary could have higher fracture strength and lower sensitivity to its tilt angle in experiments.

The indentation stress due to an AFM indenter is highly concentrated and rapidly diminishes with distance from the indenting position, and a grain boundary (or another defect) can also cause a stress concentration in polycrystalline graphene. These two effects might be coupled when indenting close to a grain boundary, which might account for the highly scattered fracture strength of polycrystalline graphene measured in FSI tests. For example, a grain boundary may not affect the σ_f when indenting far from it, i.e., polycrystalline graphene could have a similar σ_f as its single-crystalline counterpart; in contrast, a substantially reduced σ_f could occur when indenting close to a grain boundary.

3.8.2 Numerical investigations

(1) Single-crystalline graphene

In MD simulations, the stress components for atom i in graphene can be calculated using the following expression [19, 110, 120, 121]:

$$\sigma_{ab} = -\frac{N}{A_0 t}\left(m_i v_{ia} v_{ib} + \frac{1}{2}\sum_{j=1}^{n}\left(r_{ia} f_{ib} + r_{ja} f_{jb} \right) \right) \qquad a,\ b = x,\ y \tag{30}$$

where subscript i denotes atom i under observation, n is the number of atoms bonded to atom i (e.g., n = 3 for graphene), m is the atomic mass, v is the velocity of the atom, $A_0 t$ is the initial computational cell volume with in-plane area A_0 and thickness t = 0.335 nm, N is the total number of atoms in the computational cell, I and j are the atomic indices of two interacting atoms, and r and f are the coordinate and interaction force of the atom, respectively. There are three stress components, i.e., σ_{xx}, σ_{yy} and σ_{xy}, for graphene.

Using MD simulations, Han et al. [19] and Song et al. [119] calculated the fracture load of a clamped pristine graphene in FSI with a spherical tip. The fracture load P_f was found to increase with increasing tip radius R, e.g., P_f = 280 nN with R = 5 nm [19], and P_f = 60.4 nN with R = 1 nm [119]. In their simulations, the indentation stress of graphene was regarded as the maximum of the average in-plane stress of the atoms ($\sigma_{ind} = (\sigma_{xx}+\sigma_{yy})/2$ at the indentation

position, as shown in Fig. 23), and the fracture strength σ_f was regarded as the value of σ_{ind} at the maximum indentation load. The authors also showed that the calculated fracture strength of graphene slightly increases with decreasing R, e.g., σ_f = 105 GPa with R = 5 nm and σ_f = 120 GPa with R = 2 nm. For small R, the MD simulation prediction of σ_f is actually close to its theoretical value calculated using Eq. (10) (under the linear elastic assumption), e.g., σ_f = 118 GPa with R = 5 nm [19] and σ_f = 122 GPa with R = 1 nm [119]. From the MD simulations of in-plane stretching, the intrinsic strengths of graphene along the zigzag and armchair directions were reported as σ_{int}(ac) = 100 GPa and σ_{int}(zz) = 117 GPa, respectively [20]. Thus, for small R, the fracture strength of single-crystal graphene is slightly overestimated in the MD simulations of FSI, in which $\sigma_f = (\sigma_{int}(\text{ac}) + \sigma_{int}(\text{zz}))/2$ is assumed.

(2) Bi-crystalline graphene

In the MD simulations, the bi-crystalline model has been widely used to investigate the grain boundary effect on the indentation response of graphene [20, 118, 119, 122]. A grain boundary of bi-crystalline graphene consists of 5, 7 and 6 rings and is typically defined through the tilt angle θ [20]. Song et al. [119] reported that the facture loads of an armchair grain boundary with θ = 28.7° and a zigzag grain boundary with θ = 21.7° are 14% and 27% lower than that of the pristine graphene, respectively. Using the P_f-σ_f relationship of single-crystal graphene determined from MD simulations, the σ_f of bi-crystalline graphene can be further estimated from the value of P_f calculated using MD [19, 110].

Using MD simulations, Han et al. [19] calculated the σ_f-θ relationship of bi-crystalline graphene in spherical indentation and found that σ_f does not increase strongly with increasing θ, which is highly different from the corresponding result obtained from in-plane stretching [20]. Their simulation results also showed that when indenting close to a grain boundary, σ_f is sensitive to the position of indentation, as shown in Fig. 24 [19]. When the distance from the indenting position to a grain boundary is larger than the tip radius R, the grain boundary has little influence on σ_f [19]. The above results indicate that it is challenging to measure the fracture strength of polycrystalline graphene via spherical indentation when the AFM tip radius is far less than the grain size. For example, for grain radius a = 2 μm and AFM tip

radius R = 20 nm, the probability for the indentation position to fall within the distance of 20 nm from a grain boundary is quite low (< 2%).

Relative to tensile tests, FSI with a spherical tip overestimates the fracture strength of bi-crystalline graphene, which can be attributed to differences in the fracture mode [19]. In FSI tests, bi-crystalline graphene with a nucleated crack can still support the load without failure, and failure occurs only when the crack length reaches the level of indenter tip size, as shown in Fig. 25 [19], whereas in tensile tests, the sample fails soon after crack nucleation. This discrepancy can be attributed to the local stress concentration effect caused by both the indenter tip and grain boundary in FSI tests, resulting in lower crack nucleation energy in FSI than that in tensile tests. A lower strain energy in the sample results in a shorter crack as the strain energy is transferred into the crack surface energy, and thus, the nucleated crack is less likely to propagate in FSI than that in tensile tests, resulting a higher fracture strength.

These numerical investigations suggest a possible explanation for the highly scattered results of σ_f measured in the FSI tests. Han et al. concluded, for example, that the fracture strength of 2D materials cannot be accurately determined from FSI with a spherical tip [19].

(c) Polycrystalline graphene

In MD simulations, polycrystalline graphene is often built from four randomly oriented graphene grains with various shapes using the Voronoi tessellation method, and the low- or high-density regions near a grain boundary or junction are then eliminated via annealing [123, 124]. Sha et al. [125] showed that the calculated fracture indentation load P_f of polycrystalline graphene is lower than that of pristine graphene and is sensitive to the indenting position with respect to defects (grain boundaries, triple junctions and voids). P_f is significantly reduced if the indentation position is directly located on these defects, among which the triple junction is the weakest [125]. However, the grain boundaries or triple junctions in polycrystalline graphene created in their work consisted of not only 5, 7 and 6 rings but also 4 and 8 rings [125], which are unusual for grain boundaries in graphene [61, 115-117]. Thus, the MD simulations based on these unrealistic defects might not provide accurate estimates of the intrinsic fracture strength of polycrystalline graphene.

In summary, the MD simulation results show that the fracture strength of polycrystalline 2D materials cannot be effectively determined using FSI with a spherical tip. However, we note that all of these simulation results are obtained from a significantly smaller tip radius than that used in the experiments (e.g., $R \leq 5$ nm in simulations, in contrast to R = 16.5, 27.5 nm [33] and R = 115 nm [61] in experiments), which results in unrealistically high stress concentrations (which scale with R^{-2}) relative to the experiments. Consequently, σ_f is overestimated since the crack nucleation energy is underestimated. The affected area of the grain boundary is also significantly underestimated due to the small tip radius used in MD simulations (e.g., $R \leq 5$ nm). Therefore, the grain boundary strength might be more effectively determined by selecting a large tip. In addition, changing the tip geometry from a spherical shape to a cylindrical shape can significantly reduce the stress concentration near the tip and create a relatively uniform stress over the membrane [16, 85, 110], making the calculated fracture strength of the polycrystalline membrane less sensitive to the indenting position and closer to its intrinsic strength from in-plane stretching.

3.9 Effect of interlayer vdW interaction in FSI

Using FSI, Liu et al. [43] measured the elastic moduli (E_{tot}) of two-layer hybrid structures fabricated by graphene, MoS_2 and WS_2 monolayers and proposed that E_{tot} can be phenomenologically expressed as follows [43]:

$$E_{tot}t_{tot} = E_{bot}t_{bot} + \alpha E_{top}t_{top} \tag{31}$$

where t_{tot}, t_{bot} and t_{top} are the thicknesses of the whole structure, bottom layer and top layer, respectively; E_{bot} and E_{top} are the elastic moduli of the bottom layer and top layer, respectively; and α is the interaction coefficient describing the top layer contribution to E_{tot} ($0 < \alpha < 1$). They also showed that α depends on the interlayer vdW interaction but is not related to the indentation depth (or the in-plane strain). Therefore, FSI might actually provide a relatively simple approach to quantitatively predict the interlayer vdW interaction strength, and a higher α represents a larger strength. Liu et al. [43] indicated that slight interlayer sliding probably occurred in the test if $\alpha < 0.8$, e.g., α = 0.8, 0.75, 0.69 for MoS_2/WS_2, MoS_2/MoS_2 and MoS_2/graphene structures, respectively [43]. They also suggested that interlayer sliding might

be the main reason for the higher elastic moduli of the monolayer MoS_2 and WS_2 relative to their bulk values.

Using MD simulation, Neek-Amal et al. [101] and Zhou et al. [86] found that the elastic modulus of a bilayer graphene is actually lower than that of a monolayer graphene but that no interlayer sliding occurs in the bilayer graphene. Zhou et al. [86] proposed the following system strain energy of a multilayer graphene in FSI using a cylindrical tip:

$$U = \sum_{i=1}^{n} U_{gi} + \sum_{j=1,j=i+1}^{n-1} U_{ij} + U_{vdW} = U_0 + \frac{WL\varepsilon^2}{(1-\nu^2)}\left[E_{gn} + E_{i-j} + E_{vdW}\right] \quad (32)$$

where n is the number of layers in a multilayer graphene, U_0 is the system potential energy at the initial contact point, U_{gi} is the strain energy of the ith layer, U_{ij} is the interlayer interaction energy between the ith and jth layers, and U_{vdW} is the vdW interaction energy between the tip and the 1st layer. The elastic modulus of a multilayer graphene $E = E_{gn} + E_{i\text{-}j} + E_{vdw}$, where E_{gn}, $E_{i\text{-}j}$ and E_{vdw} are due to intralayer stretching, interlayer interaction and vdW interaction between the 1st layer and the tip, respectively. The effect of the tip-sample vdW interaction on the FSI response decreases with increasing n, as shown in Fig. 26, e.g., the effect is negligible on the topography of multilayer graphene when n = 4 [86]. Similar to monolayer graphene, the theoretical solution (Eq. (24)) is consistent with the ε-δ relationship of a multilayer graphene instead of its ε-δ_t relationship (see Fig. 27). For a multilayer graphene, δ is determined by the deflection of its bottom layer; thus, the discrepancy between δ and δ_t is caused by the interlayer vdW interaction.

Using Eq. (25), the elastic moduli of a multilayer graphene can be obtained either from the calculated P-δ_t or P-δ relationship, displayed as E_1^m and E_2^m (see Fig. 28), respectively [86]. Due to the interlayer vdW interaction, the elastic modulus of the multilayer graphene determined from FSI increases with n (with $n \le 4$), e.g., E_2^m increases by ~10% when n increases from 1 to 4, whereas the corresponding value determined from the tensile tests (E_0^m) is not sensitive to n. Although the tip-sample vdW effect decreases with increasing n, the elastic moduli of multilayer graphene are still overestimated from the P-δ_t relationship (i.e.,

$E_1^m / E_0^m > 1$), which is also attributed to the interlayer vdW interaction. Due to the coupling effect between the tip-sample and interlayer vdW interactions, bilayer graphene has the lowest elastic modulus from the P-δ_t relationship, in agreement with the experimental observations [43]. Note that the above simulation results are based on the assumption that the multilayer graphene thickness scales linearly with n.

From the aforementioned analysis, the lower elastic moduli of the bilayer 2D materials measured in FSI from the existing indentation model are caused by the coupling effect between the tip-sample and interlayer vdW interactions. Instead of interlayer sliding, the deviation of δ_t from δ might be the primary reason for the lower elastic moduli of bilayer structures, which can be corrected using the P-δ relationship instead of the P-δ_t relationship.

4. Indentation of 2D materials with a substrate

2D materials are almost always attached to a substrate via a vdW interaction in their important applications, e.g., nanoelectromechanical devices or graphene-reinforced polymers [126-133], and the vdW interaction might affect their mechanical behavior. Thus, studying the mechanical behavior of 2D materials directly mounted on a substrate is strongly relevant to their applications.

4.1 Existing indentation model

The mechanical properties of 2D materials can be measured via classic indentation tests by idealizing them as continuous thin films on a substrate with known elastic properties (e.g., SiO_2) [54, 57, 134]. The overall indentation load-displacement relationship of a thin-film on a substrate is measured via instrumented nanoindentation, and the overall indentation modulus is then determined using the existing indentation model as follows [135-140]:

$$P = \frac{4}{3}\frac{E_r \rho^3}{R} \tag{33}$$

where $E_r = E/(1-\nu^2)$ is the overall indentation modulus and ρ is the contact radius (the contact area $A = \pi\rho^2$). The relationship between the contact radius and the corresponding indentation displacement is typically estimated using the Hertz theory or the Oliver-Pharr method [140], e.g., the contact radius is approximated as $\rho = \rho_h = \sqrt{R\delta}$ using the Hertz theory (where ρ_h is

the Hertz contact radius). The overall indentation modulus of the composite structure is then regarded as a weighted average of the elastic moduli of both the film and substrate as follows [54, 134, 141]:

$$\frac{1}{E_r}=\frac{1-\nu_f^2}{E_f}\left(1-e^{-\zeta t/\rho}\right)+\frac{1-\nu_s^2}{E_s}e^{-\zeta t/\rho} \tag{34}$$

where ζ is a constant related to the tip geometry; E_f, ν_f and E_s, ν_s are the elastic moduli and the Poisson ratio of the film and substrate, respectively.

Zhang and Pan [54] measured the indentation responses of graphene with different numbers of layers (n = 1-5) mounted on SiO_2 (E_s = 70 GPa), and obtained E_r = 0.305, 0.12, 0.7 TPa for n = 1, 2 and 3, respectively. After decoupling their substrate contribution, the elastic moduli of graphene can be determined using Eq. (34), e.g., E_f = 0.89, 0.39, 0.05 TPa for mono-, bi- and tri-layer graphene, respectively. They speculated that the slip between graphene layers might occur in their tests, leading to apparently different elastic moduli with different numbers of layers of graphene.

Chen et al. [57] measured the indentation response of monolayer graphene mounted on polyethylene terephthalate (PET) (E_s = 3.7 GPa) and obtained an overall elastic modulus of E_r = 4.3 GPa, suggesting that graphene provides a weak enhancement to the PET substrate (E_r/E_s = 1.16). In comparison, graphene has been reported to provide a strong enhancement to a SiO_2 substrate, with E_r/E_s = 4.35 [54]. These results are at odds with our intuition that graphene should provide a larger enhancement to a compliant substrate (PET) than a stiff one (SiO_2). This result suggests that the existing indentation model (Eq. (34)) might not properly describe the indentation response of graphene with a substrate.

Niu et al. [56] proposed a possible explanation for the above paradox in that the contribution of a 2D material to the overall indentation response of a 2D material/substrate is too small to accurately determine its elastic modulus from the measured overall indentation modulus E_r. For example, for graphene/SiO_2, after substituting the modulus ratio E_f/E_s = 14, thickness t = 1 nm and contact radius ρ = 20 nm into Eq. (34), the first term on the right hand side of Eq. (34) (the 2D material contribution) accounts for less than 1% of the overall value, and the remaining contribution comes from its second term (the substrate contribution).

4.2 2D materials mounted on a very compliant substrate

To significantly increase the contribution of a 2D material to the overall indentation stiffness of the 2D material/substrate, Niu et al. [56] selected polydimethylsiloxane (PDMS), one of the most compliant materials, as the substrate to measure the elastic modulus of graphene via AFM indentation (see Figs. 29(a)). The elastic modulus ratio $E_r/E_s = 10^6$ for graphene/PDMS, and the graphene membrane provides a significant contribution to the overall indentation response, e.g., the indentation load increases by up to 14 times relative to that of PDMS, see Figs. 29(b) and 28(c) [56]. The indentation response of PDMS measured via AFM agrees closely with the existing indentation model, i.e., $P = c_1\delta^{1.5}$, where the fitting parameter $c_1 = E/(1-\nu^2)\cdot\tan\theta$ and θ is the equivalent half-conic angle of a pyramidal tip [140, 142, 143]. However, the indentation response of graphene/PDMS does not follow the existing model; rather, it follows the expression [56]

$$P = A\delta^{1.5} + B\delta^2 \tag{35}$$

where A and B are the fitting parameters depending upon the overall indentation stiffness of graphene/PDMS. The experimental values of A and B are relatively consistent and are insensitive to the tip radius: $A = 0.1202 \pm 0.0035$ nN/nm$^{1.5}$ and $B = (1.85 \pm 0.3) \times 10^{-3}$ nN/nm^2 [56].

From the measured indentation response of graphene/PDMS, the elastic modulus of graphene E_f can be determined via an inverse analysis [56, 144, 145]. Using the FEM, Niu et al. calculated the indentation responses of graphene/PDMS with a series of assumed elastic moduli of graphene E_f (in the range of $0.1 \le E_f \le 1.5$ TPa at an increment of 0.1 TPa) and a known E_s; using the least square fitting procedure, an empirical relationship was then established between the fitting parameters A and B in Eq. (35) and the input value of E_f in the FEM [56], i.e., $A = a_1(E_f)^2 + b_1(E_f) + c_1$ and $B = a_2(E_f)^2 + b_2(E_f) + c_2$, where a_i, b_i and c_i (i = 1, 2) are the fitting parameters. E_f was then determined by substituting the parameters A and B obtained from the measured P-δ relationship in experiments into the above empirical relationship: $E_f t = 329 \pm 28$ N/m, (see Fig. 29(d)), consistent with the corresponding value measured in FSI (~340 N/m [33]).

A 2D material can tightly adhere to an extremely compliant and highly stretchable substrate via vdW interactions, and consequently, the 2D material can be broken in an indentation test performed via AFM. Recently, Niu et al. [55] proposed a new approach for determining the fracture strength of a 2D material from its indentation response on PDMS. With $P = P_f$ ($\delta_t = \delta_f$), P sharply decreases to the corresponding P of pure PDMS at δ_f, as shown in Fig. 30, indicative of graphene fracture [55]. Similar to the analysis of the fracture strength of a 2D material used in FSI [33, 60], the graphene membrane on PDMS can also be modeled using a two-parameter nonlinear elastic model described by Eq. (1), where E_f is known (determined from the P-δ_t relationship of graphene/PDMS with a small δ_t), but the nonlinear elastic parameter D needs to be assumed; with a known E_s, the corresponding indentation P-δ_t relationships of graphene/PDMS are calculated using the FEM, and the input value of D is considered to be its true value if the calculated values of P_f and δ_f are consistent with the experimental results; the fracture strength of graphene can then be estimated using Eq. (2) after the D is obtained. According to this procedure, Niu et al. [55] obtained the fracture strength of monolayer graphene as σ_f = 38.9 N/m (corresponding to 112 GPa with t = 0.335 nm) and the corresponding fracture strain as ε_f = 0.23, which are slightly lower than the corresponding values reported from FSI (σ_f = 42 ± 4 Nm^{-1} and ε_f = 0.25 [33]). This measured value of σ_f is still higher than its theoretical value calculated from DFT (σ_{int} = 31 Nm^{-1} [21, 22]), which can be attributed to the simplification of the stress-strain relationship of graphene with a two-parameter model (Eq. (1)).

4.3 Effect of the modulus ratio E_f/E_s in indentation tests

Niu et al. [56] proposed that the existing indentation model might be inappropriate for describing the indentation response of graphene/substrate with a large modulus ratio of E_f/E_s, which might explain why the enhancement of graphene on a PET substrate is lower than that on a SiO_2 substrate (E_f/E_s = 14 and 230 for graphene/SiO_2 and graphene/PET, respectively). These results indicate that the modulus of graphene E_f determined from the indentation response of graphene/substrate may be highly sensitive to E_f/E_s.

Using the FEM, Cao et al. [58, 59] recently investigated the indentation response of 2D

materials mounted on various substrates (E_f/E_s = 10-10^6, which covers all possible combinations of the 2D materials and their substrates used in the experiments). It was found that the indentation response of the 2D material/substrate depends strongly on E_f/E_s: For a small E_f/E_s ($E_f/E_s \leq 10^2$), the overall indentation response of the 2D material/substrate follows the existing indentation model (Eq. (33)) closely, and an overall indentation modulus E_r can be effectively determined using the Hertz solution; however, for a large E_f/E_s (e.g., $E_f/E_s \geqslant 10^3$), the indentation response of the 2D material/substrate is inconsistent with the existing indentation model (Eq. (33)), and the E_r determined using the Hertz solution is not a constant but increases with δ_h, as shown in Fig. 31 [58].

The discrepancy between the calculated P-δ relationship from the FEM and the predictions from the theoretical models is typically attributed to an incorrect estimation of the contact radius in the model [137, 138, 146, 147]. Using the FEM, Cao et al. calculated the true contact radius of a 2D material/substrate and found that its contact radius is not only related to δ but also depends on E_f/E_s, as follows [58]:

$$\frac{\rho}{\rho_h} \approx \begin{cases} 1-k_1\delta & \lambda \leq 100 \\ k_2\delta^{\beta} \quad \beta=\beta\left(E_f/E_s\right) & \lambda \geq 10^4 \end{cases} \tag{35}$$

For a moderate $\lambda = E_f/E_s$ (e.g., $500 \leq \lambda \leq 5000$), the ρ-δ relationship undergoes a transition from a linear to a power-law relationship. When λ increases to 10^6, ρ reduces by ~72% (the contact area decreases by ~93%). While ρ is essentially not related to the material properties on the basis of the continuum contact theory, it is found to be a function of λ for the 2D material/substrate, suggesting that the existing indentation model built from the continuum contact theory is indeed inappropriate to describe the indentation response of the 2D material/substrate.

According to the value of λ, the existing indentation model (Eq. (33)) is appropriate for graphene/SiO_2 but not for graphene/PET. In addition, it is extremely challenging to accurately determine E_f from the measured E_r of graphene/SiO_2 using Eq. (34) since the E_r determined using Eq. (33) is almost equal to E_s, as shown in Fig. 31 [58], i.e., the contribution of the graphene to the overall indentation response is almost negligible.

To accurately determine the mechanical property of a 2D material from the overall indentation response of the 2D material/substrate, the 2D material must have a detectable contribution to the overall indentation stiffness, which can be clearly shown using the stain energy ratio of the 2D material to the whole composite structure $U_f/(U_s+U_f)$, e.g., $U_f/(U_s+U_f) \approx$ 0.02 and 0.1 for graphene/SiO_2 and graphene/PET, respectively. When $\lambda = 10^4$-10^6, $U_f/(U_s+U_f)$ increases to 0.28-0.33 and becomes insensitive to the indentation displacement, as shown in Fig. 32(a) [58]. Therefore, although the existing indentation model might not be appropriate for describing the P-δ relationship of a 2D material/substrate with a large λ, the elastic modulus of a 2D material might be effectively determined from an inverse analysis using the FEM [59]. Considering some of the most compliant substrate materials (e.g., PDMS), it can be estimated that $\lambda = 10^4$-10^6 for all the reported 2D materials (e.g., graphene, layered MoS_2 and BP). Using the FEM, the fitting parameters A and B in Eq. (35) can be empirically expressed as $A = a_1(\lambda)^2 + b_1(\lambda) + c_1$ and $B = a_2(\lambda)^2 + b_2(\lambda) + c_2$, as shown in Fig. 32(b). Following Niu et al. [56], the elastic modulus of a 2D material can be determined from its P-δ relationship on PDMS.

4.4 Effect of material nonlinearity in indentation tests

Using the FEM, Niu et al. [56] further studied the effect of material nonlinearity on the indentation response of graphene/PDMS. Their results showed that with a small indentation depth, the nonlinearity of graphene has a negligible effect on the indentation response of graphene/PDMS, suggesting that the nonlinearity of a 2D material does not affect its elastic modulus estimated from the P-δ_t relationship of the 2D material/PDMS; with a large indentation depth, the indentation response of graphene/PDMS becomes sensitive to the nonlinearity of graphene, which is appropriately simulated using a nonlinear elastic model (e.g., Eq. (1)), suggesting that nonlinearity should be considered for estimating the fracture stress of graphene from the indentation response of graphene/PDMS [56].

The experimental results showed that a small discrepancy exists between the indentation loading and unloading curves of graphene/PDMS (i.e., a small hysteresis loop arises, see Fig. 29), suggesting that the viscous feature of PDMS has a weak effect on the indentation

response of graphene/PDMS [55]. It is widely accepted that for small deformations, PDMS behaves more like a linear elastic material than a viscoelastic material [148-150]. Using the FEM, Niu et al. [55] compared the indentation responses of graphene/PDMS based on different material models of PDMS, including the linear elastic, neo-Hookean and standard linear solid models; they found that the nonlinear behavior of PDMS (e.g., the viscoelastic and hyperelastic features) has a negligible effect on the indentation response of graphene/PDMS, as shown in Fig. 33. In addition, the authors found that the indentation deformation of pure PDMS (with $\delta_i = \delta_f$) can be fully recovered after unloading. These results indicate that PDMS can be idealized as a linear elastic material in the indentation tests of graphene/PDMS.

4.5 Interfacial effect in indentation tests

From the indentation testing, Niu et al. [55] found that there is no interfacial debonding or slippage of the graphene/PDMS interface, even at the failure strain of graphene ($\varepsilon_f = 0.23$ for graphene), which is at odds with its interfacial behavior measured in the uniaxial tensile testing (e.g., the interfacial sliding starts at ε = ~0.3% [151, 152]). In addition, the load transfer mechanism across the graphene/PDMS interface in the indentation testing is different from that in the tensile testing.

The graphene/substrate interfacial strength has been widely investigated through tensile testing [130, 131, 151]. Under uniaxial tension, the tensile strain is uniformly transferred from the substrate to graphene across the entire interface from the edge to the center. The vdW bond energy density between graphene and its substrate was reported as 0.1-0.4 Jm^{-2} based on the MD simulations [74, 99, 153]; an adhesion energy density of approximately 0.1 Jm^{-2} can theoretically transfer a tensile strain of ~2.5% (with $E_g t$ = 340 N/m and t = 0.335 nm) based on the balance between the vdW adhesion energy and the strain energy. Jiang et al. [151] found that the strain for the onset of interfacial sliding is actually very small (~0.3%) (starting from the edge of graphene), whereas the maximum strain transferred across the interface (at the center of graphene) can reach 1.2-1.6%. The small interfacial sliding strain observed in the experiments can be attributed to the interface edge effect, which might be caused by a

higher chemical activity of the edge atoms of graphene due to their lower coordination number (dangling bonds).

In the indentation testing of graphene/PDMS, the in-plane strain (ε_r) of graphene is highly nonuniform; it is maximized at the indenting point, rapidly decreases with the radial distance r ($\varepsilon_r = \varepsilon_f$ at $r = 0$ and diminishes at a lower rate when $r > 2$ μm; see Fig. 33), suggesting that there is no edge debonding or slippage since the sample size is typically much larger than 2 μm (i.e., the graphene membrane is under a clamped boundary condition) [55]. Niu et al. [55] also found that the in-plane stretching of graphene is directly created by the indentation load but is not transferred from the substrate across the graphene/PDMS interface; on the other hand, the substrate is also directly deformed by the indentation load. The portion of the substrate close to the indenter tip is vertically compressed and laterally extended due to the Poisson effect of this compression. Consequently, the graphene/PDMS interface needs only to transfer the load difference between graphene and its substrate to maintain deformation compatibility across the interface. The above analysis provides an explanation as to why there is no interface sliding/debonding even though the graphene membrane is subjected to a relatively high in-plane strain.

4.6 Advantages and disadvantages of indentation testing of 2D materials with a substrate

Relative to the mechanical properties of graphene measured in FSI [33], a similar value of $E_f t$ and a slightly lower value of $\sigma_f t$ (~10% lower) are obtained from the indentation testing of graphene/PDMS [55, 56]. The indentation test of 2D materials with a PDMS substrate shows some advantages/disadvantages over the FSI testing of 2D materials, as follows:

(I) For a given deflection of graphene δ, the indentation displacement (δ_i) is much higher in the former test than in the latter test, e.g., δ_i = 200-300 nm when measuring the elastic modulus of graphene in the former test, whereas δ_i = 20-100 nm in the latter test; the sample size is actually much larger in the former test than in the latter test, e.g., $a > 100$ μm in the former test [55, 56], whereas $a \leq 1$ μm in the latter test [33, 40, 44]. Therefore, the former test is expected to provide a higher measuring accuracy than the latter test.

(II) Due to the substrate constraint effect (e.g., graphene can be strongly bonded with PDMS), the sample stiffness is much higher in the former test than in the latter test. Consequently, the tip-graphene vdW interaction has a negligible effect on sample deformation;

therefore, the initial contact point can be more accurately determined in the former test.

(III) In the former test, the boundary conditions of the 2D materials are relatively simple and easily described (i.e., with a clamped boundary condition), whereas in the latter test, the 2D material is actually under an adhesive boundary condition, which is much more complex and challenging to accurately describe.

(IV) In the former test, the elastic modulus of graphene (E_f) characterization not only is related to the indentation test of the 2D material/PDMS but also requires the mechanical properties of the PDMS substrate (E_s); in addition, an empirical P-δ_t relationship needs to be established for graphene/PDMS using the FEM since its analytical solution is not available. In the latter test, there is an analytical solution for the P-δ_t relationship (Eq.(8)), reducing the complexity of determining E_f. However, this analytical solution was originally intended for continuous films, with assumptions that might not be appropriate for 2D materials.

In summary, the indentation response of 2D material/PDMS can be more accurately measured than the FSI response of a 2D material; in contrast, it is simpler to determine the elastic modulus of a 2D material from FSI testing than from instrumented indentation of the 2D material/PDMS.

5. Summary and selected topics for further investigation

Indentation testing has often been adopted as the preferred method for mechanical property characterization of 2D materials, with significant progress made over the past decade, both theoretically and experimentally. Based on the issues in the existing indentation characterization of 2D materials, selected topics of interest as an outlook for future studies are summarized as follows:

(I) Establishing a more effective FSI model

In the present work, we reviewed the effects of the following issues on the FSI testing of 2D materials, including the effects of sample geometry, boundary conditions, pre-stress, material nonlinearity, defects (e.g., grain boundaries), and vdW interactions with an AFM tip and with a substrate near the boundary of the FS region. Due to these issues, the mechanical properties of 2D materials may not be properly characterized using the existing indentation models, including the clamped beam/drum model. Therefore, more appropriate indentation models for FSI should be established to address these issues.

(II) Designing a more appropriate FSI experimental configuration

In addition to correcting the existing indentation model, new FSI experimental configurations for 2D materials should also be developed to reduce the effects of the aforementioned issues on FSI testing. For example, fabricating a clamped, pre-stretched FS 2D material can effectively increase the accuracy when determining its elastic modulus via FSI testing. Recently, Yang et al. [53] developed a new fabrication method of FS 2D materials on the basis of substrate self-cracking, in which a clamped, pre-stretched, FS film of GO is fabricated, as shown in Fig. 34. A pre-tension can be induced into the FS GO film via substrate self-cracking created during a precipitation process. No portion vertically adhered to the substrate sidewall was observed in their experiments, suggesting that the FS GO film is truly under a clamped boundary condition; thus, the elastic modulus of GO film can be more accurately determined using the existing indentation model. However, wrinkles were observed in their samples, which can be attributed to the Poisson effect of pre-tension induced by substrate self-cracking, as is commonly observed in stretched continuous elastic sheets [154, 155] and whose effect on the indentation response of a pre-stretched FS sample is not yet clear. Another solution to eliminate the effect of the aforementioned issues might be applying a pressure difference across FS 2D materials over a microchember, and the FSI testing is then performed on the pressurized membranes [80]. This applied pressure difference not only delaminates the adhesive boundary of FS 2D materials but also introduces a true tensile pre-strain in these samples tested in FSI [80, 97], as shown in Fig. 35. However, the new indentation model for this bulged membrane has been not available, which should be developed in the near future.

(III) Developing a more effective analytical model predicting fracture strength

Although the fracture load of an FS 2D material can be easily measured using the indentation technique, an effective relationship between its fracture strength and fracture load is still not available. Simulation results show that existing linear and nonlinear elastic models overestimate the fracture strength of 2D materials, which can be attributed to the discrepancy between their true stress-strain curve (calculated by DFT) and the curve described by the existing theoretical models. Defects make the fracture behavior of polycrystalline 2D

materials much more complex due to the coupling effect of the stress concentrations caused by both the indenter tip and defects. From both the numerical and experimental results, the reported fracture strength of polycrystalline 2D materials is highly scattered; thus, the fracture strength characterization of polycrystalline 2D materials is currently one of the most challenging issues in indentation testing of 2D materials. Instead of using a spherical tip, a cylindrical tip can effectively improve the accuracy in determining the fracture strength of polycrystalline 2D materials, which might be considered in the future.

(IV) Developing an analytical indentation model for 2D material/PDMS

With a very large modulus ratio λ ($10^4 < \lambda \leq 10^6$), the ratio U_f/U_{tot} converges to a constant, suggesting that it is possible to determine the mechanical properties of 2D materials from the overall indentation testing of the 2D material/substrate. Due to the substrate constraint effect in indentation testing, the issues associated with FSI (mentioned previously) do not arise; thus, the indentation response of the 2D material/substrate can be more accurately measured. However, an analytical relationship between the overall indentation load of the 2D material/substrate and the elastic modulus of the 2D material is still lacking; such a relationship would provide a useful guideline for the characterization of the mechanical properties of 2D materials.

Acknowledgment

GC acknowledges financial support provided by the Ministry of Science and Technology of China (2015GB113000). HG acknowledges support by NSF under grant CMMI-1634492.

Reference

[1] Geim AK. Graphene: Status and Prospects. Science. 2009;324:1530-4.

[2] Radisavljevic B, Radenovic A, Brivio J, Giacometti V, Kis A. Single-layer MoS2 transistors. Nature Nanotechnology. 2011;6:147-50.

[3] Georgiou T, Jalil R, Belle BD, Britnell L, Gorbachev RV, Morozov SV, et al. Vertical field-effect transistor based on graphene-WS2 heterostructures for flexible and transparent electronics. Nature Nanotechnology. 2013;8:100-3.

[4] Wang QH, Kalantar-Zadeh K, Kis A, Coleman JN, Strano MS. Electronics and optoelectronics of two-dimensional transition metal dichalcogenides. Nature Nanotechnology. 2012;7:699-712.

[5] Li LK, Yu YJ, Ye GJ, Ge QQ, Ou XD, Wu H, et al. Black phosphorus field-effect transistors. Nature Nanotechnology. 2014;9:372-7.

[6] Kim J, Baik SS, Ryu SH, Sohn Y, Park S, Park BG, et al. Observation of tunable band gap and anisotropic Dirac semimetal state in black phosphorus. Science. 2015;349:723-6.

[7] Pereira VM, Castro Neto AH. Strain Engineering of Graphene's Electronic Structure. Phys Rev Lett. 2009;103:046801.

[8] Ni GX, Yang HZ, Ji W, Baeck SJ, Toh CT, Ahn JH, et al. Tuning Optical Conductivity of Large-Scale CVD Graphene by Strain Engineering. Adv Mater. 2014;26:1081-6.

[9] Pu J, Li LJ, Takenobu T. Flexible and stretchable thin-film transistors based on molybdenum disulphide. Phys Chem Chem Phys. 2014;16:14996-5006.

[10] Jiang JW. Phonon bandgap engineering of strained monolayer MoS2. Nanoscale. 2014;6:8326-33.

[11] Castellanos-Gomez A, van Leeuwen R, Buscema M, van der Zant HSJ, Steele GA, Venstra WJ. Single-Layer MoS2 Mechanical Resonators. Adv Mater. 2013;25:6719-23.

[12] Amorim B, Cortijo A, de Juan F, Grushine AG, Guinea F, Gutierrez-Rubio A, et al. Novel effects of strains in graphene and other two dimensional materials. Phys Rep. 2016;617:1-54.

[13] Yang YC, Li X, Wen MR, Hacopian E, Chen WB, Gong YJ, et al. Brittle Fracture of 2D MoSe2. Adv Mater. 2017;29.

[14] Zhang P, Ma LL, Fan FF, Zeng Z, Peng C, Loya PE, et al. Fracture toughness of graphene. Nat Commun. 2014;5.

[15] Lindahl N, Midtvedt D, Svensson J, Nerushev OA, Lindvall N, Isacsson A, et al. Determination of the Bending Rigidity of Graphene via Electrostatic Actuation of Buckled Membranes. Nano Lett. 2012;12:3526-31.

[16] Zhou L, Wang Y, Cao G. Elastic properties of monolayer graphene with different chiralities. J Phys-Condens Mat. 2013;25:125302.

[17] Xiong S, Cao G. Bending response of single layer MoS2. Nanotechnology. 2016;27:105701.

[18] Xiong S, Cao G. Continuum thin-shell model of the anisotropic two-dimensional materials: Single-layer black phosphorus. Extreme Mechanics Letters. 2017;15:1-9.

[19] Han J, Pugno NM, Ryu S. Nanoindentation cannot accurately predict the tensile strength of graphene or other 2D materials. Nanoscale. 2015;7:15672-9.

[20] Wei YJ, Wu JT, Yin HQ, Shi XH, Yang RG, Dresselhaus M. The nature of strength enhancement and weakening by pentagon-heptagon defects in graphene. Nature Materials. 2012;11:759-63.
[21] Cao GX. Atomistic Studies of Mechanical Properties of Graphene. Polymers. 2014;6:2404-32.
[22] Wei XD, Fragneaud B, Marianetti CA, Kysar JW. Nonlinear elastic behavior of graphene: Ab initio calculations to continuum description. Phys Rev B. 2009;80:205407.
[23] Liu F, Ming PM, Li J. Ab initio calculation of ideal strength and phonon instability of graphene under tension. Phys Rev B. 2007;76:064120.
[24] Zhou L, Cao G. Nonlinear anisotropic deformation behavior of a graphene monolayer under uniaxial tension. Phys Chem Chem Phys. 2016;18:1657-64.
[25] Xiong S, Cao G. Molecular dynamics simulations of mechanical properties of monolayer MoS2. Nanotechnology. 2015;26:185705.
[26] Wei Q, Peng XH. Superior mechanical flexibility of phosphorene and few-layer black phosphorus. Appl Phys Lett. 2014;104:251915.
[27] Tao J, Shen WF, Wu S, Liu L, Feng ZH, Wang C, et al. Mechanical and Electrical Anisotropy of Few-Layer Black Phosphorus. Acs Nano. 2015;9:11362-70.
[28] Cooper RC, Lee C, Marianetti CA, Wei XD, Hone J, Kysar JW. Nonlinear elastic behavior of two-dimensional molybdenum disulfide. Phys Rev B. 2013;87:035423.
[29] Lu Q, Huang R. Nonlinear Mechanics of Single-Atomic-Layer Graphene Sheets. International Journal of Applied Mechanics. 2009;1:443-67.
[30] Cadelano E, Palla PL, Giordano S, Colombo L. Nonlinear Elasticity of Monolayer Graphene. Phys Rev Lett. 2009;102:235502.
[31] Sfyris D, Sfyris GI, Galiotis C. Curvature dependent surface energy for a free standing monolayer graphene: Some closed form solutions of the non-linear theory. International Journal of Non-Linear Mechanics. 2014;67:186-97.
[32] Sfyris D, Sfyris GI, Galiotis C. Constitutive modeling of some 2D crystals: Graphene, hexagonal BN, MoS2, WSe2 and NbSe2. Int J Solids Struct. 2015;66:98-110.
[33] Lee C, Wei XD, Kysar JW, Hone J. Measurement of the elastic properties and intrinsic strength of monolayer graphene. Science. 2008;321:385-8.
[34] Frank IW, Tanenbaum DM, Van der Zande AM, McEuen PL. Mechanical properties of suspended graphene sheets. Journal of Vacuum Science & Technology B. 2007;25:2558-61.
[35] Pruessner MW, King TT, Kelly DP, Grover R, Calhoun LC, Ghodssi R. Mechanical property measurement of InP-based MEMS for optical communications. Sensor Actuat a-Phys. 2003;105:190-200.
[36] Traversi F, Guzman-Vazquez FJ, Rizzi LG, Russo V, Casari CS, Gomez-Navarro C, et al. Elastic properties of graphene suspended on a polymer substrate by e-beam exposure. New Journal of Physics. 2010;12:023034.
[37] Kunz DA, Max E, Weinkamer R, Lunkenbein T, Breu J, Fery A. Deformation Measurements on Thin Clay Tactoids. Small. 2009;5:1816-20.
[38] Gomez-Navarro C, Burghard M, Kern K. Elastic properties of chemically derived

single graphene sheets. Nano Lett. 2008;8:2045-9.
[39] Li P, You Z, Haugstad G, Cui TH. Graphene fixed-end beam arrays based on mechanical exfoliation. Appl Phys Lett. 2011;98:253105.
[40] Lee GH, Cooper RC, An SJ, Lee S, van der Zande A, Petrone N, et al. High-Strength Chemical-Vapor Deposited Graphene and Grain Boundaries. Science. 2013;340:1073-6.
[41] Bertolazzi S, Brivio J, Kis A. Stretching and Breaking of Ultrathin MoS2. Acs Nano. 2011;5:9703-9.
[42] Castellanos-Gomez A, Poot M, Steele GA, van der Zant HSJ, Agrait N, Rubio-Bollinger G. Elastic Properties of Freely Suspended MoS2 Nanosheets. Adv Mater. 2012;24:772-+.
[43] Liu K, Yan QM, Chen M, Fan W, Sun YH, Suh J, et al. Elastic Properties of Chemical-Vapor-Deposited Monolayer MoS2, WS2, and Their Bilayer Heterostructures. Nano Lett. 2014;14:5097-103.
[44] Lin QY, Jing G, Zhou YB, Wang YF, Meng J, Bie YQ, et al. Stretch-Induced Stiffness Enhancement of Graphene Grown by Chemical Vapor Deposition. Acs Nano. 2013;7:1171-7.
[45] Zhang R, Koutsos V, Cheung R. Elastic properties of suspended multilayer WSe2. Appl Phys Lett. 2016;108: 042104.
[46] Wang JY, Li Y, Zhan ZY, Li T, Zhen L, Xu CY. Elastic properties of suspended black phosphorus nanosheets. Appl Phys Lett. 2016;108:013104.
[47] Annamalai M, Mathew S, Jamali M, Zhan D, Palaniapan M. Elastic and nonlinear response of nanomechanical graphene devices. Journal of Micromechanics and Microengineering. 2012;22:105024.
[48] Castellanos-Gomez A, Poot M, Steele GA, van der Zant HSJ, Agrait N, Rubio-Bollinger G. Mechanical properties of freely suspended semiconducting graphene-like layers based on MoS2. Nanoscale Research Letters. 2012;7:1-4.
[49] Castellanos-Gomez A, Poot M, Amor-Amoros A, Steele GA, van der Zant HSJ, Agrait N, et al. Mechanical properties of freely suspended atomically thin dielectric layers of mica. Nano Res. 2012;5:550-7.
[50] Poot M, van der Zant HSJ. Nanomechanical properties of few-layer graphene membranes. Appl Phys Lett. 2008;92:063111.
[51] Wong CL, Annamalai M, Wang ZQ, Palaniapan M. Characterization of nanomechanical graphene drum structures. Journal of Micromechanics and Microengineering. 2010;20:115029.
[52] Ruiz-Vargas CS, Zhuang HLL, Huang PY, van der Zande AM, Garg S, McEuen PL, et al. Softened Elastic Response and Unzipping in Chemical Vapor Deposition Graphene Membranes. Nano Lett. 2011;11:2259-63.
[53] Yang LS, Niu TX, Zhang H, Xu WJ, Zou MC, Xu L, et al. Self-assembly of suspended graphene wrinkles with high pre-tension and elastic property. 2d Materials. 2017;4.
[54] Zhang YP, Pan CX. Measurements of mechanical properties and number of layers of graphene from nano-indentation. Diamond and Related Materials. 2012;24:1-5.
[55] Niu T, Cao G, Xiong C. Fracture behavior of graphene mounted on stretchable substrate. Carbon. 2016;109:852-9.

[56] Niu T, Cao G, Xiong C. Indentation Behavior of the Stiffest Membrane Mounted on a Very Compliant Substrate: Graphene on PDMS. International Journal of Solids & Structures. 2018;132-133:1-8.
[57] Chen J, Guo XL, Tang Q, Zhuang CY, Liu JS, Wu SQ, et al. Nanomechanical properties of graphene on poly(ethylene terephthalate) substrate. Carbon. 2013;55:144-50.
[58] Cao G, Liu Y, Niu T. Indentation response of two-dimensional materials mounted on different substrates. Int J Mech Sci. 2018;137:96-104.
[59] Cao G, Niu T. Finite element modeling of the indentation behavior of two-dimensional materials. Acta Mech. 2018.
[60] Wei XD, Kysar JW. Experimental validation of multiscale modeling of indentation of suspended circular graphene membranes. Int J Solids Struct. 2012;49:3201-9.
[61] Rasool HI, Ophus C, Klug WS, Zettl A, Gimzewski JK. Measurement of the intrinsic strength of crystalline and polycrystalline graphene. Nature communications. 2013;4:2811.
[62] Komaragiri U, Begley MR. The mechanical response of freestanding circular elastic films under point and pressure loads. J Appl Mech-T Asme. 2005;72:203-12.
[63] Wan KT, Guo S, Dillard DA. A theoretical and numerical study of a thin clamped circular film under an external load in the presence of a tensile residual stress. Thin Solid Films. 2003;425:150-62.
[64] Timoshenko S, Woinowsky-Krieger S. Theory of plates and shells. New York: McGraw-Hill; 1959.
[65] Begley MR, Mackin TJ. Spherical indentation of freestanding circular thin films in the membrane regime. J Mech Phys Solids. 2004;52:2005-23.
[66] Steigmann DJ. Puncturing a thin elastic sheet. International Journal of Non-Linear Mechanics. 2005;40:255-70.
[67] Nadler B, Steigmann DJ. Modeling the indentation, penetration and cavitation of elastic membranes. J Mech Phys Solids. 2006;54:2005-29.
[68] Jin CR, Davoodabadi A, Li JL, Wang YL, Singler T. Spherical indentation of a freestanding circular membrane revisited: Analytical solutions and experiments. J Mech Phys Solids. 2017;100:85-102.
[69] Scott ON, Begley MR, Komaragiri U, Mackin TJ. Indentation of freestanding circular elastomer films using spherical indenters. Acta Materialia. 2004;52:4877-85.
[70] Bhatia NM, Nachbar W. Finite indentation of an elastic membrane by a spherical indenter. International Journal of Non-Linear Mechanics. 1968;3:307-24.
[71] Senturia SD. Microsystem Design. Boston: Kluwer Academic Publishers; 2000.
[72] Krenk S. Mechanics and Analysis of Beams, Columns, and Cables. Berlin: Springer; 2001.
[73] Lee J, Wang Z, He K, Shan J, Feng PXL. High Frequency MoS2 Nanomechanical Resonators. Acs Nano. 2013;7:6086-91.
[74] Bunch JS, Verbridge SS, Alden JS, van der Zande AM, Parpia JM, Craighead HG, et al. Impermeable atomic membranes from graphene sheets. Nano Lett. 2008;8:2458-62.
[75] Suk JW, Piner RD, An J, Ruoff RS. Mechanical Properties of Mono layer Graphene

Oxide. Acs Nano. 2010;4:6557-64.
[76] Koenig SP, Boddeti NG, Dunn ML, Bunch JS. Ultrastrong adhesion of graphene membranes. Nature Nanotechnology. 2011;6:543-6.
[77] Guo S, Wan KT, Dillard DA. A bending-to-stretching analysis of the blister test in the presence of tensile residual stress. Int J Solids Struct. 2005;42:2771-84.
[78] Jin C, Wang XD. A theoretical study of a thin-film delamination using shaft-loaded blister test: Constitutive relation without delamination. J Mech Phys Solids. 2008;56:2815-31.
[79] Jin CR. Large deflection of circular membrane under concentrated force. Appl Math Mech-Engl. 2008;29:889-96.
[80] Lopez-Polin G, Jaafar M, Guinea F, Roldan R, Gomez-Navarro C, Gomez-Herrero J. The influence of strain on the elastic constants of graphene. Carbon. 2017;124:42-8.
[81] Osterberg PM, Senturia SD. M-TEST: A test chip for MEMS material property measurement using electrostatically actuated test structures. J Microelectromech S. 1997;6:107-18.
[82] Tan XJ, Wu J, Zhang KW, Peng XY, Sun LZ, Zhong JX. Nanoindentation models and Young's modulus of monolayer graphene: A molecular dynamics study. Appl Phys Lett. 2013;102: 071908.
[83] Zhou LX, Wang YG, Cao GX. Boundary condition and pre-strain effects on the free standing indentation response of graphene monolayer. J Phys-Condens Mat. 2013;25:475303.
[84] Zhou L, Wang Y, Cao G. van der Waals effect on the nanoindentation response of free standing monolayer graphene. Carbon. 2013;57:357-62.
[85] Zhou LX, Xue JM, Wang YG, Cao GX. Molecular mechanics simulations of the deformation mechanism of graphene monolayer under free standing indentation. Carbon. 2013;63:117-24.
[86] Zhou L, Wang Y, Cao G. Estimating the elastic properties of few-layer graphene from the free-standing indentation response. J Phys-Condens Mat. 2013;25:475301.
[87] Jennings RM, Taylor JF, Farris RJ. Determination of Residual-Stress in Coatings by a Membrane Deflection Technique. J Adhesion. 1995;49:57-74.
[88] Wang LF, Zheng QS, Liu JZ, Jiang Q. Size dependence of the thin-shell model for carbon nanotubes. Phys Rev Lett. 2005;95.
[89] Huang Y, Wu J, Hwang KC. Thickness of graphene and single-wall carbon nanotubes. Phys Rev B. 2006;74: 245413.
[90] Gao EL, Xu ZP. Thin-Shell Thickness of Two-Dimensional Materials. J Appl Mech-T Asme. 2015;82: 121012.
[91] Shi JX, Natsuki T, Lei XW, Ni QQ. Equivalent Young's modulus and thickness of graphene sheets for the continuum mechanical models. Appl Phys Lett. 2014;104:223101.
[92] Cao GX, Chen X. Buckling of single-walled carbon nanotubes upon bending: Molecular dynamics simulations and finite element method. Phys Rev B. 2006;73:155435.

[93] Chen X, Cao GX. A structural mechanics study of single-walled carbon nanotubes generalized from atomistic simulation. Nanotechnology. 2006;17:1004-15.
[94] Wei YJ, Wang BL, Wu JT, Yang RG, Dunn ML. Bending Rigidity and Gaussian Bending Stiffness of Single-Layered Graphene. Nano Lett. 2013;13:26-30.
[95] Lu Q, Arroyo M, Huang R. Elastic bending modulus of monolayer graphene. J Phys D Appl Phys. 2009;42:102002.
[96] Lee JU, Yoon D, Cheong H. Estimation of Young's Modulus of Graphene by Raman Spectroscopy. Nano Lett. 2012;12:4444-8.
[97] Kitt AL, Qi ZN, Remi S, Park HS, Swan AK, Goldberg BB. How Graphene Slides: Measurement and Theory of Strain-Dependent Frictional Forces between Graphene and SiO2. Nano Lett. 2013;13:2605-10.
[98] Cao G, Ren Y, Ni B, Wang T, Zhuang Z, Gao H. J Mech Phys Solids. 2018;Submitted.
[99] Lu ZX, Dunn ML. van der Waals adhesion of graphene membranes. J Appl Phys. 2010;107:044301.
[100] Han J, Ryu S, Kim D-K, Woo W, Sohn D. Effect of interlayer sliding on the estimation of elastic modulus of multilayer graphene in nanoindentation simulation. Epl. 2016;114.
[101] Neek-Amal M, Peeters FM. Nanoindentation of a circular sheet of bilayer graphene. Phys Rev B. 2010;81:235421.
[102] Zhao JH, Jiang JW, Rabczuk T. Temperature-dependent mechanical properties of single-layer molybdenum disulphide: Molecular dynamics nanoindentation simulations. Appl Phys Lett. 2013;103:231913.
[103] Fair KM, Arnold MD, Ford MJ. Determination of the elastic properties of graphene by indentation and the validity of classical models of indentation. J Phys-Condens Mat. 2014;26.
[104] Lorenz T, Joswig JO, Seifert G. Stretching and breaking of monolayer MoS2-an atomistic simulation. 2d Materials. 2014;1.
[105] Capella B, Baschieri P, Frediani C, Miccoli P, Ascoli C. Force-distance curves by AFM - A powerful technique for studying surface interactions. Ieee Eng Med Biol. 1997;16:58-65.
[106] Suk JW, Na SR, Stromberg RJ, Stauffer D, Lee J, Ruoff RS, et al. Probing the adhesion interactions of graphene on silicon oxide by nanoindentation. Carbon. 2016;103:63-72.
[107] Xu DW, Liechti KM, Ravi-Chandar K. Mechanical Probing of Icelike Water Monolayers. Langmuir. 2009;25:12870-3.
[108] Costescu BI, Graeter F. Graphene mechanics: II. Atomic stress distribution during indentation until rupture. Phys Chem Chem Phys. 2014;16:12582-90.
[109] Gil AJ, Adhikari S, Scarpa F, Bonet J. The formation of wrinkles in single-layer graphene sheets under nanoindentation. J Phys-Condens Mat. 2010;22:145302.
[110] Han J, Ryu S, Sohn D. A feasibility study on the fracture strength measurement of polycrystalline graphene using nanoindentation with a cylindrical indenter. Carbon. 2016;107:310-8.
[111] Yazyev OV, Capaz RB, Louie SG. One-dimensional structural irregularities in graphene: chiral edges and grain boundaries. International Symposium: Nanoscience

and Quantum Physics 2011 (Nanophys'11). 2011;302.
[112] Song ZG, Artyukhov VI, Yakobson BI, Xu ZP. Pseudo Hall-Petch Strength Reduction in Polycrystalline Graphene. Nano Lett. 2013;13:1829-33.
[113] Liu YY, Yakobson BI. Cones, Pringles, and Grain Boundary Landscapes in Graphene Topology. Nano Lett. 2010;10:2178-83.
[114] Warner JH, Margine ER, Mukai M, Robertson AW, Giustino F, Kirkland AI. Dislocation-Driven Deformations in Graphene. Science. 2012;337:209-12.
[115] Kim P. GRAPHENE Across the border. Nature Materials. 2010;9:792-3.
[116] Yu QK, Jauregui LA, Wu W, Colby R, Tian JF, Su ZH, et al. Control and characterization of individual grains and grain boundaries in graphene grown by chemical vapour deposition. Nature Materials. 2011;10:443-9.
[117] Gibb AL, Alem N, Chen JH, Erickson KJ, Ciston J, Gautam A, et al. Atomic Resolution Imaging of Grain Boundary Defects in Monolayer Chemical Vapor Deposition-Grown Hexagonal Boron Nitride. Journal of the American Chemical Society. 2013;135:6758-61.
[118] Grantab R, Shenoy VB, Ruoff RS. Anomalous Strength Characteristics of Tilt Grain Boundaries in Graphene. Science. 2010;330:946-8.
[119] Song ZG, Artyukhov VI, Wu J, Yakobson BI, Xu ZP. Defect-Detriment to Graphene Strength Is Concealed by Local Probe: The Topological and Geometrical Effects. Acs Nano. 2015;9:401-8.
[120] Ren Y, Cao G. Effect of geometrical defects on the tensile properties of graphene. Carbon. 2016;103:125-33.
[121] Liu TH, Pao CW, Chang CC. Effects of dislocation densities and distributions on graphene grain boundary failure strengths from atomistic simulations. Carbon. 2012;50:3465-72.
[122] Wu JT, Wei YJ. Grain misorientation and grain-boundary rotation dependent mechanical properties in polycrystalline graphene. J Mech Phys Solids. 2013;61:1421-32.
[123] Tanemura M, Ogawa T, Ogita N. A New Algorithm for 3-Dimensional Voronoi Tessellation. J Comput Phys. 1983;51:191-207.
[124] Finney JL. Procedure for the Construction of Voronoi Polyhedra. J Comput Phys. 1979;32:137-43.
[125] Sha ZD, Wan Q, Pei QX, Quek SS, Liu ZS, Zhang YW, et al. On the failure load and mechanism of polycrystalline graphene by nanoindentation. Sci Rep-Uk. 2014;4:7437.
[126] Ho DH, Sun Q, Kim SY, Han JT, Kim DH, Cho JH. Stretchable and Multimodal All Graphene Electronic Skin. Adv Mater. 2016;28:2601-+.
[127] Papageorgiou DG, Kinloch IA, Young RJ. Graphene/elastomer nanocomposites. Carbon. 2015;95:460-84.
[128] Hou CY, Wang HZ, Zhang QH, Li YG, Zhu MF. Highly Conductive, Flexible, and Compressible All-Graphene Passive Electronic Skin for Sensing Human Touch. Adv Mater. 2014;26:5018-24.
[129] Chen JH, Jang C, Xiao SD, Ishigami M, Fuhrer MS. Intrinsic and extrinsic performance limits of graphene devices on SiO2. Nature Nanotechnology. 2008;3:206-9.
[130] Gong L, Kinloch IA, Young RJ, Riaz I, Jalil R, Novoselov KS. Interfacial Stress

Transfer in a Graphene Monolayer Nanocomposite. Adv Mater. 2010;22:2694-+.
[131] Young RJ, Kinloch IA, Gong L, Novoselov KS. The mechanics of graphene nanocomposites: A review. Composites Science and Technology. 2012;72:1459-76.
[132] Lou Z, Chen S, Wang LL, Jiang K, Shen GZ. An ultra-sensitive and rapid response speed graphene pressure sensors for electronic skin and health monitoring. Nano Energy. 2016;23:7-14.
[133] Gao JF, Zhang G, Zhang YW. The Critical Role of Substrate in Stabilizing Phosphorene Nanoflake: A Theoretical Exploration. Journal of the American Chemical Society. 2016;138:4763-71.
[134] Chen SH, Liu L, Wang TC. Investigation of the mechanical properties of thin films by nanoindentation, considering the effects of thickness and different coating-substrate combinations. Surf Coat Tech. 2005;191:25-32.
[135] Johnson KL. Contact mechanics. Cambridge: Cambridge University Press; 1985.
[136] Oliver WC, Pharr GM. Measurement of hardness and elastic modulus by instrumented indentation: Advances in understanding and refinements to methodology. J Mater Res. 2004;19:3-20.
[137] Cao G, Sui J, Sun S. Evaluating the nucleus effect on the dynamic indentation behavior of cells. Biomechanics and Modeling in Mechanobiology. 2013;12:55-66.
[138] Cao G, Chandra N. Evaluation of biological cell properties using dynamic indentation measurement. Physical Review E. 2010;81:021924.
[139] Vanimisetti SK, Narasimhan R. A numerical analysis of spherical indentation response of thin hard films on soft substrates. Int J Solids Struct. 2006;43:6180-93.
[140] Pharr GM, Oliver WC. Measurement of Thin-Film Mechanical-Properties Using Nanoindentation. Mrs Bull. 1992;17:28-33.
[141] King RB. Elastic Analysis of Some Punch Problems for a Layered Medium. Int J Solids Struct. 1987;23:1657-64.
[142] Pharr GM. Measurement of mechanical properties by ultra-low load indentation. Materials Science and Engineering a-Structural Materials Properties Microstructure and Processing. 1998;253:151-9.
[143] Oliver WC, Pharr GM. An Improved Technique for Determining Hardness and Elastic-Modulus Using Load and Displacement Sensing Indentation Experiments. J Mater Res. 1992;7:1564-83.
[144] Zhao M, Chen X, Xiang Y, Vlassak JJ, Lee D, Ogasawara N, et al. Measuring elastoplastic properties of thin films on an elastic substrate using sharp indentation. Acta Materialia. 2007;55:6260-74.
[145] Cao GX, Chen X, Xu ZH, Li XD. Measuring mechanical properties of micro- and nano-fibers embedded in an elastic substrate: Theoretical framework and experiment. Compos Part B-Eng. 2010;41:33-41.
[146] Niu T, Cao G. Finite size effect does not depend on the loading history in soft matter indentation. J Phys D Appl Phys. 2014;47:385303.
[147] Niu T, Cao G. Power-law rheology characterization of biological cell properties under AFM indentation measurement. Rsc Advances. 2014;4:29291-9.

[148] Zhang MG, Cao YP, Li GY, Feng XQ. Spherical indentation method for determining the constitutive parameters of hyperelastic soft materials. Biomechanics and Modeling in Mechanobiology. 2014;13:1-11.
[149] Lim YY, Chaudhri MM. Indentation of elastic solids with a rigid Vickers pyramidal indenter. Mech Mater. 2006;38:1213-28.
[150] Deuschle JK, Buerki G, Deuschle HM, Enders S, Michler J, Arzt E. In situ indentation testing of elastomers. Acta Materialia. 2008;56:4390-401.
[151] Jiang T, Huang R, Zhu Y. Interfacial Sliding and Buckling of Monolayer Graphene on a Stretchable Substrate. Advanced Functional Materials. 2014;24:396-402.
[152] Young RJ, Gong L, Kinloch IA, Riaz I, Jalil R, Novoselov KS. Strain Mapping in a Graphene Monolayer Nanocomposite. Acs Nano. 2011;5:3079-84.
[153] Zhou L, Wang Y, Cao G. Boundary condition and pre-strain effects on the free standing indentation response of graphene monolayer. J Phys-Condens Mat. 2013;25.
[154] Cerda E, Ravi-Chandar K, Mahadevan L. Thin films - Wrinkling of an elastic sheet under tension. Nature. 2002;419:579-80.
[155] Cerda E, Mahadevan L. Geometry and physics of wrinkling. Phys Rev Lett. 2003;90.
[156] Neek-Amal M, Peeters FM. Linear reduction of stiffness and vibration frequencies in defected circular monolayer graphene. Phys Rev B. 2010;81:235437.

Table I. Mechanical properties of 2D materials obtained from FSI

2D materials	Approach	E (TPa)	σ_f (GPa)	Reference
Bi-layer Graphene	MD	0.8		[101]
Monolayer graphene	MD	0.501-1		[16, 82, 156]
Monolayer graphene	FEM		108.5	[60]
Monolayer graphene	MD		105	[19]
Monolayer graphene	Experiment	1.0±0.1	130±10	[33]
Graphene (n<5)	Experiment	0.5		[34]
Monolayer graphene	Experiment	1.12		[47]
Polycrystalline graphene	Experiment	0.967-1.01	98.5-118	[40]
Monolayer MoS_2	MD	0.149-0.159	13-58	[102]
Monolayer MoS_2	Experiment	0.27±0.1	23	[41]
Monolayer MoS_2	Experiment	0.264±0.018		[43]
MoS_2 (n=5-25)	Experiment	0.21–0.37		[42]
Multiple-layer BP	Experiment	0.0586±0.0117(zz) 0.0272±0.0041(ac)	4.79±1.43(zz) 2.31±0.71(ac)	[27]
Multiple-layer BP	Experiment	0.276±0.0324	25	[46]
Multiple-layer WSe_2	Experiment	0.1673±0.0067	12.4	[45]

Table II. Geometrical parameters selected in FSI

2D materials	Sample size (μm)	t (nm)	δ_t (nm)	s (nm)	R (nm)	Ref
Graphene (n = 1)	a = 0.5, 0.75	0.335	20-100	2-10	16.5, 27.5	[33]
Graphene (n > 1)	a = 1	2-8	12			[34]
Graphene (n < 5)	a = 1.9	0.335-1.675	50-130		8±2	[47]
Graphene ($n \leq 2$)	L = 1.2, W = 2	0.34-0.68	10			[36]
Graphene ($n \leq 5$)	L = 5, W = 3	1-5	90			[39]
GO (n = 1)	L = 0.8-1, W = 1-2	0.335	10			[38]
MoS_2 (n = 1)	a = 0.55±0.01	0.65	40	5	12±2	[41]
MoS_2 (n = 1)	a = 0.55	0.65	70		10	[43]
MoS_2 (n = 5-25)	a = 0.55	3-15	5-15			[42]
BP (n > 1)	L = 0.8-1.92 W = 0.48-1.47	14.8-28	5		28	[27]
BP (n > 1)	a = 1-1.5	14.3-34	70		20	[46]
WSe_2 (n > 1)	a = 0.75, 1.3	3.5-9.8	80-130		81	[45]
Mica (n = 2-14)	a = 0.5-0.55	2-8	5		15-20	[49]

Figure Captions:

Figure 1. Images of selected 2D materials measured with FSI. (a) AFM image of a MoS_2 monolayer [43]. (b) AFM image of a SeW_2 [45]. (c) (d) Scanning electron microscopy (SEM) images of a graphene [33, 34]. (e)(f) AFM and SEM images of a Layered BP [27, 46].

Figure 2. Doubly-clamped beam structure of a selected 2D material [27]. (a) SEM image of a beam structure of a Layered BP. (b)(c) Schematics of the beam structure before and after applying the indentation load.

Figure 3. FSI responses of selected 2D materials over a trench in the substrate. (a) The linear P-δ_i relationship [34]. (b) The relationship between the slope k of the P-δ_i curve and the ratio of t/L [34]. (c) The P-δ_i relationship of a doubly-clamped beam structure of a selected 2D material with a large indentation displacement [39] .

Figure 4. FSI responses of a clamped circular structure of a selected 2D material with a small indentation displacement [42]. (a) Schematics of a clamped circular structure. (b) The linear P-δ_i relationship. (c) The relationship between the slope k of the P-δ_i curve and the ratio of t^3/a^2.

Figure 5. FSI responses of a clamped circular structure of a selected 2D material with a large indentation displacement [33]. (a) The indentation P-δ_i relationship and the fitting function (Eq. (9)). (b) The fracture behavior measured via FSI testing, and the fracture load is marked as × in the figure.

Figure 6. FSI testing for the elastic modulus of clay tactoids [37]. (a) FSI testing setup. (b) Determination of the elastic modulus of clay tactoids using Eq. (11).

Figure 7. (a) AFM image of a monolayer graphene mounted on a cylindrical well in SiO_2 substrate. (b) Line cut through the center of the graphene membrane in (a). (c) Schematics of a FS graphene cover on a substrate well before and after applying an indentation load (Z_0 is the adhesive length to the substrate sidewall) [74].

Figure 8. AFM image of a deformed graphene mounted on a cylindrical well (top), the height profile of the topology of the deformed graphene (middle), and the relationship between the G-band frequency and the applied pressure difference across the graphene (bottom) [97]. (a) a

multiple-layer graphene (n = 3) sealed microchamber (a = 5 μm); (b) a monolayer graphene sealed microchamber (a = 3 μm). There is a portion of FS graphene adhered on the sidewall of the substrate due to a vdW interaction.

Figure 9. The G-band frequency ω_g of the graphene sealed a cylindrical hole varying with the radial distance (ω_g decreases with the increase of the in-plane tension of graphene) [97].

Figure 10. The geometry of the FS region of CVD grown graphene before and after loading (the top figures show the AFM images; the bottom figures show the height profile of the cutting line) [44]. (a) Initial structure. (b) Deformed structure by a small indentation load.

Figure 11. MD simulation model of a FS graphene with an adhesive boundary condition under a concentrated load (including a horizontal portion and a vertical portion adhered with the substrate sidewall of SiO_2) [83]. (a) Initial structure. (b) The adhered portion is peeled off the substrate sidewall by an indentation load.

Figure 12. (a) Schematic of the FEM model of FSI testing of a 2D material with an adhesive boundary. (b) The cohesive zone model of the vdW interaction between the FS 2D material and the substrate sidewall [98].

Figure 13. FEM results of the P-δ_t relationship obtained from the FSI of a 2D material with an adhesive boundary condition. (a) With the different adhesive strength. (b) With the different adhesive length [98].

Figure 14. Schematic illustrations of the adhesive boundary condition and pre-tension of a 2D material in FSI [98]. (a) Initial structure of a FS 2D material transferred on a substrate with a cylindrical hole. (b) A FS 2D material with an adhesive boundary condition over the portion of the FS material larger than the substrate hole. (c) An extra adhered portion s_1 created by vdW adhesion from the substrate sidewall, and meanwhile a pretension is induced in the FS 2D material. (d) Pre-tension in the FS 2D material induced by vdW adhesion. ε_{rr} and $\varepsilon_{\theta\theta}$ denotes tensile prestrains along radial and circumferential directions, respectively. $\varepsilon_{rr} = \varepsilon_{\theta\theta} = \varepsilon_0 = s_1/a$ for $r \le a$; $\varepsilon_{rr} = \varepsilon_0 = s_1/a$ and $\varepsilon_{\theta\theta} = 0$ for $a < r < a + s_1$.

Figure 15. (a) The measured P-δ_t curve in FSI testing of CVD grown graphene. The inset figure shows the zoom-in structure of the initial stage of the curve enclosed by the dashed line,

among which the red color points show the initial linear P-δ_t relationship. (b) The elastic moduli of graphene determined from the measured P-δ_t curve vary with the different initial contact position. When the indentation model based on Eq. (8) is used, the determined E increases with the increase of the initial contact position (displayed as black squared symbols); when Eq. (22) is used, the determined E is not sensitive to the selection of the initial contact position (displayed as red circular symbols), and the average value E = 540GPa [44].

Figure 16. MD simulation models of graphene in FSI testing. (a) With a spherical tip. (b) With a cylindrical tip [84, 85].

Figure 17. The effect of the vdW interaction between the indenter-tip and graphene on the topology of the graphene at the initial contact position [84]. (a) Without the vdW interaction. (b) With the vdW interaction (ε_0 = 0). (c) With the vdW interaction and ε_0 = -0.01 (representing the sample with a larger size than the sealed microchamber). (d) With the vdW interaction and ε_0 = 0.01 (the graphene is prestretched.)

Figure 18. MD simulation results of the normalized strain energy U_{tot}/A of monolayer graphene in FSI testing and its components U_g/A (the normalized strain energy of graphene) and U_{vdw}/A (the normalized vdW interaction energy between indenter tip and graphene), varying with in-plane strain, where A is the in-plane area of sample. The right side is for the ratio of U_{vdw}/U_g [84].

Figure 19. (a) Relationship between indentation displacements (displayed as δ_t/L and δ/L, respectively) and in-plane strain of the monolayer graphene in FSI testing calculated through MM simulations. δ_t and δ are the displacements of indenter tip and graphene, respectively. The solid lines are the fitting curves of Eq. (24). (b) The divergence between δ_t and δ varying with the ratio of L/R, displayed as the fitting parameters k_1 and k_2 [85].

Figure 20. The elastic moduli and pre-strains determined from the simulated FSI responses of the graphene under a cylindrical tip based on the P-δ_t relationship and the P-δ relationship, respectively [83].

Figure 21. FEM results of the P-δ_t relationships of graphene based on the linear/nonlinear elastic models [33]. (a) The P-δ_t relationship with a small δ_t, and for reference purposes, the

theoretical value determined from Eq. (9) is also displayed in the figure. (b) The P-δ_t relationship with a large value of δ_t, and for reference purposes, the theoretical value determined from Eq. (22) is also displayed in the figure.

Figure 22. The σ_{int} value determined from Eq. (2) varies with the fitting range of the indentation strain. The values of E and D used to calculate σ_{int} are determined through fitting the calculated σ-ε relationship via DFT with Eq. (1) [24].

Figure 23. The indentation stress in graphene calculated by MD simulations [19]. (a) In-plane stress components σ_{xx}, σ_{yy}. (b) The relationship between the indentation stress $(\sigma_{xx} + \sigma_{yy})/2$ and the indentation load P.

Figure 24. Various fracture strengths of the bi-crystalline graphene determined from FSI testing [19]. (a) Indenting from the position moving along grain boundary. (b) Indenting from the position moving perpendicular to grain boundary. (c) Indenting the grain with different tilt angle θ.

Figure 25. The simulated fracture behavior of a bi-crystalline graphene through FSI [19]. (a) The P-δ_t relationship; (b) the crack evolution with the indentation displacement.

Figure 26. The effect of the tip-graphene vdW interaction on the topology of the graphene with the different number of layers at the initial contact position [86]. (a) n = 1; (b) n = 2; and (c) n = 4.

Figure 27. (a) Relationship between indentation displacement and in-plane strain of a few layer graphene in FSI calculated through MD simulations. (a) The relationship between δ_t/L and ε; (b) the relationship between δ/L and ε. δ_t and δ are the displacements of indenter tip and graphene, respectively [86]. The dashed line is the fitting curve of Equation (16).

Figure 28. MD simulation results of the elastic moduli of the graphene with the different number of layers, normalized by the corresponding value determined from in-plane stretching (E_0^m), or by the elastic moduli of monolayer graphene (E_1, E_2). For reference purposes, the value of E_0^m normalized by the product of nE_0 is also displayed in the figure [86].

Figure 29. The indentation response of a graphene mounted on a PDMS substrate [56]. (a) Schematic of the indentation test. (b) The measured P-δ_t relationship of pure PDMS substrate.

(c) The measured P-δ_t relationship of graphene/PDMS. (d) The histogram of elastic modulus determined from the indentation response of graphene/PDMS.

Figure 30. The fracture behavior of graphene measured through the indentation response of graphene/PDMS [55]. (a) The P-δ_t relationships. For reference purposes, the indentation response of pure PDMS is displayed as the dashed line in the figure. (b) The relationship between the indentation stress and indentation load calculated by FEM. The fracture load is marked as a star.

Figure 31. The overall indentation modulus (E_r) of a 2D material mounted on various substrate varying with the normalized indentation displacement δ_t/R, where R is tip radius [58]. In the figure, E_r is normalized by the indentation modulus of substrate $E_s' = E_s/(1-\nu_s)$, and λ is the elastic modulus ratio of the 2D material to the substrate $\lambda = E_f/E_s$. (a) Using the Hertz solution, $\delta_t/R \leq 0.5$. (b) Using the true contact radius calculated from FEM, $\delta_t/R \leq 0.5$. (c) Using the Hertz solution, $\delta_t/R > 0.5$. (d) Using the true contact radius calculated from FEM, $\delta_t/R > 0.5$.

Figure 32. (a) The strain energy ratio of the 2D material to the overall 2D material/substrate $U_f/(U_f+U_s)$ varying with the normalized indentation depth δ_t/R [55]. (b) The fitting coefficients A and B determined from the P-δ_t relationships calculated by FEM using Eq. (39). The dashed lines are fitting functions.

Figure 33. FEM results of the radial distribution of the in-plane strains of the graphene in graphene/PDMS just before the failure of graphene [55]. (a) Radial strain. (b) Circumferential strain. The inset figures show the strains of the sample close to the indenter tip. In FEM, the PDMS substrate is modeled using the different material models including the linear elastic, neo-Hookean and Standard Linear Solid models. For reference purposes, the FSI result of graphene is also shown in the figure.

Figure 34. A new developed fabrication method of FS 2D materials on the basis of substrate self-cracking, in which a clamped, pre-stretched, FS film of GO is fabricated [53]. (a)(b) SEM images on a typical area consisting of a FS GO film (55 nm in thickness) covering cracked TiO_2. (c) Enlarged view of suspended GO films between islands. (d) The measured P-δ_t

relationships of suspended GO films between islands.

Figure 35. Morphology of FS membranes over a microchamber with an applied pressure difference across them [80]. (a)(b)(c) AFM images of a FS graphene over a circular chamber of 1.5 mm diameter subjected to various ΔP. (d)(e)(f) Schematic profiles of the pressurized membrane. (g) Height profiles along the midline in the AFM images shown in Figs. (a)(b)(c).

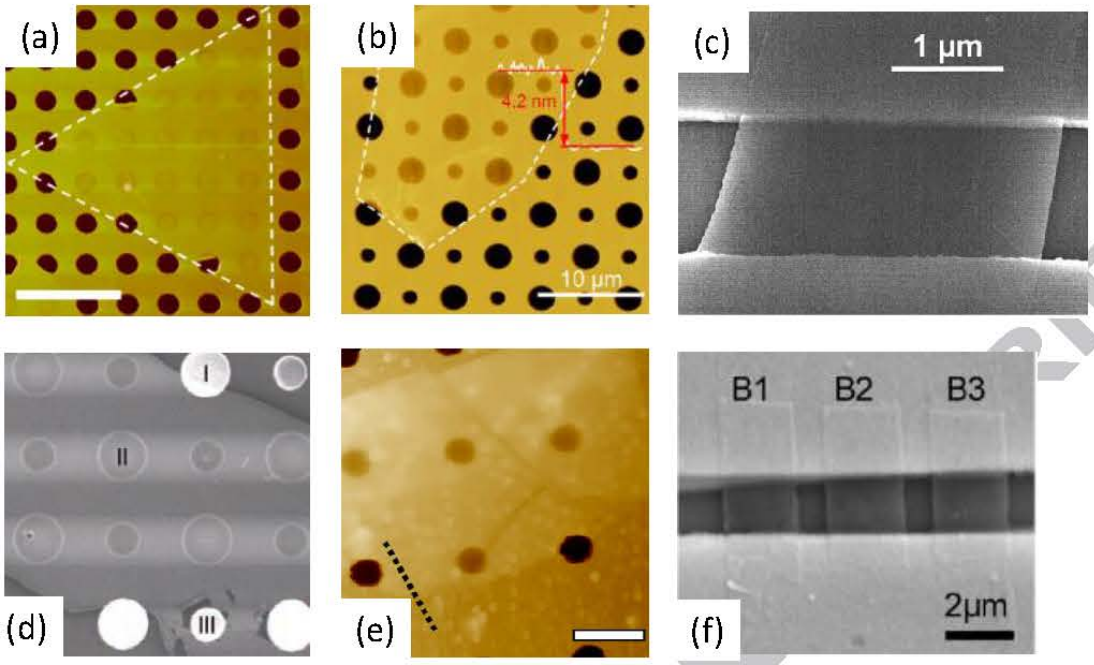

Figure1.

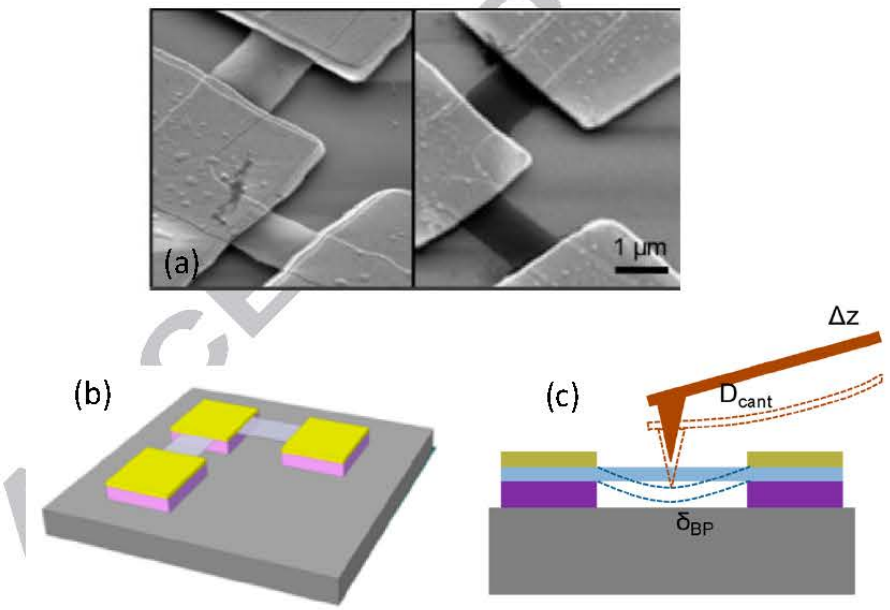

Figure 2.

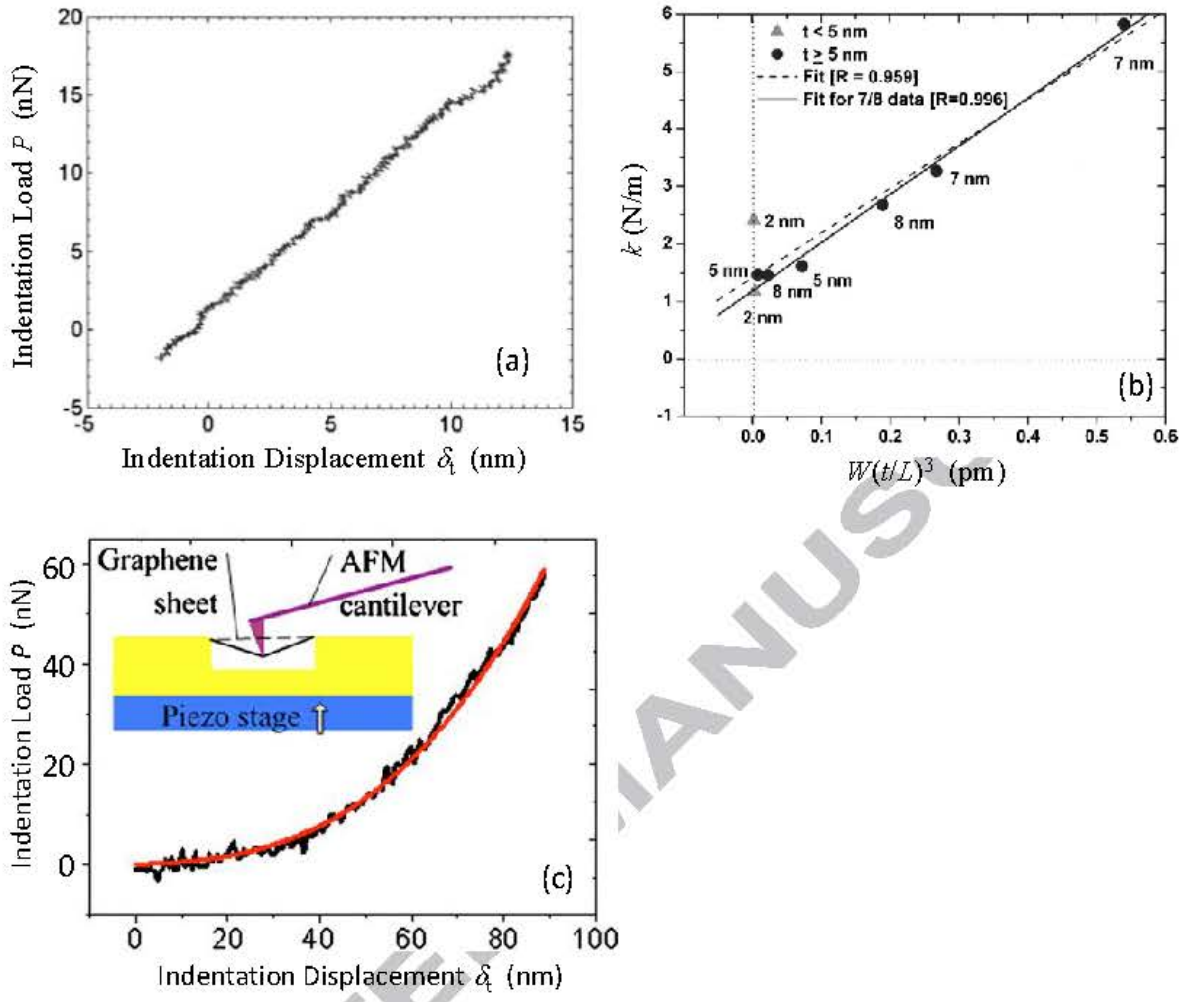

Figure 3.

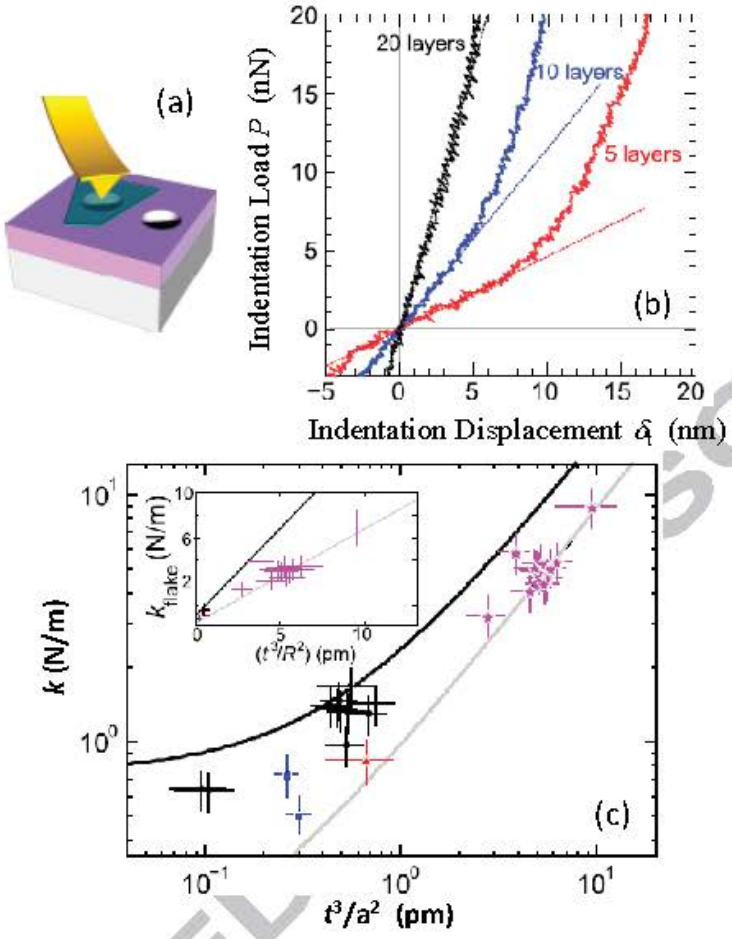

Figure 4.

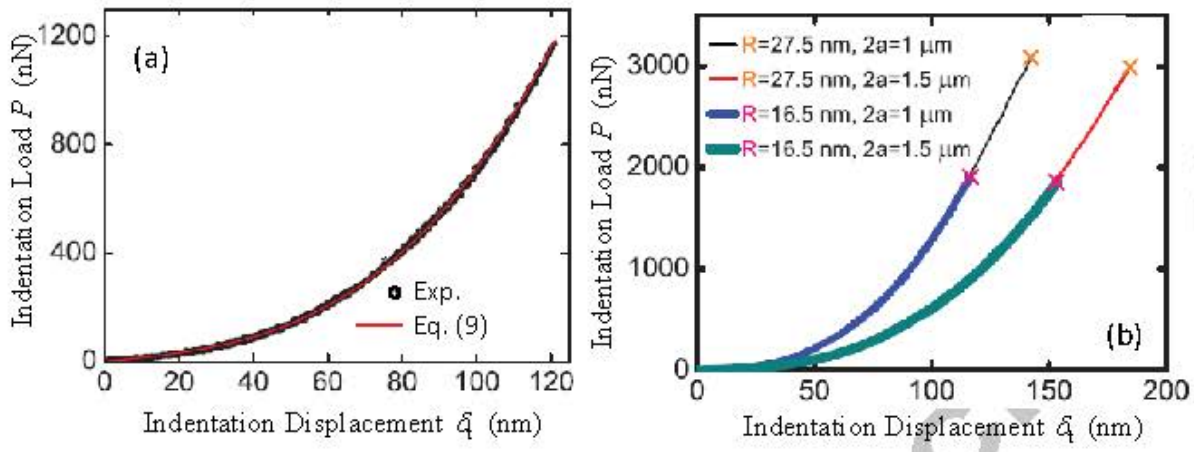

Figure 5.

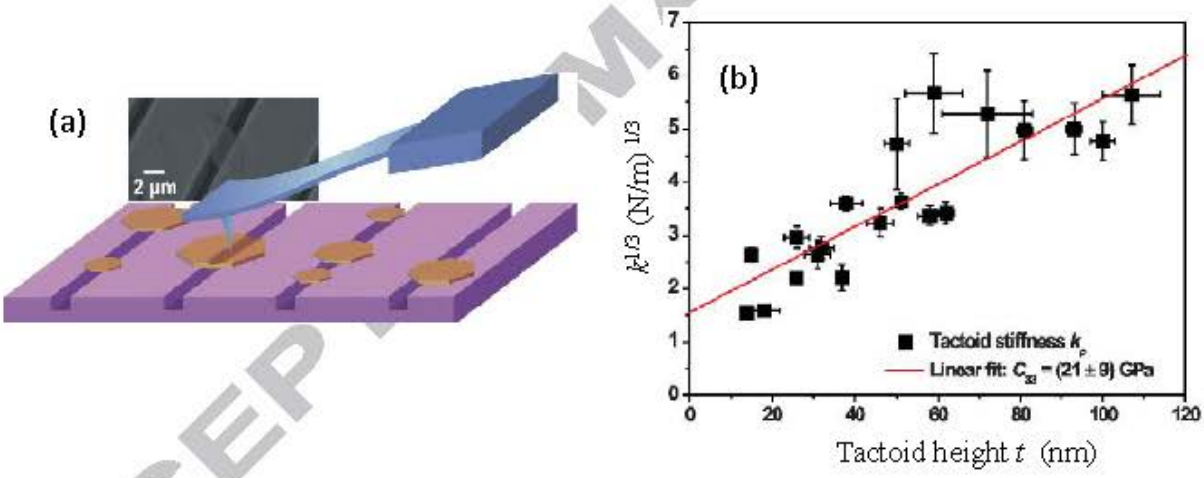

Figure 6.

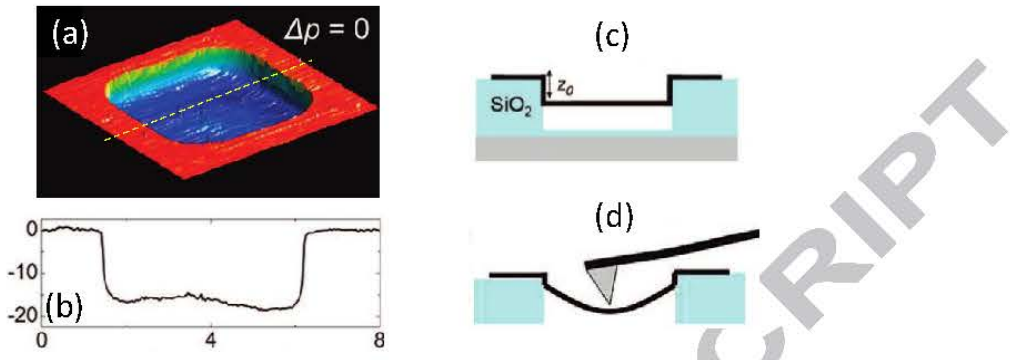

Figure 7.

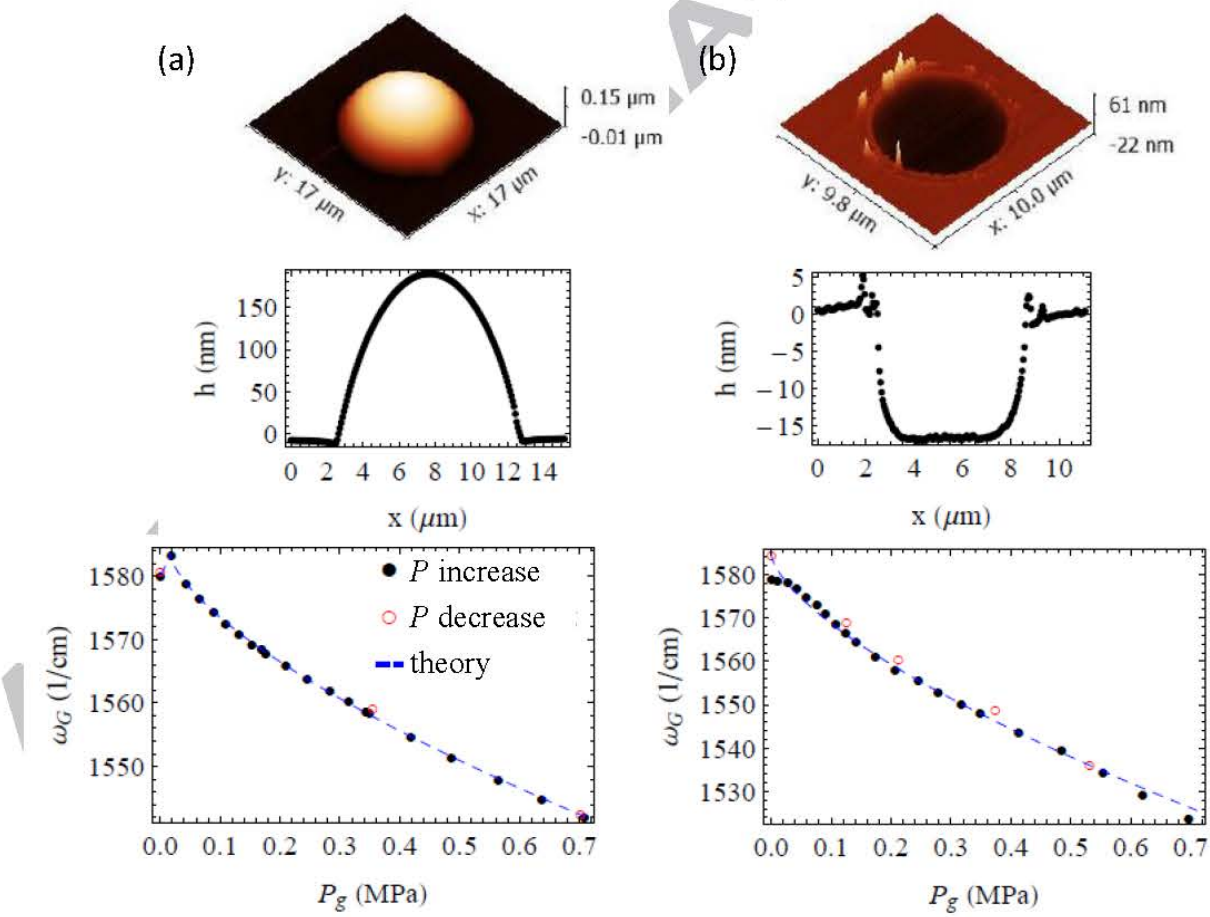

Figure 8.

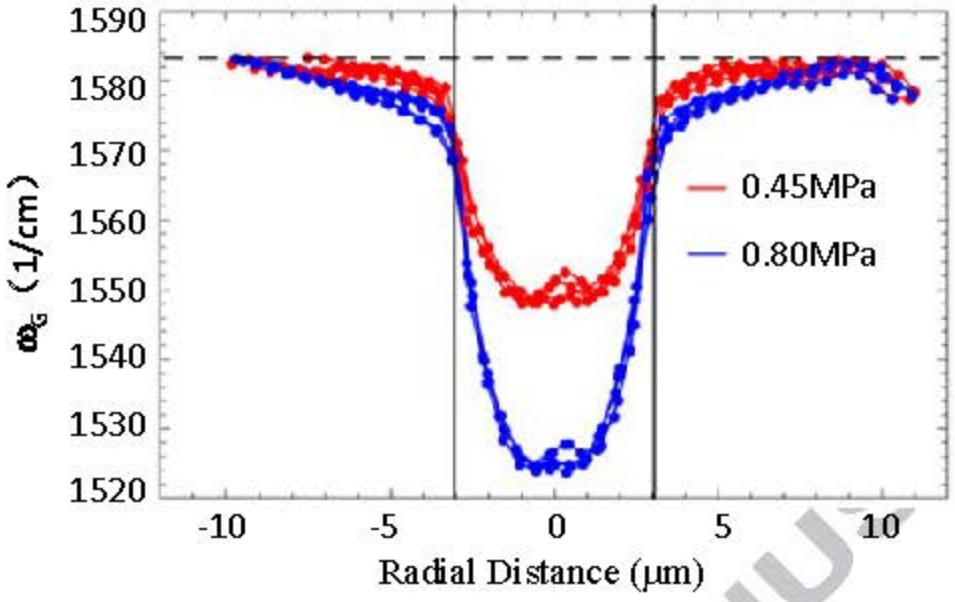

Figure 9.

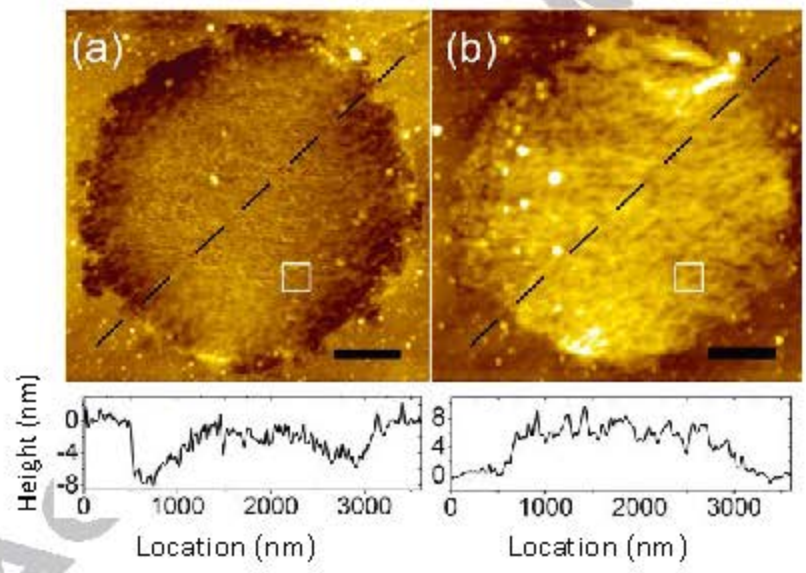

Figure 10.

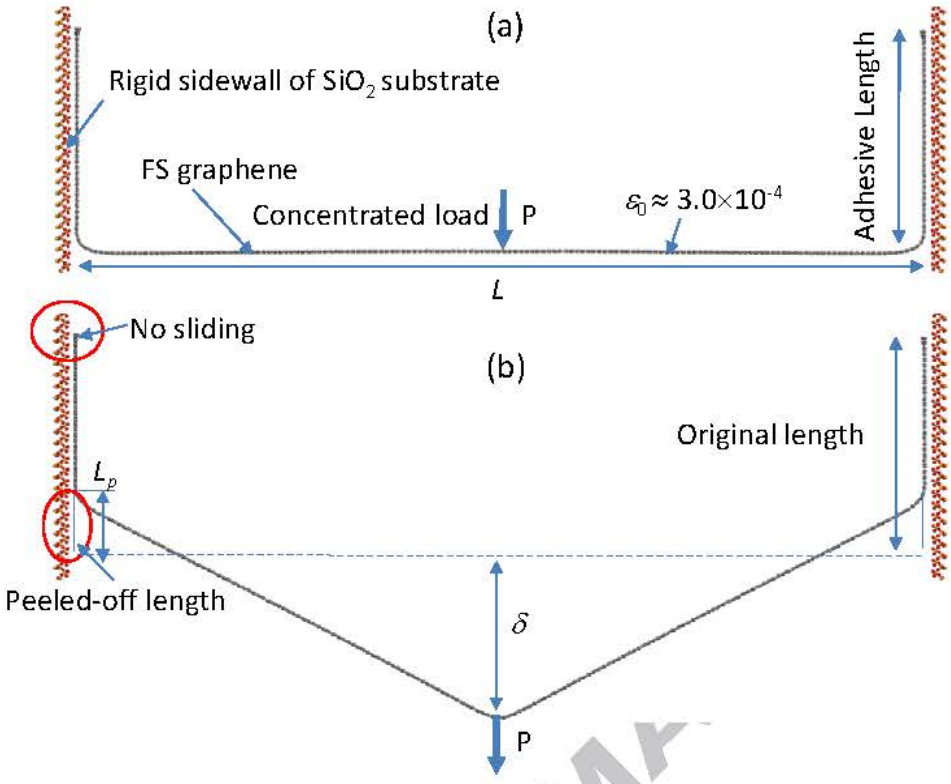

Figure 11.

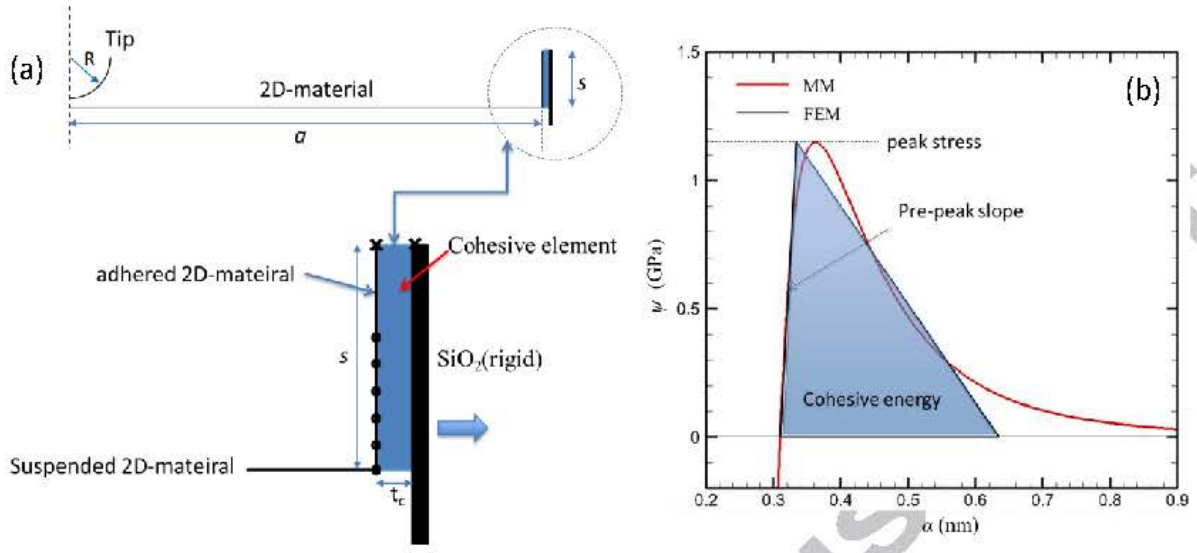

Figure 12.

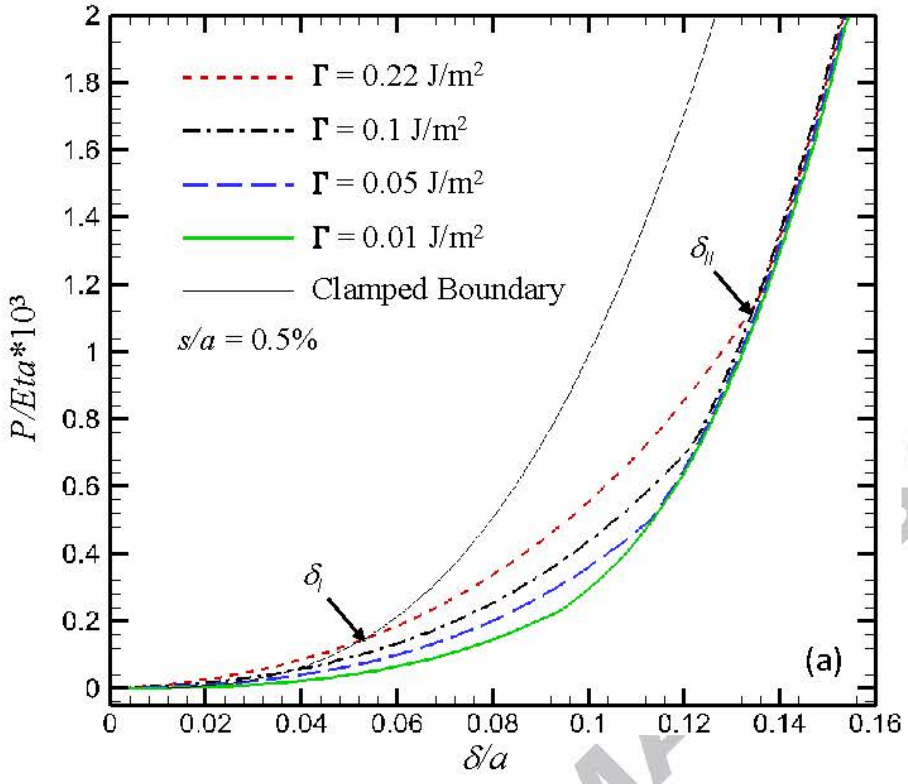

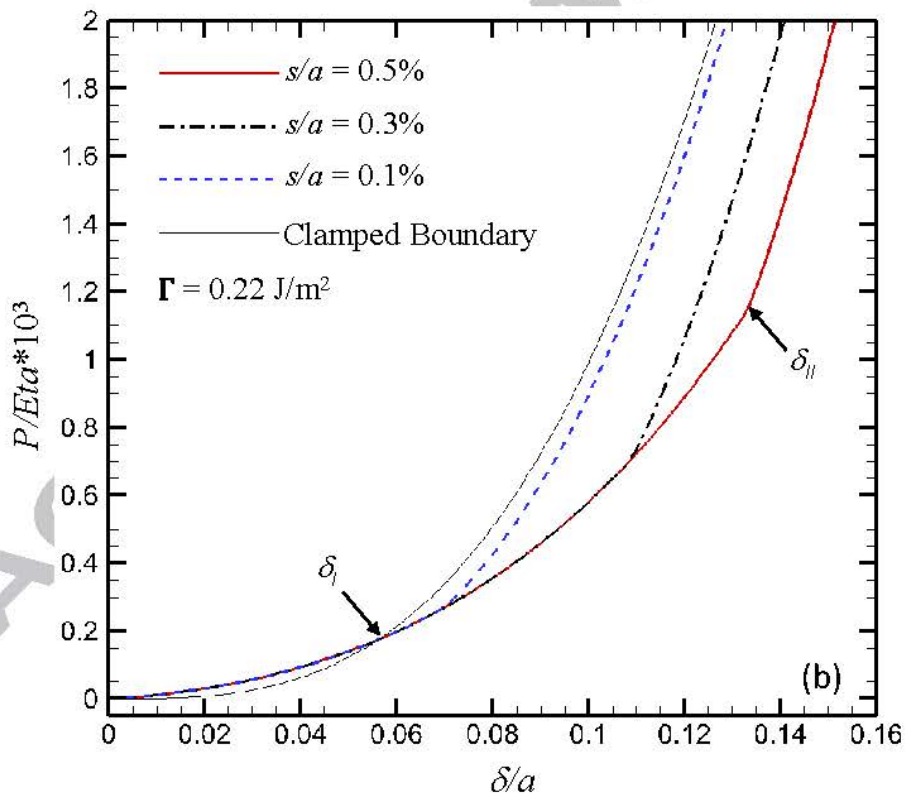

Figure 13.

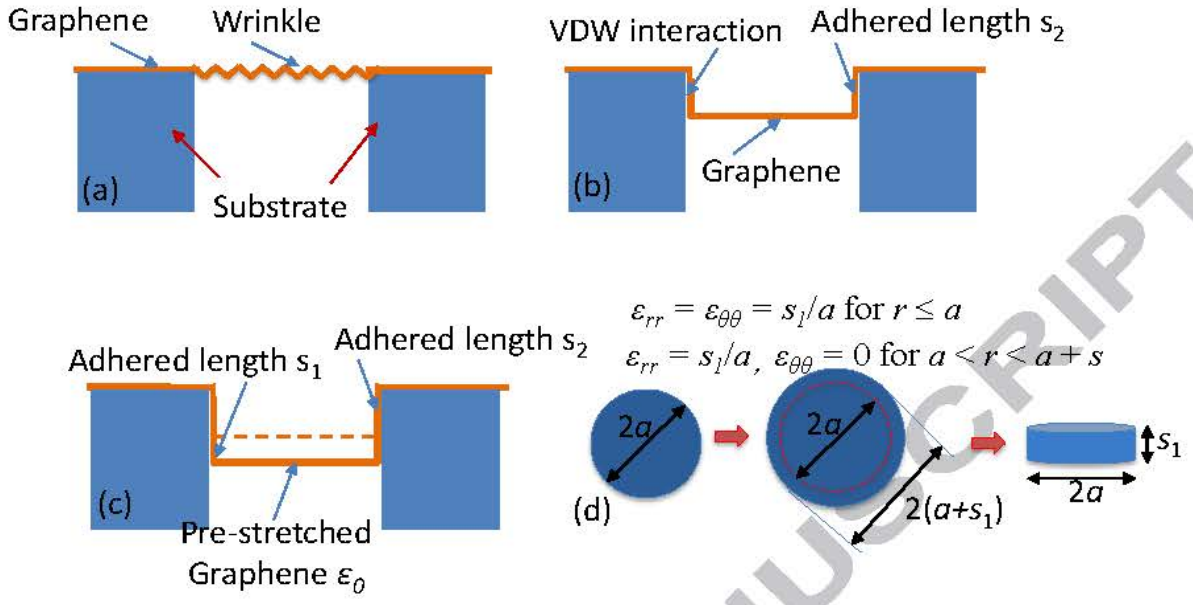

Figure 14

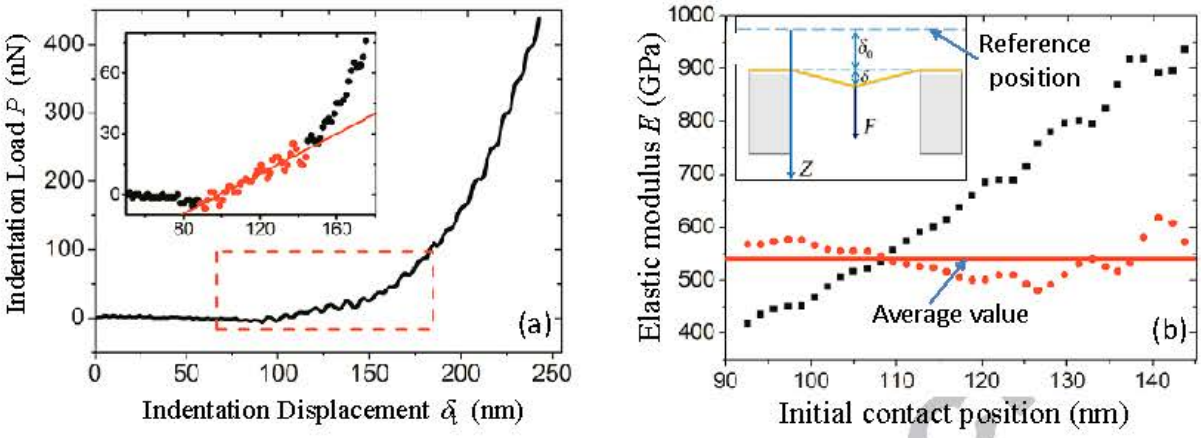

Figure 15.

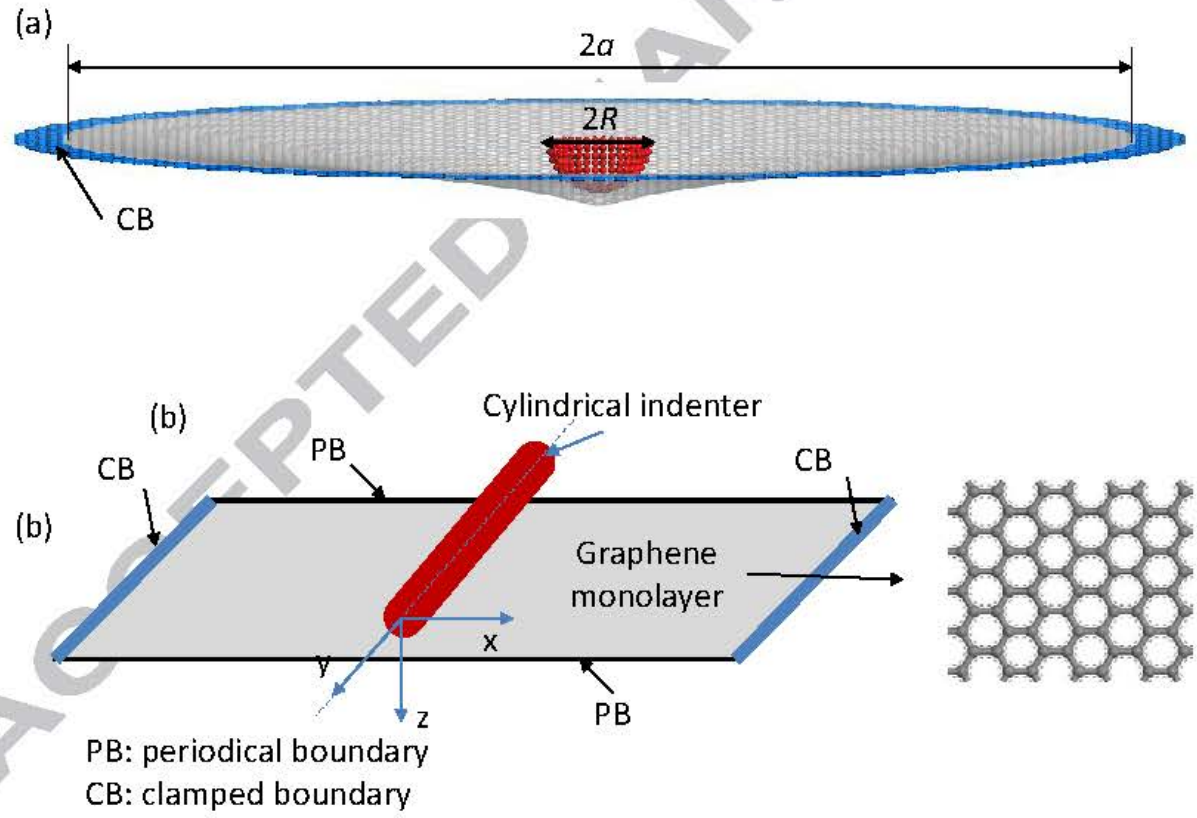

Figure 16

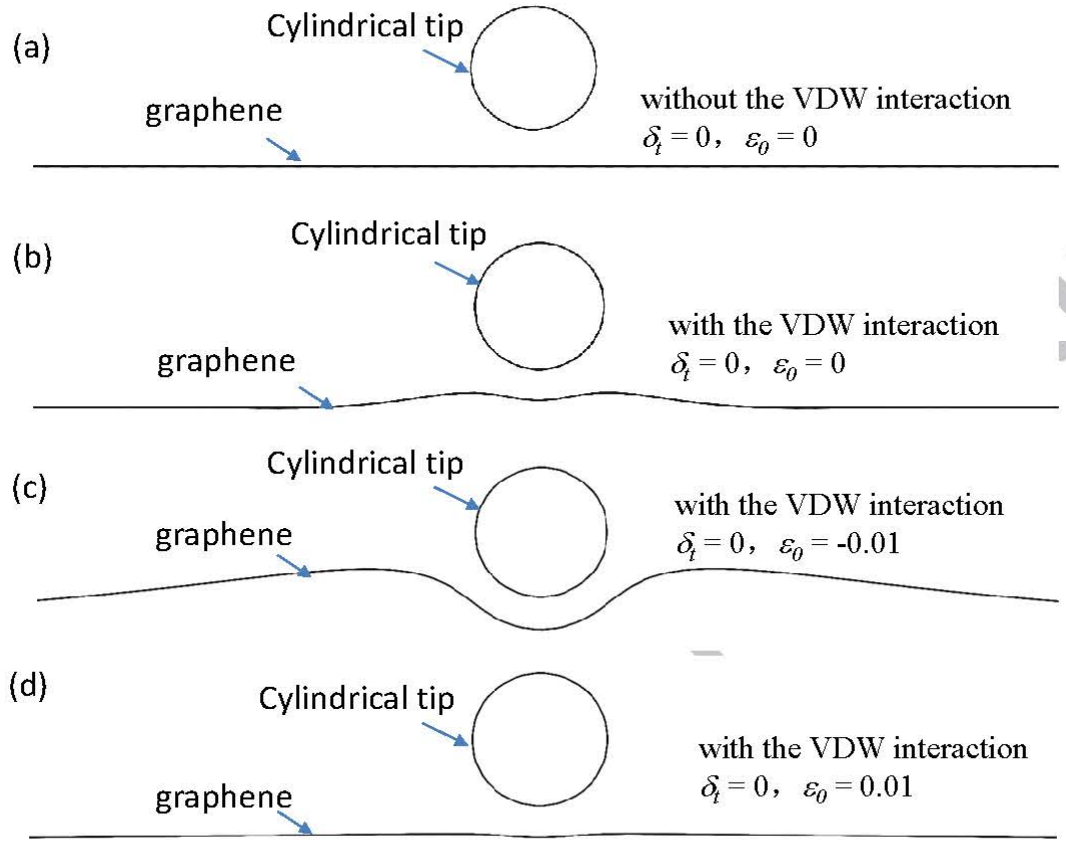

Figure 17.

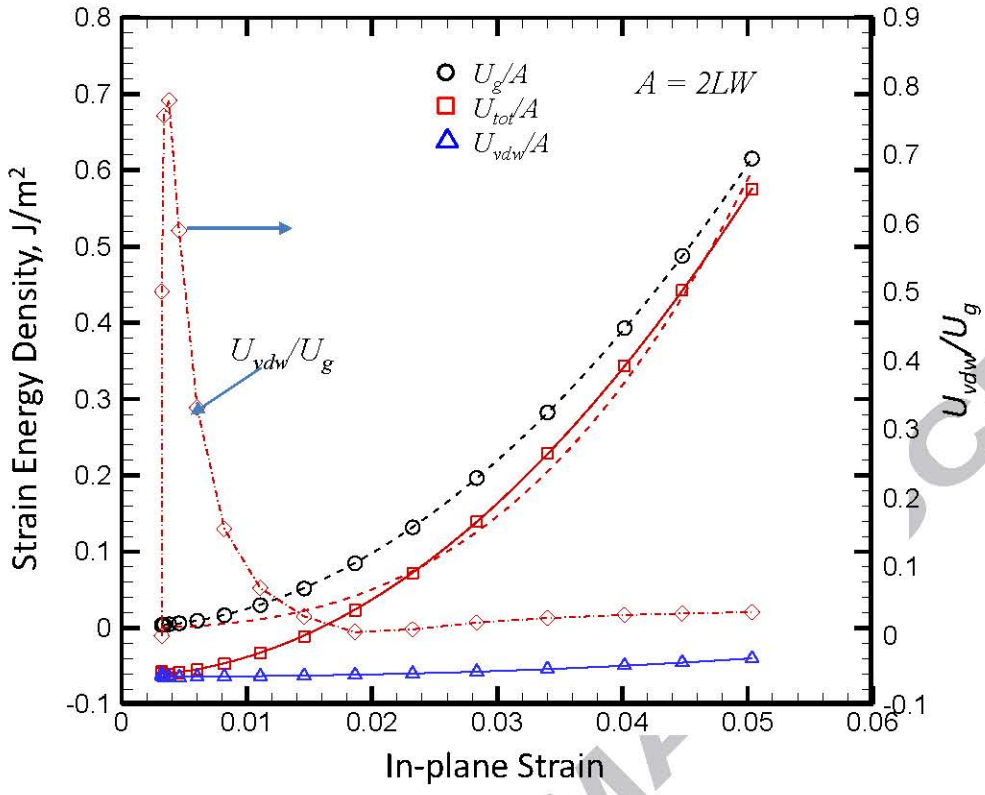

Figure 18.

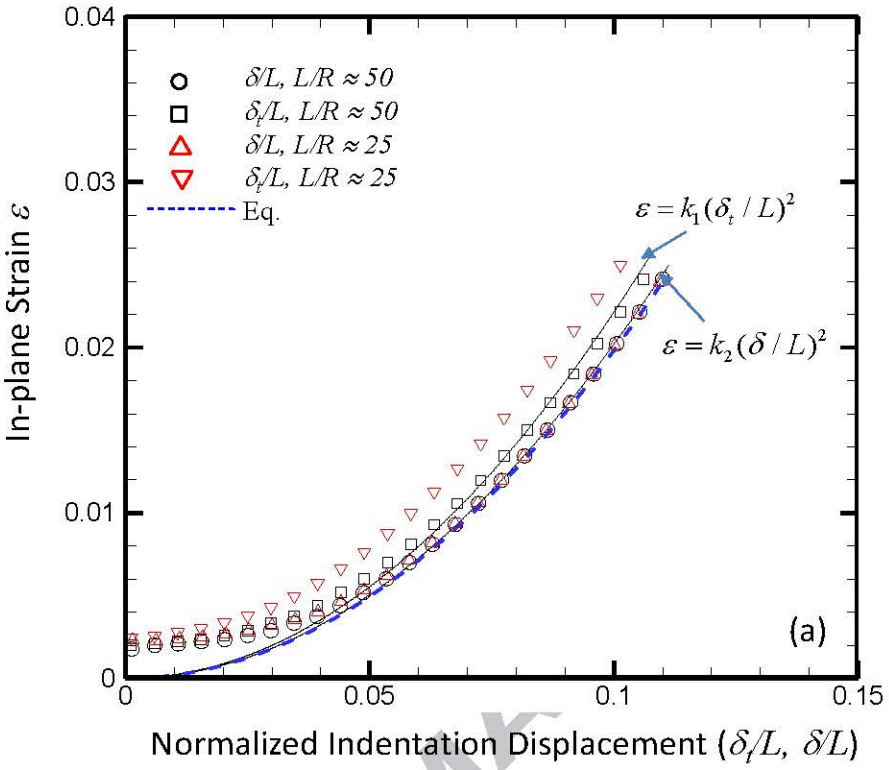

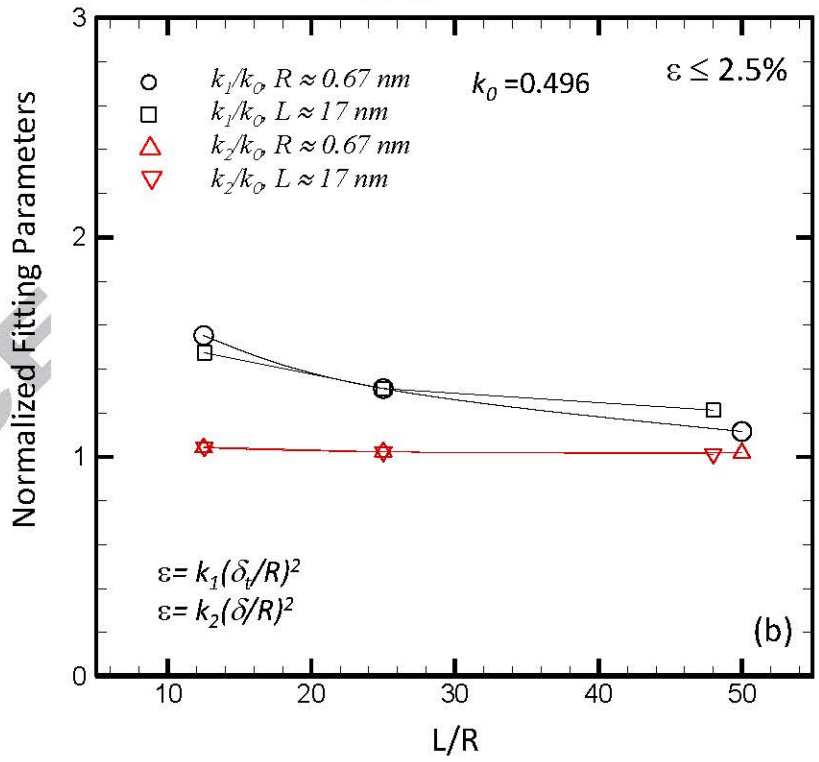

Figure 19.

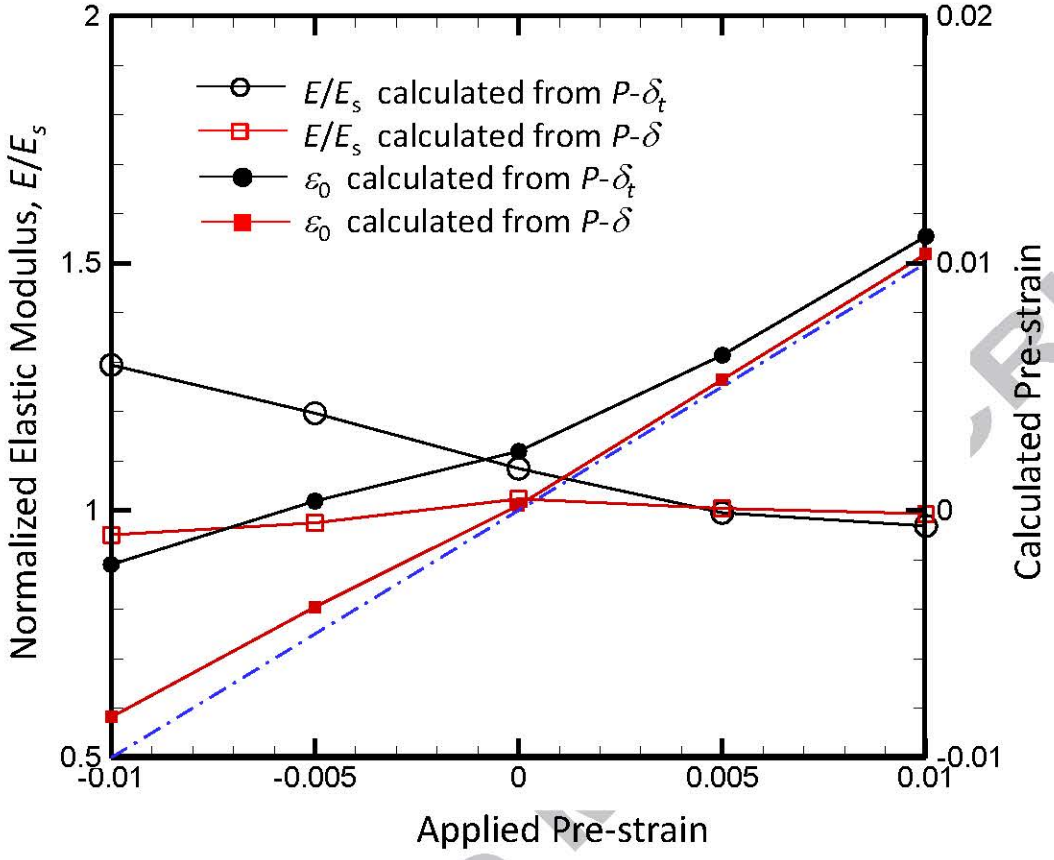

Figure 20

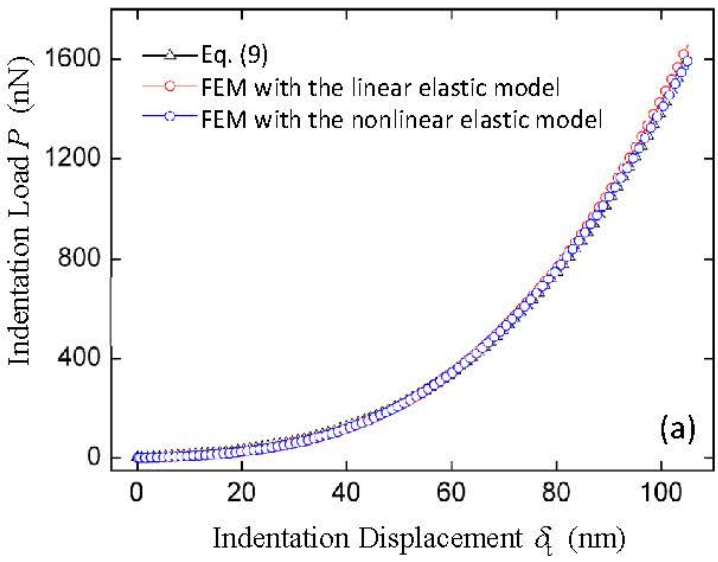

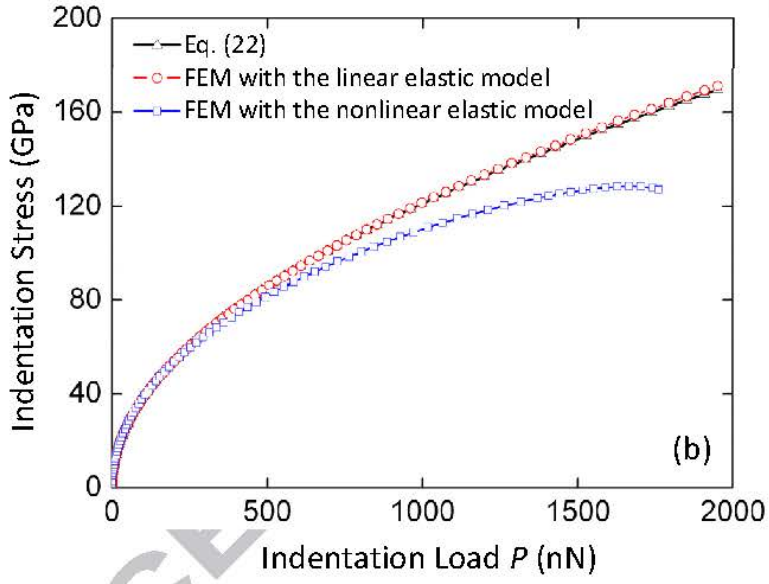

Figure 21

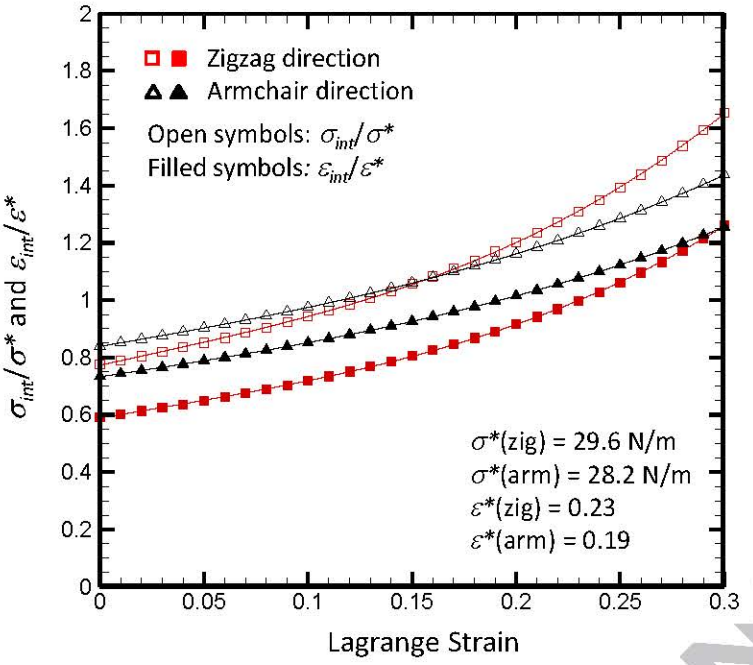

Figure 22.

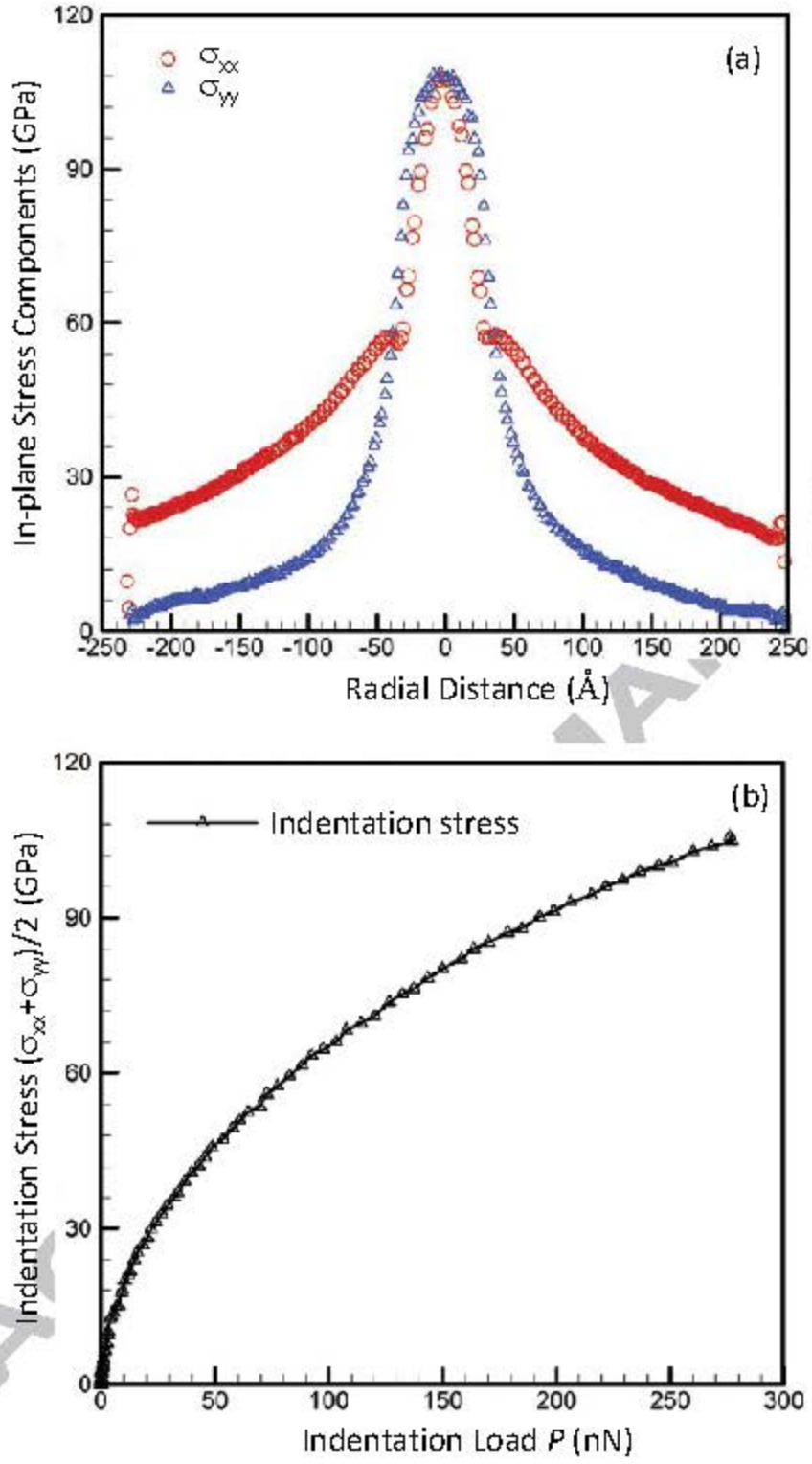

Figure 23

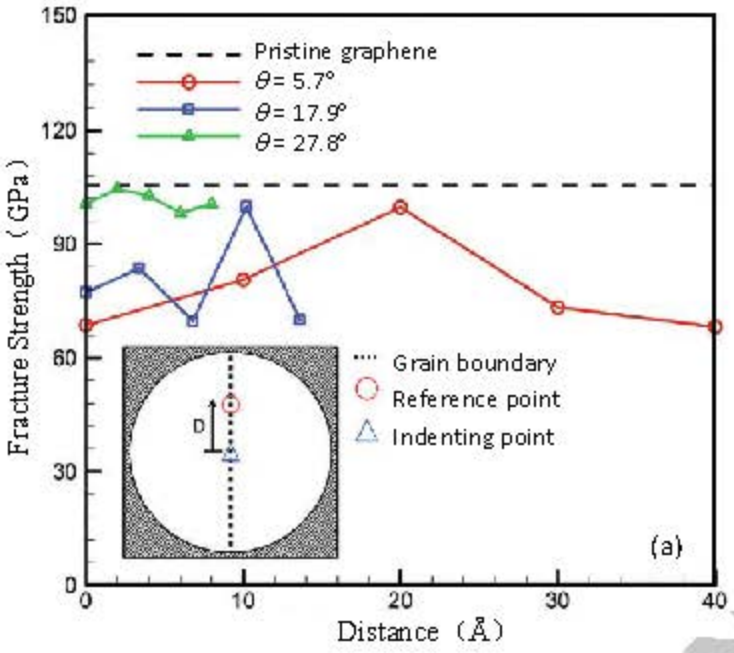

Figure 24(a)

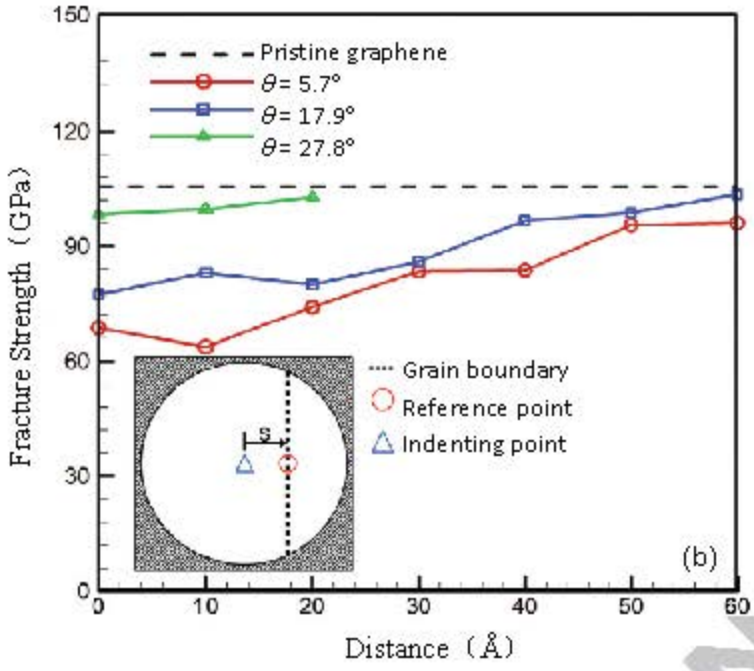

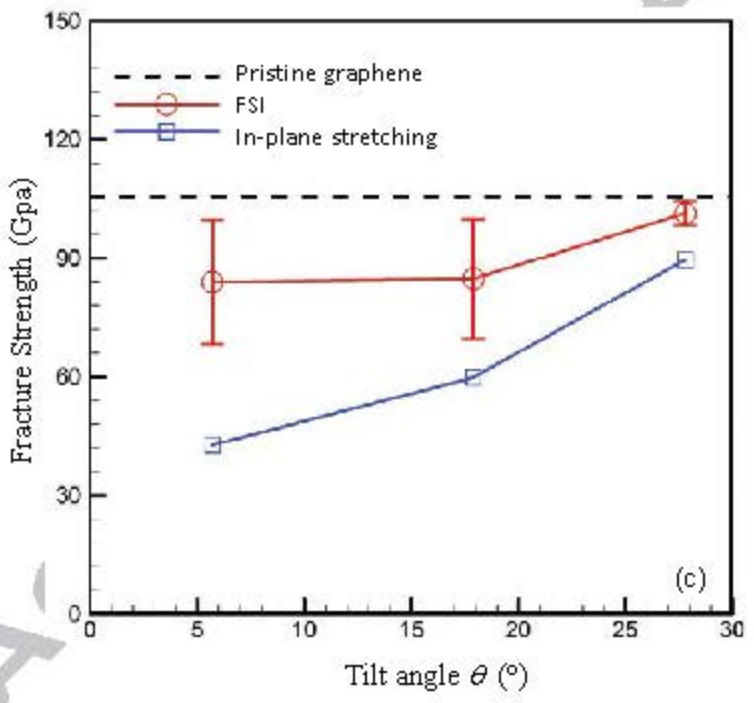

Figure 24(b)(c)

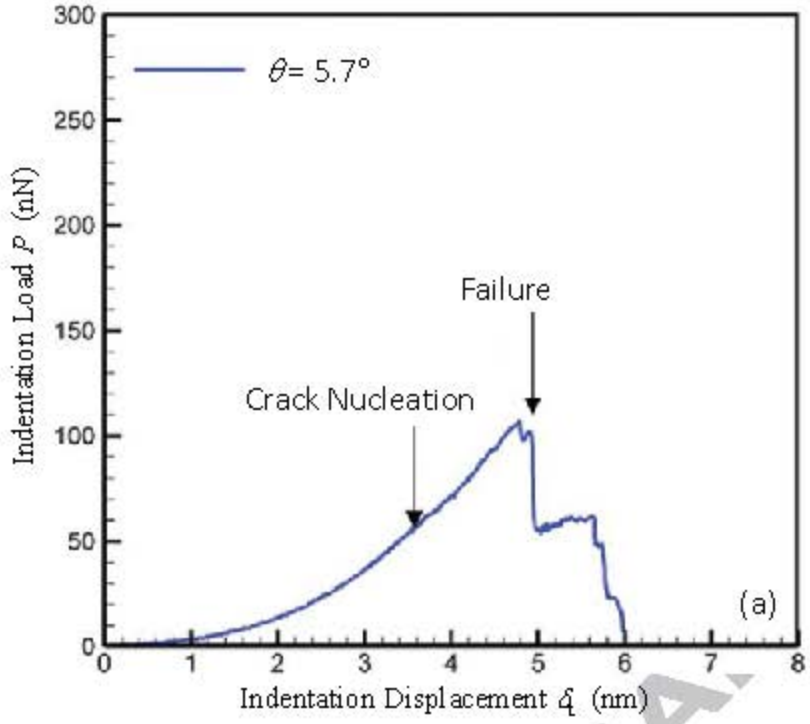

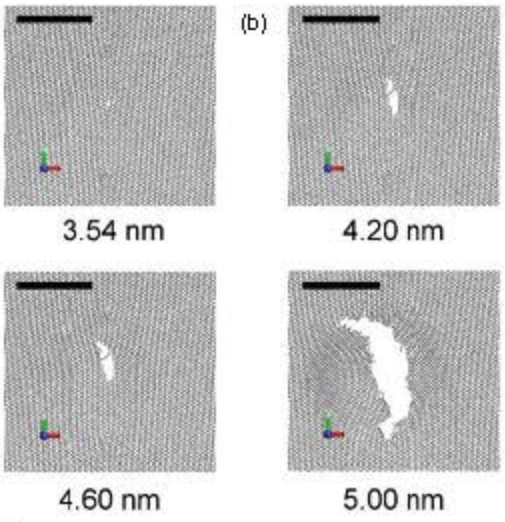

Figure 25

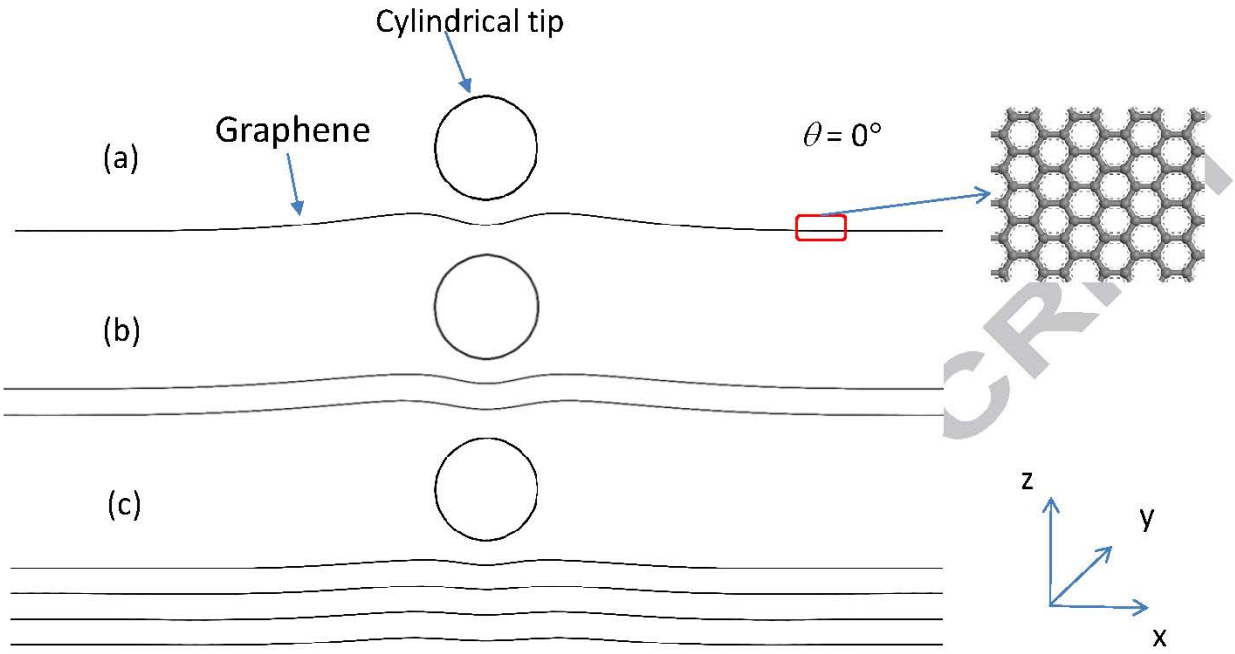

Figure 26.

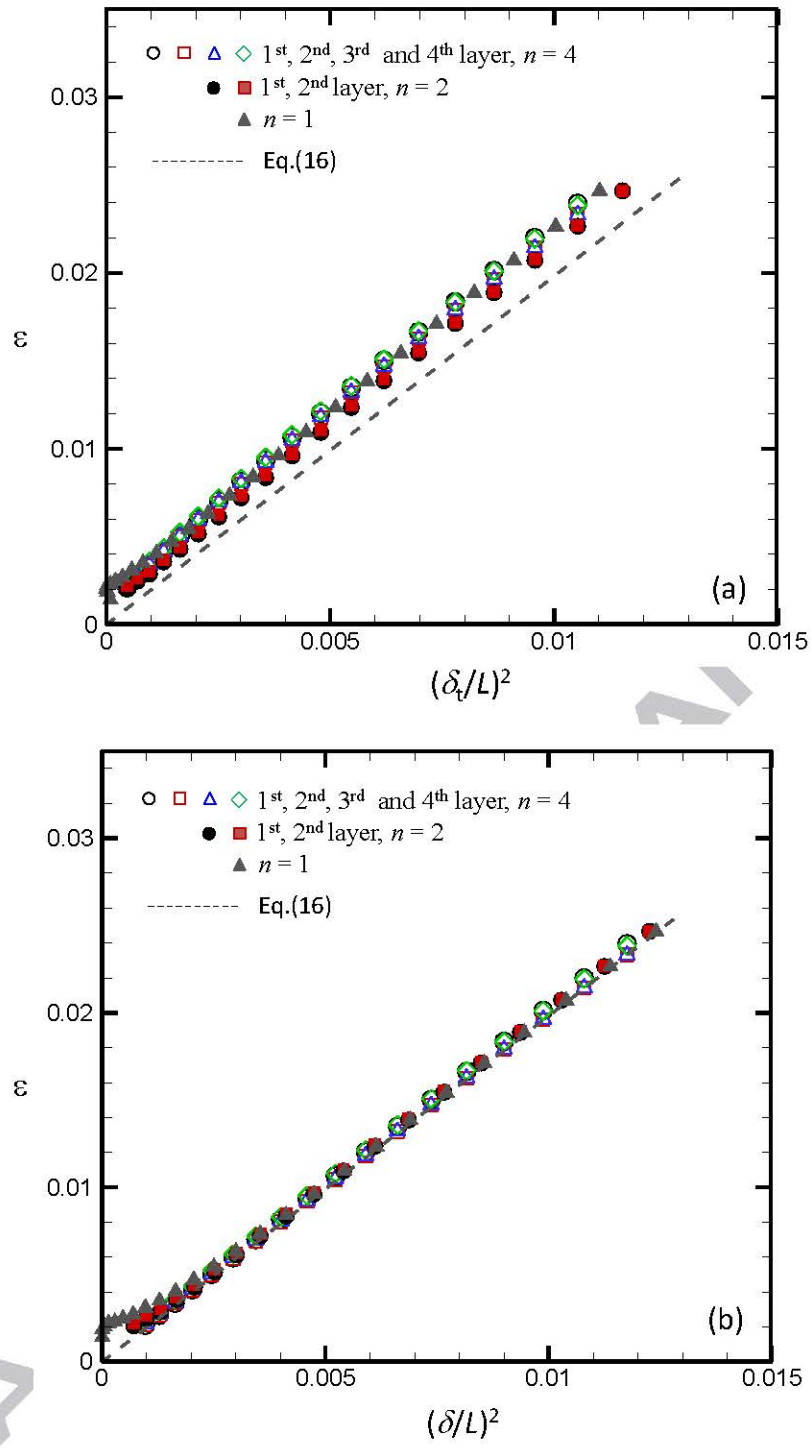

Figure 27

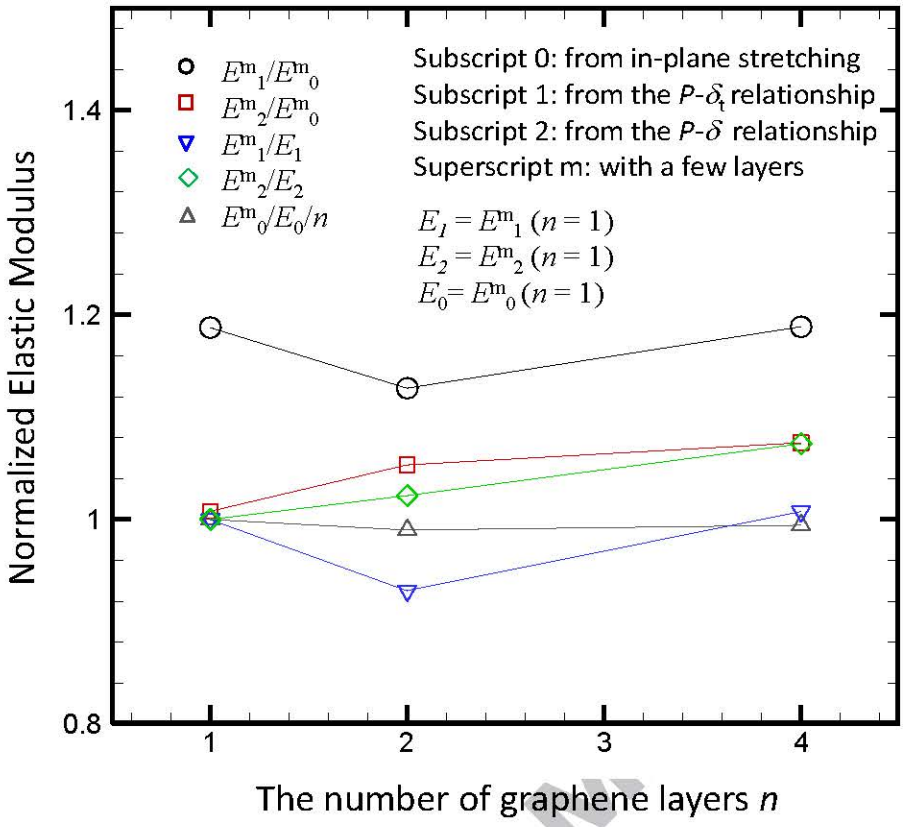

Figure 28.

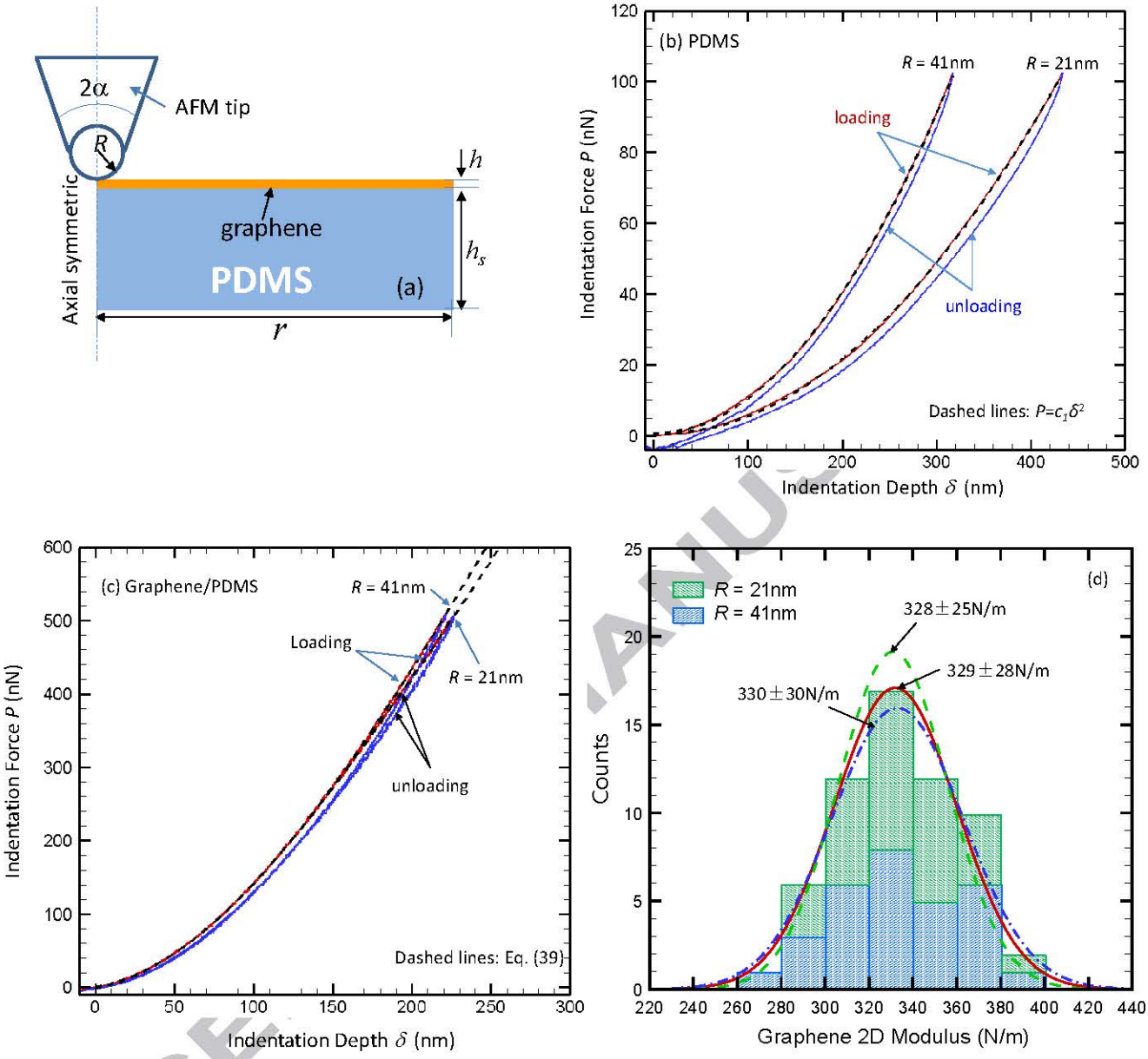

Figure 29

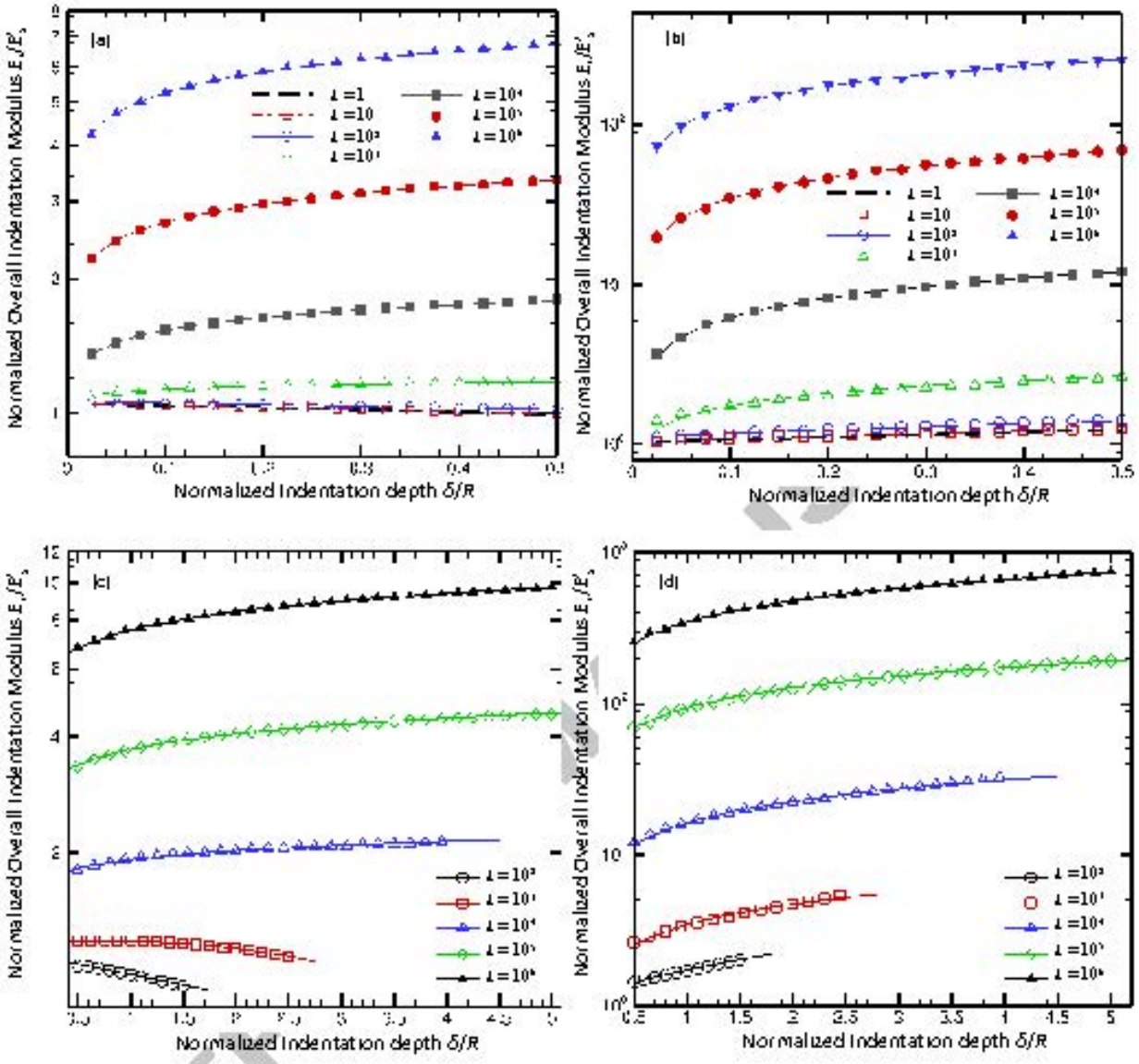

Figure 30

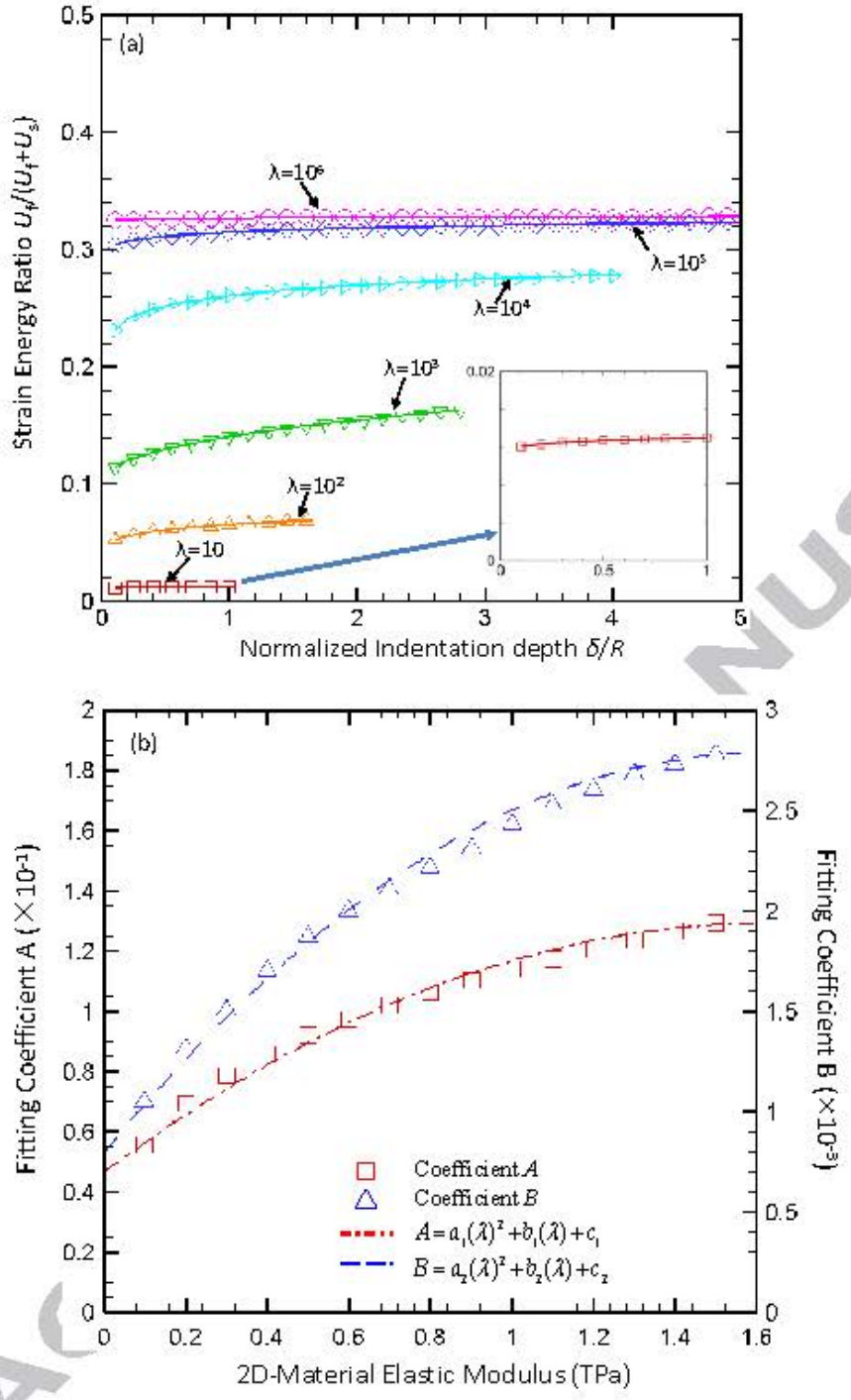

Figure 31

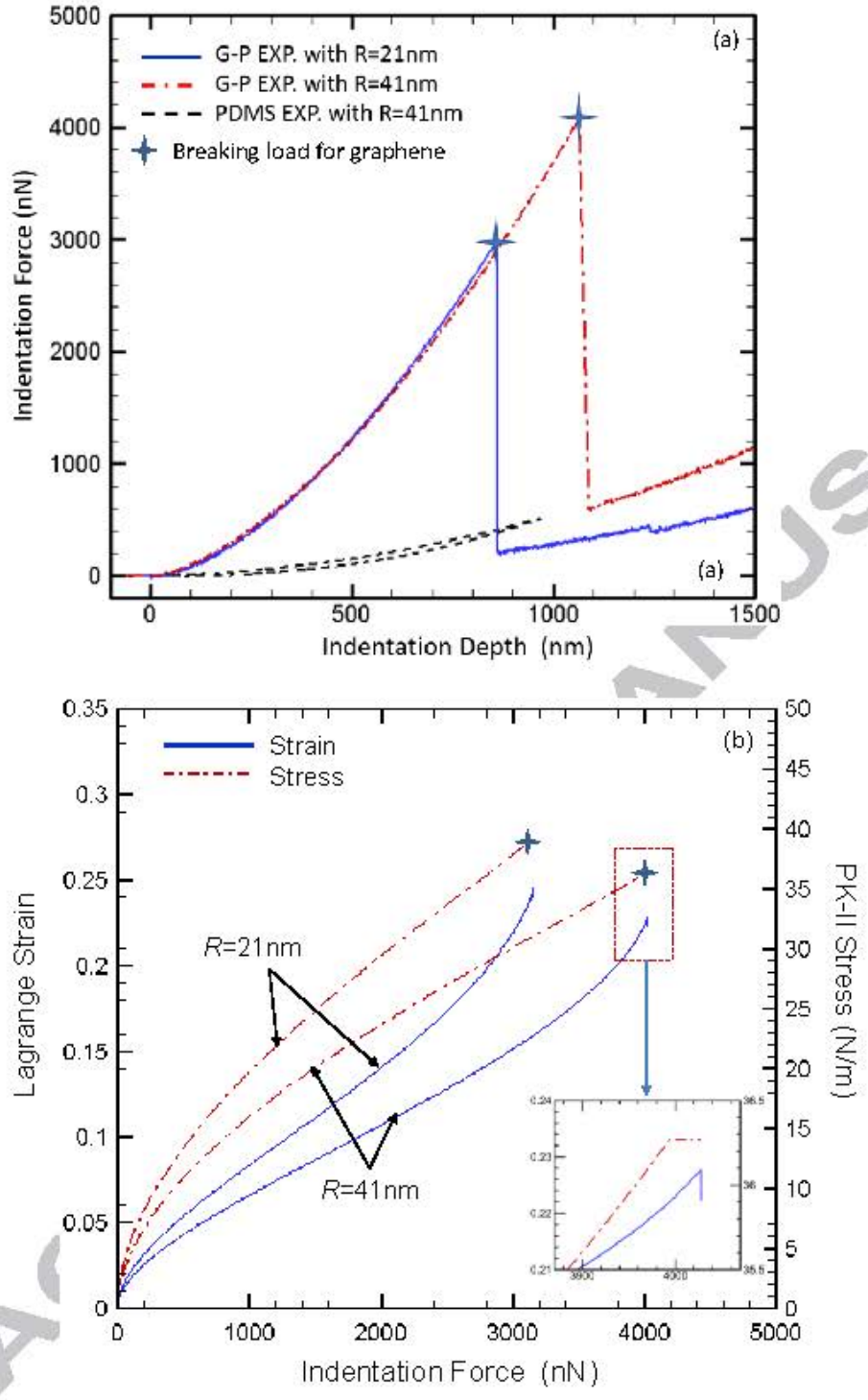

Figure 32

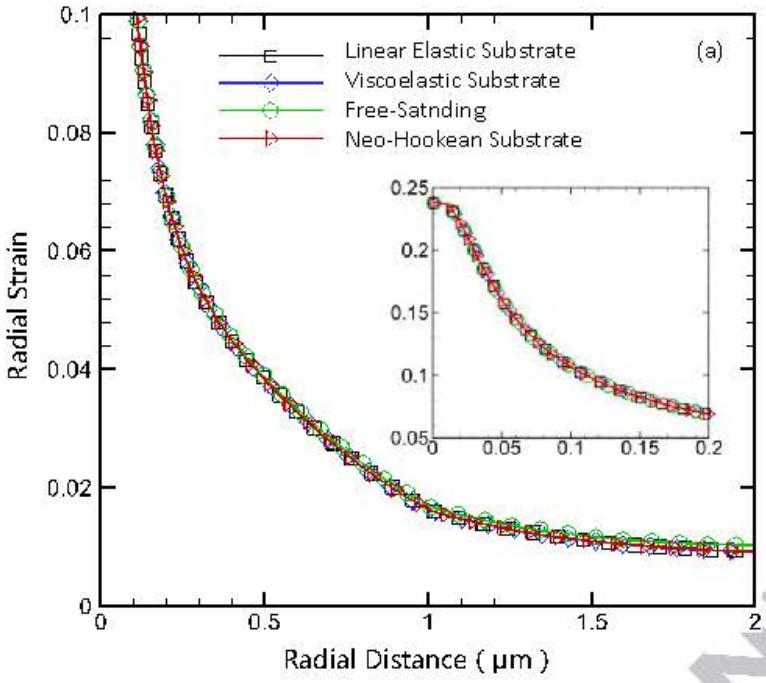

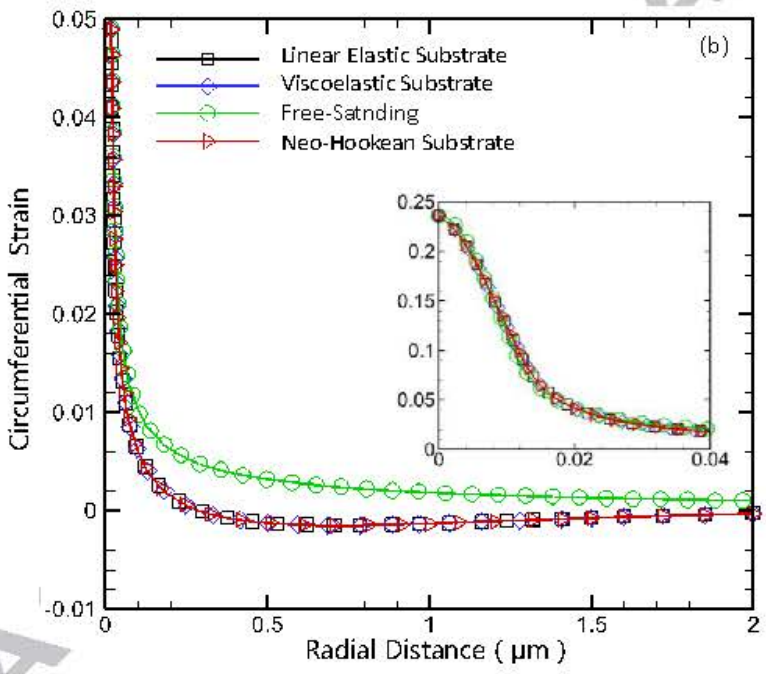

Figure 33

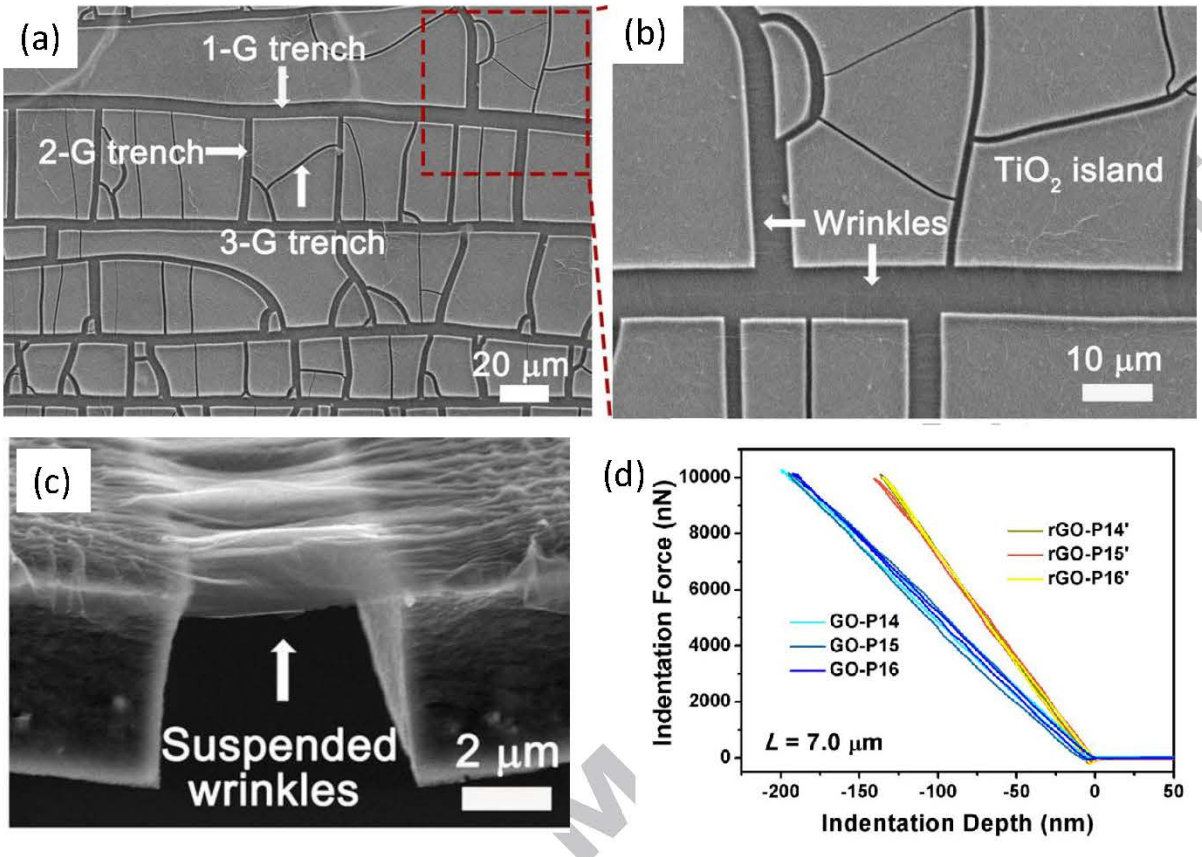

Figure 34

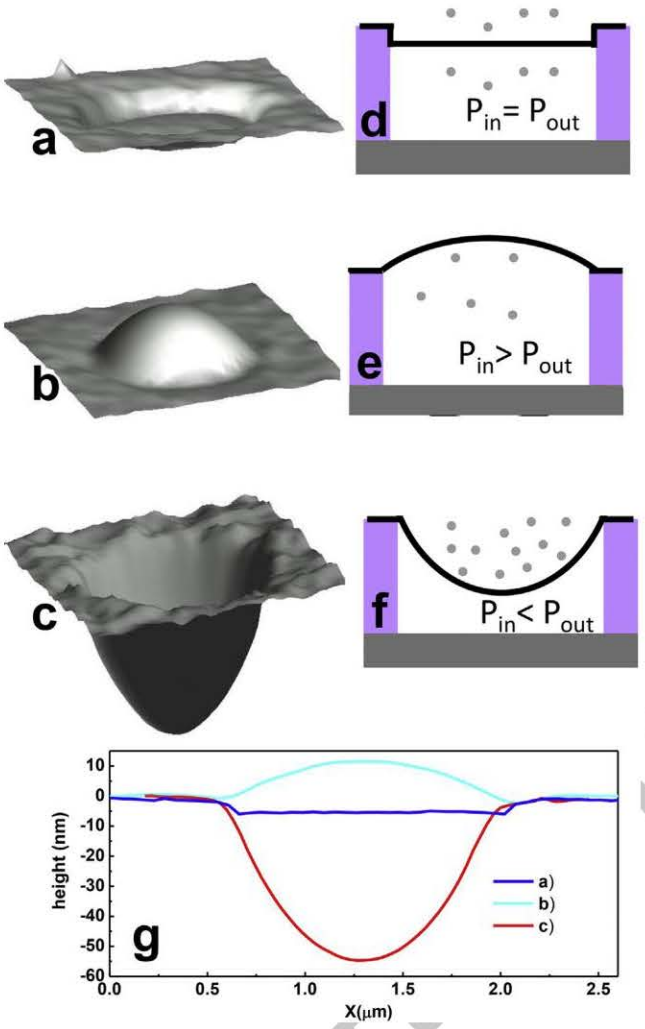

Fig. 35